

Counting Calories – Studies of Energy Loss in a Segmented Calorimeter

SARA BERGENIUS GAVLER



KTH Physics

Doctoral Thesis
Stockholm, Sweden 2006



Doctoral Thesis

Counting Calories – Studies of Energy Loss in a Segmented Calorimeter

Sara Bergenius Gavler

Particle- and Astroparticle Physics, Department of Physics
Royal Institute of Technology, SE-106 91 Stockholm, Sweden

Stockholm, Sweden 2006

Cover illustration: Sampled electromagnetic shower
Image montage by Sara Bergenius Gavler
Original image by F. Schmidt, "CORSIKA Shower Images",
<http://www.ast.leeds.ac.uk/~fs/showerimages.html>

Akademisk avhandling som med tillstånd av Kungliga Tekniska Högskolan i Stockholm framlägges till offentlig granskning för avläggande av filosofie doktorsexamen fredagen den 28 april 2006 kl 10.15 i sal FB55, AlbaNova, KTH Partikel- och Astropartikelfysik, Roslagstullsbacken 21, Stockholm.
Avhandlingen försvaras på engelska.

ISBN 91-7178-319-9
TRITA-FYS 2006:23
ISSN 0280-316X
ISRN KTH/FYS/--06:23--SE

© Sara Bergenius Gavler, April 2006
Printed by Universitetsservice US AB 2006

Abstract

The Gamma-ray Large Area Space Telescope (GLAST) is a space mission with anticipated launch in 2007. The aim is to study the gamma-ray sky in the energy range 10 keV–300 GeV. The GLAST electromagnetic calorimeter is $8.6X_0$ deep and has a total of 1536 CsI(Tl) crystals each measuring $32.60 \times 2.67 \times 1.99 \text{ cm}^3$. The crystals are read out at both ends with PIN photodiodes.

As a part of the quality control procedure during crystal production, samples from all CsI(Tl) boules were irradiated with gamma-rays from a ^{60}Co source. The average decrease in light yield was found to be $(13.4 \pm 0.7)\%$ after 100 Gy, 5 times the expected dose during a 5 year mission. The correspondence between the radiation damage of boule samples and the full-sized crystals were examined. A full-size crystal was also irradiated with a 180 MeV proton beam, with a decrease in light yield of $(22 \pm 5)\%$ after a dose of 175 Gy. The induced radioactivity of the crystal was also studied and a number of radioactive nuclei could be identified.

Detailed simulations of electron- and photon-induced showers in a segmented CsI calorimeter have been performed in the energy range 1–100 GeV, and for incident angles 0° , 30° and 60° . The energy distributions in the 1.99 cm ($1.08X_0$) thick layers were found to change systematically along the shower, varying little with initial energy. Three probability distributions have been fitted to the data: negative binomial, log-normal and Gaussian distributions. The energy fluctuations generated from non-perpendicular incident were similar to those for perpendicular incidence.

Two energy reconstruction methods were also studied, shower profile fitting and leakage correction. The latter gave better energy resolution, 5.1% and 7.6% (6.6% and 9.1%) for 1 GeV and 10 GeV electrons (photons) in the segmented $8.6X_0$ calorimeter. A third method, using a maximum likelihood method is also discussed.

Contents

Abstract	iii
Contents	v
1 Introduction	3
1.1 Gamma-ray astronomy	3
1.1.1 Detecting gamma-rays	3
1.1.2 Current status of gamma-ray missions	5
1.2 Outline of the thesis	6
1.3 Contributions by others	8
2 GLAST	9
2.1 Mission overview	9
2.2 Scientific objectives	10
2.3 The GLAST instruments	12
2.3.1 Tracker	12
2.3.2 Calorimeter	14
2.3.3 Anticoincidence detector	16
2.3.4 Data acquisition system	17
2.3.5 Gamma-ray burst monitor	17
3 Energy measurements using crystal calorimeters	19
3.1 Particle interactions in the calorimeter	19
3.1.1 Interactions of charged particles	20
3.1.2 Interactions of photons	22
3.2 Electromagnetic showers	25
3.2.1 Longitudinal development of electromagnetic showers	26
3.2.2 Lateral development of electromagnetic showers	27
3.3 Hadronic showers	29
3.4 Energy resolution	31
3.5 GLAST calorimeter properties	32
3.5.1 Energy and position resolution	33

3.5.2	Readout system	34
3.5.3	Calibration of the GLAST calorimeter	34
4	GLAST CsI(Tl) crystal elements	37
4.1	Crystal scintillators	38
4.1.1	Scintillation mechanism in inorganic crystals	38
4.1.2	Intrinsic Crystals	44
4.1.3	Extrinsic Crystals	44
4.2	Properties of inorganic scintillators	46
4.2.1	Scintillation efficiency	47
4.2.2	Time characteristics	49
4.2.3	Light propagation and readout	49
4.2.4	Temperature dependence	53
4.2.5	Mechanical and chemical properties	53
4.3	Radiation environment of GLAST	54
4.4	Radiation damage of CsI(Tl) crystals	56
4.4.1	Mechanism of radiation damage	57
4.4.2	Effects of radiation damage	58
4.5	Radiation hardness tests of CsI(Tl) crystals	60
4.5.1	Radiation hardness tests of boule samples	61
4.5.2	Gamma irradiation of full-size crystals	63
4.5.3	Proton irradiation of full-size crystals	66
4.5.4	Results of boule sample tests	69
4.5.5	Results of gamma irradiation of full-size crystals	71
4.5.6	Results of proton irradiation test	73
5	Simulation studies of a segmented calorimeter	79
5.1	Shower fluctuations	79
5.2	Simulation of energy fluctuations using Geant4	81
5.3	Longitudinal shower profiles	82
5.4	Sample fluctuations	83
5.4.1	Non-perpendicular incidence	91
5.5	Discussion	92
6	Energy estimation in a segmented calorimeter	97
6.1	Energy reconstruction methods	97
6.1.1	Shower profile fitting	98
6.1.2	Energy leakage compensation	105
6.1.3	Maximum likelihood method	107
6.2	Summary	109
7	Conclusions and outlook	111
7.1	Radiation hardness tests	111
7.2	Simulations of energy fluctuations	112

<i>Contents</i>	vii
Acknowledgments	115
List of figures	117
List of tables	119
Bibliography	121

WITHOUT DEVIATION PROGRESS IS NOT POSSIBLE.

FRANK ZAPPA

Chapter 1

Introduction

1.1 Gamma-ray astronomy

There is no exact definition of the energy region of gamma-ray photons, but usually a lower limit of a few keV is adopted. At the upper end of the spectrum, very high energy gamma-rays cover the energy range around 100 GeV–10 TeV, and ultra high energy gamma-rays from 10 TeV and upwards.

Gamma-ray astronomy is a relatively modern field¹, before 1930 the astronomers were mostly concerned with optical observations of stars, galaxies and nebulae. In 1932, Karl Jansky discovered radio emission from the Milky Way, and since then many wavebands have been opened up for astronomical observation and are now disciplines of their own; infrared, ultraviolet, X-ray and gamma-ray. With a wider range of the electromagnetic spectrum available, a legio of new objects that emitted light in other wavelengths than optical were discovered – radio galaxies, quasars, pulsars, X-ray binaries, black holes, gamma-ray bursts, etc.

The gamma-ray sky was observed for the first time in the 1960s, but is still today not fully mapped. All other energybands from radio to X-rays have already been explored quite extensively, leaving the gamma-ray sky essentially to be the last of the electromagnetic windows to be opened. There is a great possibility for findings of new physics in gamma-ray astronomy, and it may well be the key to understand the mechanisms behind some of the already observed phenomena.

1.1.1 Detecting gamma-rays

Due to their small interaction probability the universe is essentially transparent to gamma-rays. Also, as photons are neutral they are not deviated by magnetic fields. Hence, gamma-rays point directly back to its source of origin, providing a

¹Astronomy is probably the oldest of the sciences, dating back as far as 2000–3000 b.c. There even exist (controversial) claims that carvings in 32000 years old mammoth tusks depict star constellations. Still, both are well before the invention of the colour TV.

direct view into nature's highest energy acceleration processes. It is, however, these properties of gamma-rays that make them difficult to detect. Unlike optical photons they cannot be focused, and in addition there are a relatively small number of photons in the gamma-ray energyband, demanding new detector techniques having high efficiencies. Another obstacle, and perhaps the main reason why gamma-ray astronomy developed so late, is that gamma-rays are difficult to measure from the ground since they are absorbed in the atmosphere, and measurements had to be performed with balloon-borne or space-based detectors. The detectors consisted of dense materials in order to stop the gamma-rays, and due to the limited size of space missions, these gave very coarse measurements.

Space missions

The first observation of the high-energy gamma-ray sky took place in 1961 with the launch of the first high-energy astrophysics satellite Explorer-XI. The detector consisted of a sandwich crystal scintillator (CsI and NaI), a Cherenkov counter, surrounded by a plastic anticoincidence scintillator². The satellite could not be actively pointed, but was put into a tumble in order to get a rough scan of the celestial sphere. It detected 22 cosmic gamma-ray events. In 1967, an instrument on-board OSO-III detected the Milky Way as a source of gamma-ray emission. An unexpected but very important contributor to the origins of gamma-ray astronomy in the 1960s and 1970s were the Vela satellites. Intended to watch for violations of an international treaty banning atmospheric testing of nuclear weapons, they instead gave the first hints of gamma-ray bursts. In 1972 the SAS-2 satellite detected an isotropic diffuse, apparently extragalactic, gamma-ray background. It also detected the Crab and Vela pulsars which had first been discovered in radio wavelengths 5 years earlier, and the then unidentified Geminga pulsar (a radio-quiet pulsar whose optical and X-ray counterpart wasn't found until nearly 20 years later). The COS-B satellite (1975–1982) produced the first map of the galaxy in gamma-ray wavelengths, and a catalogue of 25 point sources.

In 1991 the Compton Gamma-Ray Observatory (CGRO) was launched. The satellite carried four major instruments including the Energetic Gamma-ray Experiment Telescope (EGRET), which greatly improved the spatial and temporal resolution of gamma-ray observations. EGRET made a complete survey of the gamma-ray sky and produced a catalogue of 271 sources of which approximately half are still unidentified. It found a new class of objects called blazars, which are extragalactic sources with bright and variable gamma-ray emission. The mission was ended by a controlled re-entry in the atmosphere in 2000, but the data is still being studied.

²More information about historic and future gamma-ray missions can be found on NASA's webpage <http://heasarc.gsfc.nasa.gov>

Ground-based missions

If the gamma-ray is energetic enough it can be measured with ground-based detectors. When interacting with the atmosphere, a gamma-ray produces a cascade of charged particles. For gamma-ray energies above a few TeV, the charged particles are energetic enough to produce Cherenkov light³ that can be detected from ground. The pattern of the Cherenkov radiation gives information about the energy and direction of the original gamma-ray photon.

One of the first successful gamma-ray Cherenkov telescopes, the Whipple Gamma-ray Telescope, started measuring TeV gamma-rays in the late 1980s. Although first ground-based detections were reported in the 1970s, it was not until later the imaging technique provided means to distinguish between air showers induced by cosmic-rays (protons and heavier atomic nuclei) and gamma-ray induced air showers. The ground-based technology was developed further with HEGRA (1997–2002) which used an array of atmospheric Cherenkov telescopes.

Another method to detect air showers is by extensive air shower (EAS) arrays, where the shower particles are detected instead of the Cherenkov light. Unlike the Cherenkov telescopes EAS arrays can operate night or day, and can view the entire overhead sky continuously. However, the distinguishing between gamma-rays and nuclear cosmic-rays is not as efficient as the imaging method used by the Cherenkov telescopes.

A third method is a water Cherenkov extensive air shower array, where the Cherenkov light generated by the charged particles as they pass through water is measured. The first example of a water Cherenkov detector used to detect gamma-rays is MILAGRO.

1.1.2 Current status of gamma-ray missions

The next generation of gamma-ray satellites will continue where previous missions ended. The Gamma-ray Large Area Space Telescope (GLAST) mission was initiated when it was realised that an instrument with higher precision was needed in order to understand the discoveries of EGRET. The goal was to continue where EGRET had stopped, mapping the gamma-ray sky, pin-point the objects still unidentified but also search for new physics. The design of GLAST emerged as a result of improvement of the EGRET construction and by using refined technology from existing high-energy detectors. Table 1.1 shows the improvements of mission parameters of some gamma-ray missions over the last 40 years.

In the last few years, several new gamma-ray missions have been launched, for example INTEGRAL which is sensitive in the energy range 15 keV–10 MeV, and the missions HETE-2 and Swift which will study gamma-ray bursts in details in the keV range. Missions that are due to launch in a near future are AGILE in 2006,

³Cherenkov light is produced when the velocity v of a charged particle exceed the speed of light in a medium with refractive index n , $v > c/n$

Table 1.1. High-energy gamma-ray missions. A_{eff} is the effective area, and Ω is the field of view. Adapted from [1].

Instr.	Years	$\theta_{0.1}^a$ ($^\circ$)	θ_{10}^b ($^\circ$)	Energies (GeV)	$A_{eff} \cdot \Omega$ ($\text{cm}^2 \text{ sr}$)	No. gamma-rays
OSO-3	1967–68	18	-	>0.05	1.9	621
SAS-2	1972–73	7	-	0.03–10	40	$\sim 1 \times 10^4$
COS-B	1975–82	7	-	0.03–10	40	$\sim 2 \times 10^5$
EGRET	1991–00	5.8	0.5	0.03–10	750	1.4×10^6
AGILE	2006–	4.7	0.2	0.03–50	1500	$4 \times 10^6/\text{yr}$
LAT	2007–	3.5	0.1	0.01–300	25000	$1 \times 10^8/\text{yr}$
AMS	2008–	-	0.1	1–300	500	$\sim 2 \times 10^5/\text{yr}$

^aAngular resolution at 0.1 GeV

^bAngular resolution at 10 GeV

GLAST in 2007, and later AMS. These missions will be able to detect gamma-rays in the GeV range.

GLAST will complement the capabilities of the next-generation atmospheric Cherenkov and shower gamma-ray telescopes, such as ARGO, CANGAROO-III, CELESTE, HESS, MAGIC, MILAGRO, STACEE and VERITAS. In contrast to GLAST they have very large effective collecting areas, but small field of view (except for MILAGRO). Figure 1.1 shows the sensitivities of present and future gamma-ray detectors. GLAST is expected to improve sensitivity by one or two orders of magnitude with respect to the EGRET mission. The overlap between GLAST and the next-generation Cherenkov telescopes allow energy and sensitivity calibrations.

1.2 Outline of the thesis

The main subject of this thesis is energy measurements using a segmented CsI(Tl) crystal calorimeter. It consists of mainly two parts, the radiation hardness tests of the GLAST CsI(Tl) crystals, and a simulation study of individual electromagnetic showers in a longitudinally segmented CsI calorimeter.

This first chapter, which you have (probably) already read, gave a short introduction to the field of gamma-ray astronomy, different detection techniques and some of the past, present and future gamma-ray missions. Chapter 2 gives an overview of the GLAST mission and some of the science objectives, followed by a brief introduction the GLAST instruments. In chapter 3 the basics of homogeneous electromagnetic calorimeters and their performance are presented, this includes particle interactions with matter and electromagnetic cascades. In connection to this, some of the challenges involved in the design of the GLAST calorimeter are discussed. Chapter 4 presents the experimental method and the results of the radiation

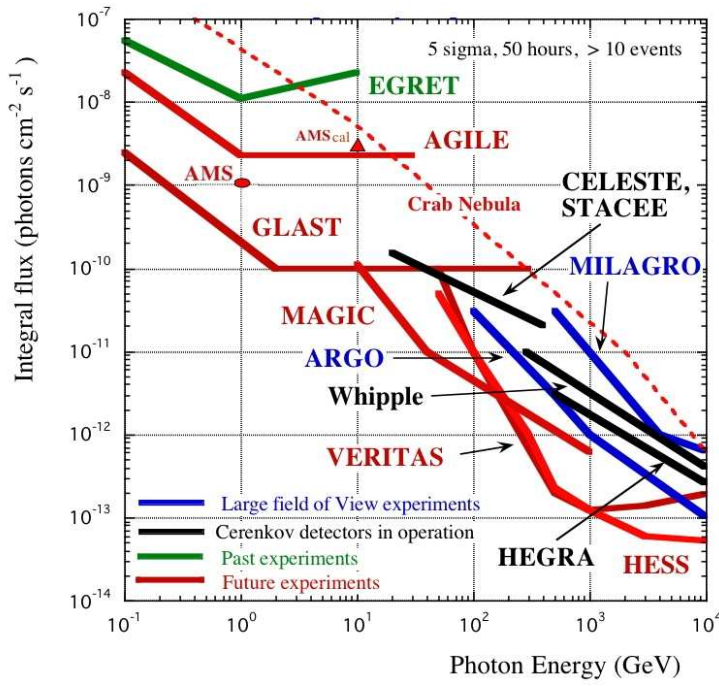


Figure 1.1. The predicted sensitivities of a number of gamma-ray space detectors (from [2]). CELESTE, STACEE, VERITAS Whipple is for a 50 hours exposure of a single source. The EGRET, GLAST, MILAGRO, ARGO, AMS and AGILE sensitivities are shown for one year of all-sky survey. For AMS only the estimate for two points exist, one for the AMS-conversion mode and the second is for the calorimeter mode.

hardness tests of CsI(Tl) crystals. In order to understand how the scintillator quality is affected by radiation, the scintillation mechanism and the basic properties of inorganic scintillators are reviewed. The mechanism and effects of radiation damage are discussed, and in connection to this, some background to the space environment of the GLAST satellite is given. Chapters 5 and 6 present the simulation studies of electromagnetic showers in a segmented CsI calorimeter. Both chapters address the problem arising from shower-to-shower fluctuations. In chapter 5 the energy distributions, resulting from shower fluctuations, at various depth in the calorimeter are studied. In chapter 6 different energy reconstruction algorithms are reviewed, and simulation data are used to compare the methods. Also, a new reconstruction method is discussed.

1.3 Contributions by others

I would like to point out contributions made by others in this thesis. The optical test-setup in the radiation hardness tests of the full-size crystal was engineered by Leif Nilsson, and the analysis of the degradation of light yield was performed by Georg Johansson and Staffan Carius. The proton beam intensity profile (figure 4.18) and the dose rate were provided by the staff at TSL. Apart from this, the material in chapters 4–6 is based on my own measurements, analysis and simulations, if not stated otherwise.

Chapter 2

GLAST

2.1 Mission overview

The GLAST satellite will detect gamma-rays in the rather wide energy range 10 keV–300 GeV. At high-energies, there is some overlap with other missions such as the ground-based Cherenkov telescopes. This overlap enables the measurements made by GLAST to be combined with observations by the next-generation atmospheric Cherenkov and shower gamma-ray telescopes.

The GLAST mission will follow closely in the footsteps of EGRET, continuing to catalogue gamma-ray objects, but with much better sensitivity. The large increase in sensitivity as compared to EGRET is mainly due to three improvements. One is the larger effective area, which is the product of total geometric acceptance, conversion probability, and all detector and reconstruction efficiencies. The real rate of detecting a signal is then the flux of gamma-rays multiplied with the effective area. Secondly, the detector has a wide field of view, simultaneously “seeing” about 2 steradians of the sky¹. Finally, the third improvement is the much better angular resolution improving the ability of determining the direction of the gamma-ray, allowing fewer background events. A comparison between the GLAST and EGRET capabilities is shown in table 2.1.

GLAST is scheduled to launch in 2007. It will be placed in orbit at an altitude of 600 km with 28.5° inclination. The first year in orbit will be dedicated to an all-sky survey, and the remainder of the mission will consist of point observations. In survey mode, GLAST will be rocked 35° up or down for alternating orbits, providing a uniform exposure over the entire sky. The detector will point away from the Earth in order to maximise the exposure to the celestial gamma-rays. The large effective area together with the large field of view enables the LAT to observe the entire sky (except for the orbit poles) in one orbit. This is very useful

¹The steradian (sr) is the SI unit of solid angular measure, there are 4π steradians in a complete sphere.

Table 2.1. A comparison between GLAST and EGRET mission parameters.
Adapted from [3]

	EGRET	GLAST
Energy range	20 MeV–30 GeV	20 MeV–300 GeV
Peak effective area ^a	1500 cm ²	>8000 cm ²
Angular resolution ^b	5.8° (100 MeV)	< 3.5° (100 MeV) < 0.15° ($E > 10$ GeV)
Energy resolution ^c	10%	<10%
Field of view ^d	0.5 sr	>2.4 sr
Deadtime per event	100 ms	< 100μs
Source location determination ^e	5–30 arcmin	1–5 arcmin
Point source sensitivity ^f	$\sim 1 \times 10^{-7} \text{cm}^{-2} \text{s}^{-1}$	$4 \times 10^{-9} \text{cm}^{-2} \text{s}^{-1}$

^aAfter background rejection

^bSingle photon, 68% containment, on-axis

^c1σ, on-axis

^dIntegral of effective area over solid angle divided by peak effective area.

^eRange: bright sources to sources of 10^{-8} photons cm⁻²s⁻¹ flux at > 100 MeV.

^fSensitivity at high latitude after a 2-year survey for a 5σ detection.

for observing transient sources such as gamma-ray bursts and flaring active galactic nuclei (blazars). GLAST is designed for a mission duration of 5 years with a goal of 10 years.

The GLAST collaboration is multi-national and consists of institutions from France, Italy, Japan, Sweden and USA. The instruments are currently being integrated and tested at the Stanford Linear Accelerator Center.

2.2 Scientific objectives

Gamma-rays do not carry charge and can therefore travel through space without becoming deflected by magnetic fields as is the case for charged cosmic-rays, and therefore point directly back to its source. In addition, they have a small interaction cross section below a few TeV which implies that the Universe is more or less transparent to gamma-rays in the energy range of GLAST. This makes it possible to probe the processes giving rise to these high-energetic signals. GLAST will image the sky with an unprecedented precision in an energy-band which is not yet fully covered, which means that there is a great potential of new discoveries. The main scientific goals of the GLAST mission are:

- Understand the mechanisms of particle acceleration in active galactic nuclei (AGN), pulsars and supernova remnants.
- Resolve the diffuse gamma emission and the sources EGRET left unidentified.

- Determine the high-energy behaviour of gamma-ray bursts and transients.
- Probe dark matter and the early universe.

One of the hot topics within astrophysics and cosmology is the detection of dark matter, which will here be discussed briefly. The summary is based on the review of Jungman et al. [4]. The detection of dark matter signals would be a tremendous discovery and a giant step forward for cosmology. Ever since the 1930s, when it was first realised that mass was “missing” and that there had to be some dark matter invisible to us, scientists have been mocked by the fact that only a fraction of the mass present in the Universe is visible to us. The measurements of the amount of luminous matter in spiral galaxies showed that there was not enough to account for their observed rotation curves, implying that there had to be either some invisible mass causing the extra gravitational pull, or a non-Newtonian gravitation. Evidence for dark matter has also been found through gravitational lensing, where heavy objects bend the light trajectories, and in hot gas surveys in galaxy clusters. These observations conclude that the objects studied must contain more mass than estimated through luminous matter. Today, observations indicate that the total density contents of the Universe consists of about 70% dark energy, 5% is matter visible to us and the rest is matter that does not absorb or emit electromagnetic radiation in any wavelength visible to us.

The candidates for dark matter can be divided into two main groups: baryonic and non-baryonic. The baryonic dark matter candidates include massive compact halo objects (MACHOs), for example brown dwarfs, stellar black hole remnants, white dwarfs located in the halos of galaxies. The non-baryonic candidates would be some new elementary particle and can be categorised into “hot” and “cold” dark matter, depending on if it was moving at relativistic- or non-relativistic speeds respectively at the time of galaxy formation. Therefore, studies of the process of galaxy formation can provide information of whether the dark matter is hot or cold. The leading hot candidate is the light Majorana neutrino, which unfortunately does not reproduce the observed structure well. However, suggestions that dark matter consists of both hot and cold non-baryonic particles could give a better modeling. The most successful cold dark matter candidates include axions, and weakly interacting particles (WIMPs). Due to the gravitational pull and the low probability of interactions with matter, these should gather in galactic halos and in stellar objects, thus being present in large quantities in the Milky Way halo. There are two ways to search for WIMPs, through direct and indirect detection. The first is to detect signals in crystals induced by the recoil of crystal nucleus from elastic scattering of a WIMP, and the latter is through detecting particles created in WIMP interactions.

One of the promising WIMP candidates for dark matter is the neutralino, χ , the lightest particle of the Minimal Supersymmetric Standard Model (MSSM). It is neutral and stable with a mass between 50 GeV to a few TeV, and can annihilate with another neutralino. The process $\chi\chi \rightarrow \gamma\gamma$ is possible and should give rise to a mono-energetic gamma line at an energy corresponding to the mass of the

neutralino. The flux of gamma-rays from this reaction depends on the galaxy and halo structure, cross sections for neutralino annihilations, see [5] for a review of gamma-ray signatures of dark matter annihilation. If the mass of the neutralino lies within the energy range of GLAST and the flux of gamma-rays is high enough, GLAST with its excellent background rejection and sensitivity could be capable of observing gamma-ray signals from neutralino annihilations. Recent calculations of the flux of gamma-rays from neutralino annihilations show that it is possible that the signal is visible above the diffuse extragalactic background [6]. It is also possible that most of the measured EGRET flux comes from unresolved AGNs so that the true diffuse background may be lower at the neutralino energies, than the EGRET extrapolation. GLAST will be able to resolve the AGNs if they constitute the diffuse background.

The dark matter search by GLAST would be for annihilation signatures in the Milky Way, or from extragalactic sources. A narrow line above 50 GeV would be a definitive signature of nonbaryonic dark matter and would determine the WIMP mass.

2.3 The GLAST instruments

GLAST is composed of two independent instruments: the Large Area Telescope (LAT) and the Gamma-ray Burst Monitor (GBM). The primary instrument is the LAT [7] which will measure gamma-rays in the energy range of 20 MeV–300 GeV. It consists of three major subsystems: a precision silicon tracker, a CsI(Tl) electromagnetic calorimeter and a segmented anti-coincidence detector. These are described in more detail below.

Like EGRET the LAT is a pair conversion instrument, many of the incident gamma-ray photons are converted to a electron-positron pair in the converter foils of the tracker. The signals from the charged electron and positron in the tracker can be traced back to the conversion point and give the incident photon direction. The energy of the pair, or a photon that did not convert in the tracker, is measured in the calorimeter.

LAT has a modular design, consisting of 16 identical towers arranged in a 4×4 array. Each tower has a base of about 40×40 cm² and consists of a complete setup of a tracker, calorimeter and data acquisition module. An overview of the LAT instrument is shown in figure 2.1. The modularity of LAT facilitates manufacturing, integration and testing, since each module is fully operational by itself. It also minimises the effects from component failure.

2.3.1 Tracker

The main task of the LAT tracker [8, 9] is to offer precise tracking of the electron-positron pair in order to determine the direction of the incident gamma-ray. At low energies (below 100 MeV) the tracker also provides energy measurement since

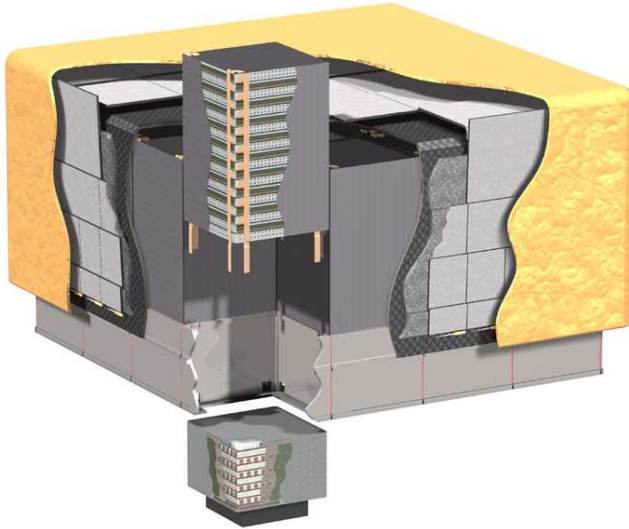


Figure 2.1. A schematic cutout of the LAT, showing a tower with the tracker on top and the calorimeter below. The 4×4 array of towers are covered with the segmented ACD. The outmost layer is a protective micro-meteor shield. The size of the instrument is about $170 \times 170 \times 90$ cm³. From the LAT collaboration.

the electron and positron deposits a non-negligible fraction of their energy in the tracker. The energy resolution is however much worse than the energy resolution of the calorimeter. There is a great improvement in the tracking system of LAT compared to EGRET's spark chambers. Most important, the new silicon-strip technology provides much better pattern information for background rejection, and reconstruction of the conversion pair which improves the angular resolution. It also has a much faster readout, with a dead time of a few tens of microseconds, compared to a hundred milliseconds for sparkchambers. The LAT tracker is self-triggering, while the spark chambers required an external trigger.

Each tracker tower consists of interleaved planes of silicon-strip detector sheets and tungsten converter foils. The planes are arranged in 19 trays, each tray containing two silicon-strip detector (SSD) planes oriented in the same directions, with a tungsten converter plate in between as shown in figure 2.2. Each tray is rotated 90° with respect to the adjacent trays. As a result, the SSD on the bottom of one tray forms a x - y pair with the SSD on the top of the tray below, each with a 2 mm gap between the SSDs. The topmost tray has no upper SSD, while the bottom tray has no lower SSD, so that each tracker has a total of 18 x - y pairs.

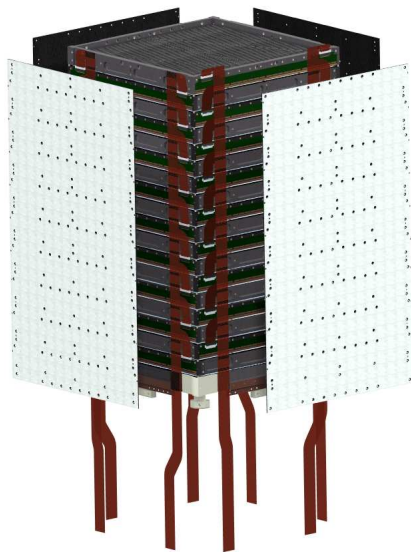


Figure 2.2. A exploded view of a tracker tower. The wires from the bottom of the tracker are readout cables. The tracker tower measures about $35 \times 35 \times 60 \text{ cm}^3$. From the LAT collaboration.

The first twelve tungsten layers have a thickness of $0.03X_0$, the following four are each $0.18X_0$ thick.² The thin layers ensure good tracking, whereas the thicker converters at the back give efficient conversion. The two x - y pairs at the bottom are not preceded by converter foils, since 3 x - y pairs is the minimum number needed to form an acceptable track, following a gamma-ray conversion. Taking into account all support materials the total depth of the tracker is about $1.6X_0$.

Each SSD plane has 1536 strips, 36 cm long and $400 \mu\text{m}$ thick, with a $228 \mu\text{m}$ pitch. Thus, a tower has about 55000 strips and the whole tracker instrument will have a total of about 885000 channels. One of the main technological challenges has been to maintain low noise and low power consumption despite this large number of readout channels. Other challenges has been to construct a low-mass, stiff carbon-composite structure to support the large SSD sheets, and to package the readout electronics while leaving minimal gaps between modules.

2.3.2 Calorimeter

The primary tasks of the GLAST electromagnetic calorimeter [10] are to provide an accurate measure of the energy of the electron-positron pair or the primary

² X_0 is the radiation length or the distance over which an electron energy is reduced by a factor $1/e$ due to radiation losses (see section 3.1.1).

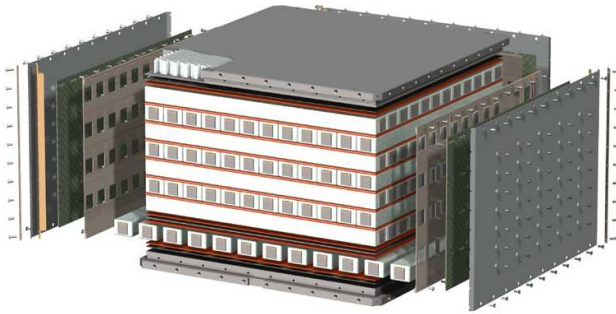


Figure 2.3. A schematic overview of a calorimeter module. The CsI(Tl) crystals are stacked so that the layers are rotated 90° with respect to adjacent layers. The signal from the crystals are read out with PIN diodes at both ends. The calorimeter module measures about $35 \times 35 \times 20$ cm³. From the LAT collaboration.

gamma-ray in the energy range 20 MeV–300 GeV, and to assist with cosmic-ray background rejection. It is a $8.5X_0$ deep, homogeneous calorimeter composed of 1536 scintillating CsI(Tl) crystals. The scintillation light from each CsI(Tl) crystal is detected at each end by PIN diodes, each crystal element is sensitive in the energy range 2 MeV–100 MeV.

A calorimeter module is composed of 8 layers of 12 CsI(Tl) crystals, each measuring $326.0 \times 26.7 \times 19.9$ mm³. Each layer is rotated 90° with respect to its neighbouring layers as shown in figure 2.3, forming an x - y array. This segmentation gives both longitudinal and transverse information about the energy deposition in the calorimeter, and enables it to determine the direction of the primary particles. This is important when the incident gamma-ray fails to convert in the tracker, although its imaging capability gives a much worse angular resolution than the tracker. At high energies (>1 GeV) the gamma-ray interaction probability in the tracker is about 33%. The segmentation also enables the calorimeter to separate between electromagnetic and hadronic showers, so that the calorimeter can assist in hadronic background rejection. The imaging capabilities of the calorimeter is further discussed in section 3.5.

The mass of the GLAST calorimeter will be about 1500 kg and will be the largest calorimeter launched into space. It constitutes about 60% of the total GLAST mass which is about 2500 kg. One of the challenges during the development of the GLAST calorimeter has been to construct a mechanical structure that supports the CsI crystals securely during launch while still allowing for thermal expansion and contraction without putting too much stress onto the crystals. It is also important to minimise the amount of dead space and material between the tracker and the calorimeter, and between the calorimeter modules. The resulting support structure

is made up of a stack of carbon-fiber cells, each containing one crystal. The crystals are wrapped in a highly reflective specular film (VM2000) in order to achieve high light collection efficiency, before inserted into a cell. The crystal is held in place by end-caps mounted around the PIN diode which are attached to the cell, and elastic bands along the chamfered edges will keep the crystal steady and allow it to expand and contract inside the cell.

2.3.3 Anticoincidence detector

The Anticoincidence Detector (ACD) [11] is an outer layer covering the LAT and is sensitive to charged particles. It makes the initial distinction between gamma-ray signals and “false” signals such as charged particle cosmic-rays, which outnumber the gamma-rays by a factor of 10^4 , and Earth albedo particles.

The ACD consists of an array of 1 cm thick plastic scintillator tiles, each tile being read out by wavelength-shifting fibers and miniature photomultiplier tubes. The tiles cover the top and sides of the tracker array (see figure 2.1), but not the sides or back of the calorimeter. The ACD tiles covering the top are about 1000 cm^2 , and the closer to the calorimeter they are placed the smaller the size of the tiles. The smallest tiles measure about 200 cm^2 . Figure 2.4 shows a curved top tile with wavelength-shifting fibers.

The ACD is designed to reject charged particles. The segmentation of the ACD avoids self-veto from “backsplash” caused by high-energy gamma-rays. Backsplash is when particles created in the calorimeter by the incident gamma-ray are scattered backward. These particles can cause a veto signal in the ACD, mistaking the gamma-ray for a background event. The EGRET instrument had a single ACD



Figure 2.4. A curved top ACD scintillator tile. Credit: David Thompson.

shield and suffered a loss of nearly 50% in detection efficiency at 10 GeV due to this effect [12]. The smaller tiles covering the sides of the instrument are used to achieve a lower self-veto rate from calorimeter backslash from events entering the tower from the side.

The ACD tiles will be supported on a frame attached to the grid, and the large top surface will be anchored to the top of the tracker via snubbers located at the tower corners to protect the ACD shield during launch.

2.3.4 Data acquisition system

The large amount of data that is accessible from the detectors cannot all be transferred to the ground, due to the limited transfer rate. Therefore the instrument data must be collected and processed on board, applying filters and algorithms so that only the most useful information is transferred to the ground. The filtering process must be able to separate the primary gamma-rays, originating from sources in the universe, from mainly cosmic-rays, but also from secondary gamma-rays from the interaction of cosmic-rays with the Earth's atmosphere.

There are three levels of triggers, where the first level trigger (L1T) coordinates the signals from the tracker, ACD and calorimeter. A L1T will be issued if there is a signal in 3 consecutive x - y silicon pairs in the tracker, indicating a particle event, or if the calorimeter register an energy deposition above a set threshold. A veto is applied if an ACD tile associated with a TKR hit fires, or if more than three ACD tiles fire. Level 1 also checks if there is a signal in the ACD indicating a background event. When L1T is issued it initialises readout from the other detector subsystems within 20 μ s. The second level trigger (L2T) is a tower-level function and refines the output of the L1T, by checking that the produced tracks in the silicon planes are somewhat aligned in order to remove triggers due to stochastic noise. Further, it applies a fast algorithm to extrapolate track candidates and match it with an ACD tile, eliminating the charged particle background. The level 3 trigger (L3T) does a complete event reconstruction using data from the entire instrument. The main purpose is to do very loose cuts to reduce background events, such as gamma-rays originating from the Earth albedo.

2.3.5 Gamma-ray burst monitor

The primary objectives of the GLAST Burst Monitor (GMB) [13] is to provide a large field-of-view for localising gamma-ray bursts. The instrument is sensitive in the energy range 10 keV–30 MeV. It consists of 12 Sodium Iodide (NaI) scintillation detectors and 2 Bismuth Germanate (BGO) scintillation detectors. The NaI detectors cover the lower part of the energy range, from a few keV to about 1 MeV and provide burst triggers and locations. The BGO detectors cover the energy range of about 150 keV to 30 MeV, providing a good overlap with the NaI at the lower end, and with the LAT at the high end. The detectors are located at opposite sides

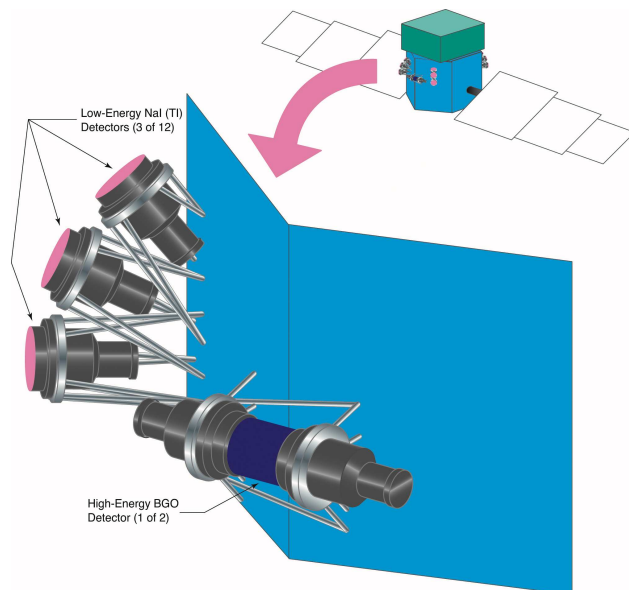


Figure 2.5. The Gamma-ray Burst Monitors are placed on the sides of the GLAST spacecraft, covering a wide range of the sky. From the GBM collaboration.

of the spacecraft, placed in such a way that they sample a wide range of the sky. Figure 2.5 shows the detectors and their placing on the GLAST spacecraft.

The angular resolution of GBM is much worse than for the LAT instrument, but the idea is to notify LAT when and where a gamma-ray burst has occurred, providing the possibility of relocating the GLAST spacecraft to measure the burst. The GBM's ability to quickly locate bursts will also be used to initiate counterpart searches by ground or other space-based observers.

GLAST will provide alerts when gamma-ray bursts or flaring objects are detected, so that the ground-based detectors can redirect.

Chapter 3

Energy measurements using crystal calorimeters

The most important features of a calorimeter are proportionality of the signal to the incident particle energy, sufficient size in order to allow the energy to be fully absorbed, and a high energy conversion efficiency. Energy leakage through the calorimeter boundaries have large effects on the energy resolution, and often determines the calorimeter design. Ground-based detectors allow the construction of large calorimeters, but in space applications there are practical limitations to the size and weight of the detectors.

There are two main types of calorimeters, *homogeneous calorimeters* which are fully active, and *sampling calorimeters* which consists of alternating active detector layers and passive dense layers. The main advantage of the homogeneous calorimeters is their excellent energy resolution, which is due to the fact that the whole energy of an incident particle can be deposited in the active detector medium. In sampling calorimeters, however, the energy lost in the passive layers vary statistically from event to event, leading to so-called “sampling fluctuations” which have considerable influence on the energy resolution. The advantage with sampling calorimeters is that they can be made more compact by using dense material in the absorber layers.

In order to understand how the energy of the particle can be measured in the calorimeter, it is necessary to describe the basic interactions that transfer the energy of the incident particle to the detector material.

3.1 Particle interactions in the calorimeter

The energy of the particle is transferred to the detector through the interactions with the material. A high-energy electron or positron, or photon will undergo a series of interactions until all its energy is dissipated in the calorimeter. The charged

electrons and positrons interact differently with matter than the neutral photons and, in addition, for one and the same particle different interaction processes at different energies may be relevant. The following, if no other references are stated, is based on the presentation of Leroy and Rancoita [14].

3.1.1 Interactions of charged particles

Charged particles passing through matter lose energy by ionising and exciting the atoms through inelastic collisions with atomic electrons. This is usually referred to as *ionisation* or *collision losses*. A charged particle can also lose energy by emitting photons when decelerating in the electric field of a nucleus, so called *radiation losses*. The total energy loss can thus be written as

$$\left(\frac{dE}{dx}\right)_{tot} = \left(\frac{dE}{dx}\right)_{coll} + \left(\frac{dE}{dx}\right)_{rad}. \quad (3.1)$$

Ionisation loss

The collision energy loss (per g/cm²) of a particle in a material with atomic number Z and mass A (in g/mol), is determined by the well-known Bethe-Bloch formula

$$-\left(\frac{dE}{dx}\right)_{coll} = kz^2 \frac{Z}{A} \frac{1}{\beta^2} \left[\ln \frac{2m_e c^2 \beta^2 E_{max}}{\bar{I}^2 (1 - \beta^2)} - 2\beta^2 - \delta - \frac{2C}{Z} \right] \quad (3.2)$$

where z and $\beta = v/c$ are charge and velocity of the particle, and

$$k = 2\pi r_e^2 N_A m_e c^2,$$

where r_e is the classical electron radius, N_A is Avogadro's number, m_e the electron rest mass. \bar{I} is the mean ionisation potential of the material, and E_{max} is the maximum energy transfer in a single collision. At non-relativistic velocities, the energy loss dE/dx is determined by the term $1/\beta^2$, decreasing rapidly as the velocity increases. When $\beta \approx 0.95$, the energy loss reaches a minimum. As the velocity further increases, the energy loss starts to increase again due to the logarithmic term in equation 3.2. This is often referred to as the relativistic rise. However, as the velocity increase the electric field of the particle polarises the atoms along its path, reducing the electric field strength acting in distant electrons. The term δ is a correction for this “density effect”, so called because the charged particle sees less nuclei due to the screening by the atomic electrons. It causes a suppression of the relativistic rise. The shell correction, C , accounts for effects arising as the velocity of the incident particle becomes comparable to the orbital velocity of the bound electron.

The Bethe-Bloch formula must be modified somewhat in the case of electrons and positrons. Due to their small mass, the incident particle does not remain undeflected during collisions as assumed in the formula above. Also, collisions

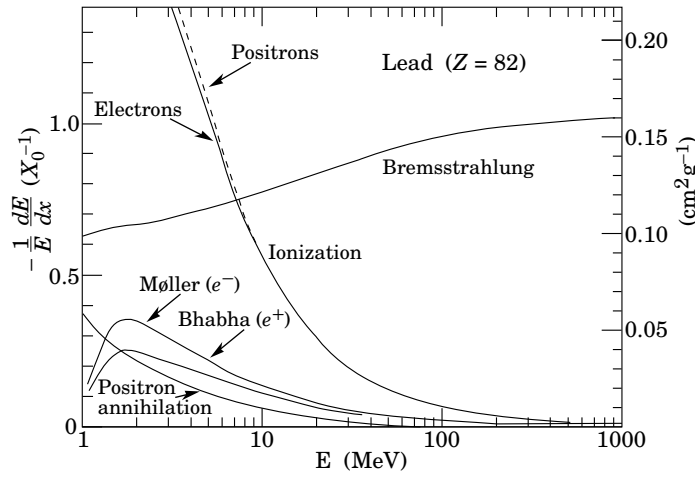


Figure 3.1. Fractional energy loss per radiation length in lead as a function of electron or positron energy. X_0 is the radiation length, and is defined in equation 3.5. Figure from [15].

occur between identical particles so that the maximum energy transfer becomes $E_{max} = T_e/2$ where T_e is the kinetic energy of the incident electron. The Bethe-Bloch formula then becomes

$$-\left(\frac{dE}{dx}\right)_{coll} = k \frac{Z}{A} \frac{1}{\beta^2} \left[\ln \frac{\tau^2(\tau+2)}{2(\bar{I}/m_e c^2)^2} + F(\tau) - \delta - \frac{2C}{Z} \right], \quad (3.3)$$

where $\tau = T_e/m_e c^2$, and

$$\begin{aligned} F(\tau) &= 1 - \beta^2 + \frac{\tau^2 - (2\tau+1)\ln 2}{(\tau+1)^2} && \text{for } e^- \\ F(\tau) &= 2 \ln 2 - \frac{\beta^2}{12} \left[23 + \frac{14}{(\tau+1)} + \frac{10}{(\tau+1)^2} + \frac{4}{(\tau+1)^3} \right] && \text{for } e^+ \end{aligned} \quad (3.4)$$

Figure 3.1 shows the energy loss for electrons and positrons in lead as a function of energy.

Radiation loss: Bremsstrahlung

A charged particle can also lose energy by emission of electromagnetic radiation or *Bremsstrahlung* when decelerating in the electric field of a nucleus. The emission probability is proportional to Z^2/m^2 , where m is the mass of the particle. Hence, it becomes an important source of energy loss for low-mass particles like electrons and positrons already at a few tens of MeV (see figure 3.1). Neglecting the field

from the atomic electrons, the radiation loss in high- Z materials can be expressed by

$$-\left(\frac{dE}{dx}\right)_{rad} = 4\alpha r_e^2 \frac{N_A}{A} Z(Z+1) E_e \left(\ln \frac{183}{Z^{1/3}} + \frac{1}{18} \right), \quad (3.5)$$

where E_e is the kinetic energy of the electron, α the fine-structure constant. For each material we can define a *critical energy*, E_c , at which the radiation losses equal the collision losses. An approximate formula for E_c in solids is given in [15] as

$$E_c \approx \frac{610 \text{ MeV}}{Z + 1.24}. \quad (3.6)$$

It is convenient to introduce a quantity called *radiation length*, X_0 , to measure typical distances traveled while radiative emission occurs. The radiation length is the distance over which the electron has reduced its energy by a factor $1/e$ due to radiation losses only. The radiation length is given by

$$\frac{1}{X_0} = 4\alpha r_e^2 \frac{N_A}{A} Z(Z+1) \ln \frac{183}{Z^{1/3}}. \quad (3.7)$$

On average (it is a statistical process), the electron (positron) will radiate one photon per radiation length.

3.1.2 Interactions of photons

Interactions of photons are fundamentally different from ionisation processes of charged particles because in every interaction the photons is either completely absorbed or scattered. Since the absorption or scattering is a statistical process, it is not meaningful to define a range for photons. Instead, a beam of photons with initial intensity I_0 passing through a material of thickness, x (cm), will be attenuated exponentially according to

$$I = I_0 e^{-\mu x}, \quad (3.8)$$

where μ (cm^{-1}) is the linear attenuation coefficient of the material. The attenuation coefficient describes the absorbing or scattering properties of the material for a given photon energy. It depends on the density of the material, ρ , and the cross section σ_i for the process i as

$$\mu = \frac{N_A}{A} \rho \sum_i \sigma_i, \quad (3.9)$$

where N_A is Avogadro's number and A is the atomic mass. There are three main interaction processes by which photons interact with matter:

Photoelectric effect

An atomic electron can absorb the energy of an incident photon completely, after which it is ejected with a resulting energy equal to the difference between the photon

energy and its binding energy. The photoelectric cross section strongly depends on the atomic number Z of the material, and in the non-relativistic range it is

$$\sigma_{ph} \propto \frac{Z^5}{E_\gamma^{7/2}}. \quad (3.10)$$

For high energies ($E_\gamma \gg m_e c^2$), the energy dependence is much less pronounced

$$\sigma_{ph} \propto \frac{Z^5}{E_\gamma}. \quad (3.11)$$

The photoelectric effect is the dominating process at lower energies.

Compton scattering

The Compton effect describes the scattering of photons off atomic electrons. In the treatment of this process the binding energy is neglected and the electrons are considered as free. At high energies ($E_\gamma \gg m_e c^2$) the Compton cross section is approximately

$$\sigma_C \propto \frac{Z \ln E_\gamma}{E_\gamma}, \quad (3.12)$$

while at low energies ($E_\gamma \ll m_e c^2$) the cross section for Compton scattering reduces to the classical Thomson scattering cross section, i.e. depending only on the classical radius of the electron. Compton scattering is important at energies of a few MeV for high- Z materials.

Pair production

In the pair production process, a photon is converted into an electron-positron (e^-e^+) pair. This can only occur in the presence of a nucleus in order to conserve momentum, and in order to create a pair the photon must have an energy larger than 1.022 MeV (i.e. $2m_e$). The recoil energy of the nucleus can be neglected since $m_{nucl} \gg m_e$. The probability of pair production increases slowly with incident energy, and depends on the atomic number as

$$\sigma_{pair} \propto Z^2 \ln 2E_\gamma. \quad (3.13)$$

For photon energies such that $E_\gamma \gg \frac{m_e c^2}{\alpha Z^{1/3}}$ the screening is total and the cross section can be expressed as

$$\sigma_{pair} \approx \frac{7}{9} \frac{A}{N_A} \cdot \frac{1}{X_0}, \quad (3.14)$$

i.e. the cross section at high energies is independent of the incident photon energy. X_0 is the radiation length defined in equation 3.7. Pair production is the dominating

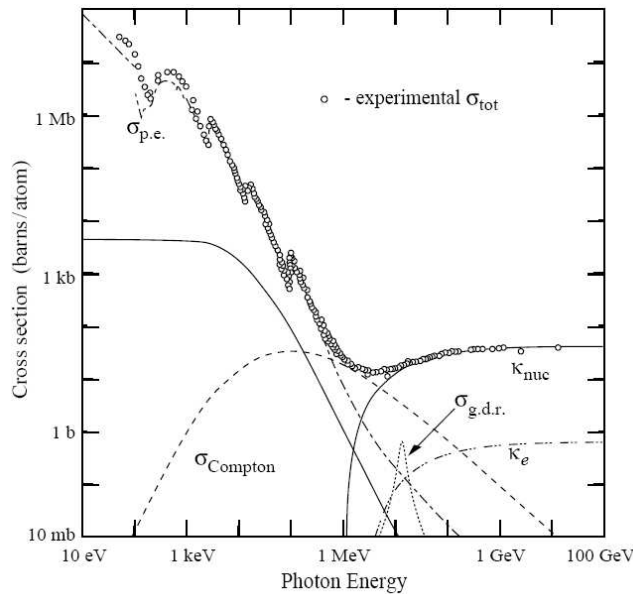


Figure 3.2. Total photon cross section as a function of energy in lead. From [15].

process above a few 100 MeV, and for most dense materials the probability of pair production reaches its maximum value around a few GeV and does not grow further. Equation 3.14 also implies that the mean free path of a high-energy photon for pair production is $9/7$ of a radiation length.

The opening angle of the electron-positron pair has been calculated analytically [16, 17], and the most probable opening angle is found to be of the order

$$\theta_{pp} \approx \frac{m_e c^2}{E_\gamma}. \quad (3.15)$$

From this relation the opening angle θ of the electron-positron pair can be used to estimate the photon energy. The recoil of the nucleus following pair production can be neglected for photon energies above 1 GeV.

As discussed above, the most important interaction for high-energy photons ($\gtrsim 100$ MeV) in matter is pair production. Low-energy photons are most likely to interact through Compton scattering or photoelectric absorption. Figure 3.2 shows how the photoelectric effect, Compton scattering and pair production contribute to the total cross section in lead. It also shows two additional processes which contribute less: Rayleigh scattering and photonuclear absorption. The former concerns photons that scatter without exciting or ionising the atom, and the latter

absorption of the photon by a nucleus. These two effects contribute little to the total cross section.

3.2 Electromagnetic showers

A high-energy ($\gtrsim 100$ MeV) photon striking some material will interact almost exclusively by pair production creating a high-energy e^+e^- pair. These will in turn have enough energy to produce bremsstrahlung photons, which again undergo pair production, etc. An alternating sequence of bremsstrahlung and pair production lead to a multiplication of the number of electrons, positrons and photons in what is referred to as an *electromagnetic shower*. In the final stages of the multiplication process, low-energy photons and electrons/positrons are generated. These photons mainly interact via the photoelectric process, while the electrons/positrons, including the photoelectric electrons, dissipate their energy through collisions. In this way the incoming particle energy is gradually absorbed by the calorimeter medium.

The behaviour and properties of an electromagnetic shower can be understood in a very simplified model [18]. Let E_0 be the energy of a photon incident on a calorimeter. After one radiation length the photon produces an e^+e^- pair of equal energies (the mean free path for a photon to undergo pair production is in fact $9/7X_0$, but is for simplicity here assumed to be $1X_0$). After further one radiation length the electron and positron emit one bremsstrahlung photon each, which again after one additional radiation length again transforms into e^+e^- pair. By continuing the process, and assuming equal energy sharing among the generated particles, the number of particles will double themselves every radiation length. This crude model of an electromagnetic shower is depicted in figure 3.3, where $t = x/X_0$ is the depth in units of the radiation length X_0 . The number of particles at a depth t is

$$N(t) = 2^t, \quad (3.16)$$

and their energy is given by

$$E(t) = \frac{E_0}{N(t)}. \quad (3.17)$$

The multiplication of the shower continues as long as $E > E_c$, the critical energy. Below E_c , other processes like ionisation for electrons, and Compton scattering and photoelectric absorption for photons become important and the production of particles stop. Hence, the location of the shower maximum, t_{max} , occurs when the energy equals the critical energy, so that

$$E_c = \frac{E_0}{2^{t_{max}}}, \quad (3.18)$$

which gives

$$t_{max} = \frac{\ln \frac{E_0}{E_c}}{\ln 2}. \quad (3.19)$$

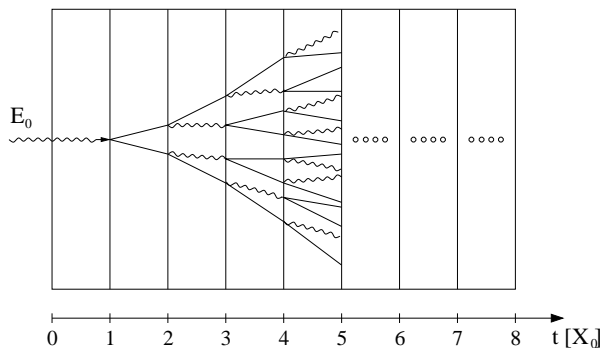


Figure 3.3. A simple model of an electromagnetic shower. The wavy lines are photons, and the straight are electrons and positrons.

The number of particles at the shower maximum is

$$N_{max} = 2^{t_{max}} = \frac{E_0}{E_c}. \quad (3.20)$$

From this crude estimation of the properties of electromagnetic shower the following is found

1. The location of the shower maximum changes logarithmically with E_0 .
2. The number of particles in the shower is proportional to E_0 .

The theory of cosmic-ray showers was first put forward in 1937 by two independent papers by Bhabha and Heitler [19], and Carlson and Oppenheimer [20]. In a simplified analytical model of cascade development referred to as “Approximation B”, Rossi and Griesen (1941) [21] predicted the number and energy distributions of electrons and photons over about 5 MeV. In their calculations the Compton effect is neglected, the collision loss is described as a constant energy dissipation equal to the critical energy, E_c , and the bremsstrahlung and pair production is described by the expression of complete screening. The techniques for Monte Carlo simulation of electromagnetic cascades were developed by Butcher and Messel (1960) [22], and independently by Varfolomeev and Svetlilobov [23].

3.2.1 Longitudinal development of electromagnetic showers

The longitudinal shower profiles in various media have been studied both experimentally and through simulations (e.g. [24, 25]). Recent simulation studies of electromagnetic showers exist, where the average longitudinal distribution for electron-induced showers has been systematically studied up to about 100 GeV [15, 26]. The

shower energy deposition maximum was found to be located at [15]

$$t_{max} = 1.0 \left[\ln \frac{E}{E_c} + C_j \right] [X_0], \quad (3.21)$$

where $C_e = -0.5$ and $C_\gamma = +0.5$ for electron- and photon-induced showers, respectively. This is similar to the results obtained by Rossi in the context of Approximation B.

The mean longitudinal profile of the energy deposition in an electromagnetic shower is approximately described by the Gamma distribution (see e.g. [27])

$$\frac{dE}{dt} = E_0 b \frac{(bt)^{a-1} e^{-bt}}{\Gamma(a)}, \quad (3.22)$$

where t is given in radiation lengths, a an energy-dependent parameter and b a Z -dependent parameter varying slowly with energy [15]. E_0 is the initial energy of the particle, Γ is the Gamma function. The shower maximum is then given by

$$t_{max} = \frac{a-1}{b}. \quad (3.23)$$

For the design of a calorimeter the longitudinal and lateral shower development is of great importance. On average, the cascade deposits 98% of the energy of the incoming particle within [28]

$$L(98\%) \simeq 2.5 t_{max} [X_0] \quad (3.24)$$

for energies in the region 10 GeV to 1000 GeV.

At very high energies the development of electromagnetic cascades in dense media is influenced by the Landau-Pomeranchuk-Migdal (LPM) effect [29, 30]. This effect predicts that the production of bremsstrahlung photons by high-energy electrons is suppressed in dense media. Suppression affects showers in several ways: the shower is elongated, and the radiation length increases. Because suppression reduces the number of photons emitted by the electron, electrons will behave more like heavier particles, such as muons and pions. Experimental measurements of the bremsstrahlung energy loss of 149 GeV, 207 GeV and 287 GeV electrons in thin Ir, Ta, and Cu targets have been performed by Hansen et al. [31]. Good agreement between simulations based on Migdal's theory and data from the experiment is found, indicating that the LPM suppression is quite well understood. For a review of the LPM effect and additional experiments see e.g. [32].

3.2.2 Lateral development of electromagnetic showers

The lateral development of the cascade is determined by several physical processes that generate secondary electrons and photons which are no longer aligned with the incoming particle direction. At high energies the angular spread is due to the opening angles in bremsstrahlung and pair production, whereas at lower energies close

to the critical energy, multiple scattering dominates the lateral shower expansion. The angular divergence for the processes mentioned above decreases with increasing energy, and this results in two components for the lateral profile: a narrow, central core due to the high-energy particles and a peripheral part spreading out as the shower penetrates deeper and low-energy particles are created.

Since it is mainly the low-energy particles that are responsible for the spread of the shower in the lateral direction, the width can be measured in a unit that depends only on the material and the Coulomb scattering from low-energy particles of the shower. This unit is called Molière radius, R_M , and is defined as the average lateral spread undergone by an electron of energy E_c traversing one X_0 of material:

$$R_M = \frac{21.2 \text{ MeV}}{E_c} X_0, \quad (3.25)$$

However, the radial development shows two different mechanisms that contribute to the transverse distribution [33, 24]. There is a central part of the radial energy profile that falls off steeply from the shower axis and that scales as R_M . Further out from the shower centre the energy distribution flattens out. Still, 95% of the total shower energy is contained within a cylinder of radius [34]

$$R(95\%) \simeq 2R_M \quad (3.26)$$

Values of the Molière radius and the radiation length of various materials are given in table 3.1.

The evolution of the radial function with increasing shower depth has been mapped using simulations and experimentally measured [24]. Simulation studies

Table 3.1. Properties of some absorber materials. The critical energy, E_c is calculated from equation 3.6 and the Molière radius, R_M , from equation 3.25.

Material	Z	ρ (g/cm ³)	E_c (MeV)	X_0^a (g/cm ²)	X_0/ρ^a (cm)	R_M (cm)
Hydrogen	1	0.08	350	63	700000	42400
Aluminum	13	2.70	43	24	8.9	4.4
Copper	29	8.96	20	12.9	1.43	1.5
Tungsten	74	19.3	8	6.8	0.35	0.9
Lead	82	11.35	7	6.4	0.56	1.7
CsI(Tl)	54	4.51	11	8.39	1.85	3.8
NaI(Tl)	45.8	3.67	13	9.49	2.59	4.5
BGO	59.9	7.13	10	7.97	1.12	2.4
Air	7.3	1.2	84	37	30000	7500

^aFrom [15]

by Grindhammer and Peters [35] show that the lateral development as a function of depth can be parametrised with a two component function [35]

$$f(r) = p(t) \frac{2rR_C^2(t)}{(r^2 + R_C^2(t))^2} + (1 - p(t)) \frac{2rR_T^2(t)}{(r^2 + R_T^2(t))^2} \quad (3.27)$$

where t is the depth, $R_C(t)$ and $R_T(t)$ are the median of the core component and tail component respectively, and $p(t)$ is the relative weight ($0 \leq p(t) \leq 1$).

3.3 Hadronic showers

Although the subject of this thesis is electromagnetic showers, a short summary of the properties of hadronic showers is given for completeness. If the incident particle is a hadron (mainly protons in cosmic-rays) it may also participate in strong interactions with the nuclei of the material resulting in a *hadronic shower*. The hadronic cascade is far more complex than the electromagnetic since hadrons undergo inelastic hadronic interactions with the nuclei in the detector material, resulting in a wide variety of particles and nuclear reactions. For more detailed information on hadronic showers see e.g. [14, 36, 37] There are no simplified analytical treatments available. The secondary products are mainly charged and neutral pions, and with lower multiplicities also kaons, nucleons and other hadrons like protons and neutrons. The length scale relevant for hadronic cascades is the nuclear interaction length, given very roughly by [15]

$$\lambda_I \approx 35A^{1/3}, \quad (3.28)$$

which is large compared to the length scale of radiation length, X_0 , governing the electromagnetic cascades. Therefore, hadronic calorimeters are required to be much larger than the electromagnetic ones. The shower maximum is given by [28]

$$t_{max} \approx 0.2 \ln E + 0.7, \quad (3.29)$$

where the energy is in GeV. The lateral profile is similar to the electromagnetic case with an energetic core surrounded by lower-energy particles, and [28]

$$L(95\%) \approx \lambda_I. \quad (3.30)$$

There are two additional features which give the hadronic cascade a different profile in the calorimeter

- i) A considerable part of the secondaries are π^0 's, which will decay into two photons, $\pi^0 \rightarrow \gamma\gamma$, before having a chance to re-interact hadronically, inducing electromagnetic cascades.
- ii) A non-negligible amount of the available energy is converted into excitation or break-up of the nuclei, of which only a fraction will result in detectable, or “visible”, energy. In addition, long lived or stable neutral particles like neutrons and neutrinos can escape from the calorimeter.

The average fraction of π^0 's (of the order 20%) increases with increasing primary energy of the incident hadron, but the size of the π^0 component may fluctuate considerably from event to event depending on the first interaction. Thus, the visible energy will fluctuate between more electromagnetic-like showers and fully hadronic showers with a maximum of invisible energy.

For comparison, a typical electromagnetic and a typical hadronic shower are shown in figure 3.4.

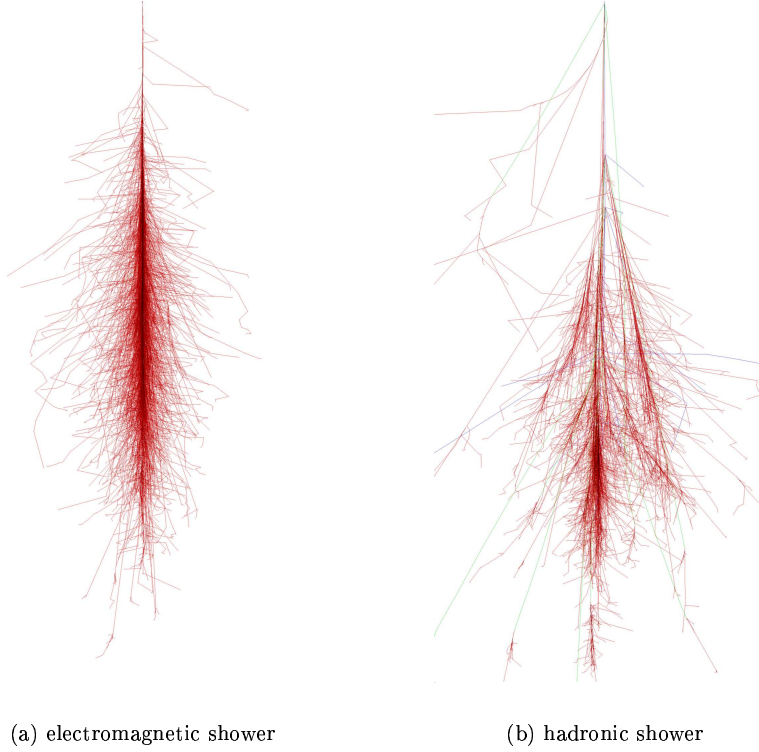


Figure 3.4. (a) An electromagnetic shower induced by a 50 GeV photon in air. (b) A hadronic shower induced by a 50 GeV proton in air. Both are from [38]

3.4 Energy resolution

Ideally, the energy measured in a calorimeter is proportional to the incident particle energy, E . The intrinsic energy resolution of a calorimeter is limited by the statistical fluctuations of the elementary processes converting the initial energy to a detectable signal. The energy resolution can therefore be written as

$$\left(\frac{\sigma(E)}{E}\right)_{intrinsic} \propto \frac{1}{\sqrt{E}}. \quad (3.31)$$

Because of the statistical nature of calorimetry, the accuracy improves with increasing energy. In most detectors, however, there are a number of other factors that affect the energy resolution. This is often expressed as (see for instance [36])

$$\frac{\sigma(E)}{E} = \frac{a}{\sqrt{E}} \oplus \frac{b}{E} \oplus c, \quad (3.32)$$

where the symbol \oplus indicates a quadratic sum. The first term is called the *stochastic term*, and includes the statistic-related intrinsic shower fluctuations, photoelectron statistics, dead material, and sampling fluctuations (in the case of sampling calorimeters). The stochastic term is usually small in scintillation calorimeters thanks to the rather low energy needed to create a scintillation photon, and is of the order of a few percent in homogeneous CsI(Tl) calorimeters (see e.g. [39, 40]). The light yield, i.e. the number of photons produced per MeV of energy deposition, should be large enough to minimise the contribution of the statistical fluctuations to the energy resolution. The CsI(Tl) crystal has a rather high light yield compared to other scintillators (see table 4.2). Nevertheless, it is important to minimise inefficiencies in light collection, arising from photon self-absorption, bad spectral matching between crystal and photosensor, or bad optical coupling (see section 4.2.3). Sampling electromagnetic calorimeters usually have intrinsic energy resolutions in the range 5-20% \sqrt{E} [36].

The second term is called the *noise term* and comes from the electronic noise of the readout chain. It depends on the detector technique and on the features of the readout circuit (detector capacitance, cables, etc.). With an increased segmentation position resolution increases but at the same time readout noise also increases due to the larger number of unused readout channels. The noise contribution to the energy resolution increases with decreasing energy.

The *constant term* includes contributions that do not depend on the energy of the particle, often it is instrumental effects causing variations of the calorimeter response. Examples are non-uniform production of scintillation light along the crystals, temperature gradients, detector aging, radiation damage, etc. The constant term often dominates the resolution in homogeneous high-energy calorimeters because of the very small stochastic term, and should be kept at a low level. It is therefore important with frequent *in situ* calibration and monitoring.

Additional contributions to the energy resolution can be upstream energy loss due to non-negligible amount of inactive material before the active volume, and

cracks, gaps and dead regions inside the calorimeter may also contribute to the energy resolution.

3.5 GLAST calorimeter properties

Scintillation crystal calorimeters are often used in high-energy physics, and exist both as homogeneous and sampling calorimeters. Active electromagnetic calorimeters, where the showering material is also the detecting medium, give the best energy resolution. The EGRET calorimeter consisted of a single $76 \times 76 \times 20 \text{ cm}^3$ NaI(Tl) scintillator crystal, $8X_0$ deep [41]. It allowed energy measurements of gamma-rays in the range of 20 MeV to about 30 GeV, and had an energy resolution of about 20% (FWHM) over the central part of the energy range. The resolution became worse above several GeV due to incomplete absorption in the NaI calorimeter. The scientific objectives of GLAST, however, require a more sophisticated calorimeter with efficient background rejection of cosmic rays and good energy resolution. The performance requirements for the GLAST calorimeter, shown in table 3.2, and the limitations of space missions have influenced the choice of calorimeter design and material. CsI(Tl) is a fairly dense scintillator material with a short radiation length, and it is also ideal for PIN photodiode readout, since the PIN sensitivity range fully overlaps with the CsI(Tl) emission spectrum. This enables a more compact calorimeter, which is important in high-energy space missions where the instrument size is limited. CsI(Tl) also has a high light yield which is important in order to achieve a good energy resolution. Different scintillator materials will be discussed in more detail in chapter 4.

Table 3.2. GLAST calorimeter requirements. Data from [42].

Parameter	Requirement
Energy range	20 MeV–300 GeV
Energy resolution ^a	<20% (20 MeV < E < 100 MeV) <10% (100 MeV < E < 10 GeV) <20% (10 GeV < E < 300 GeV, on-axis) <6% (10 GeV < E < 300 GeV, off-axis > 60°)
Field of view ^b	>2.4 sr
Peak effective area	>8 000 cm ²
Background rejection	>10 ⁵ :1
Dead time	<20 μ s per event
Instrument lifetime	>5 years, with no more than 20% degradation.

^a 1σ

^bFWHM

The GLAST calorimeter and tracker together have a total depth of approximately $10X_0$, and the shower maximum can be contained within the instrument up to about 150 GeV (equation 3.21) for perpendicular incidence. If the gamma-ray enters the detector at an angle, the upper energy limit can be of the order of several hundred GeV.

3.5.1 Energy and position resolution

The resolution below 100 MeV is dominated by the energy resolution of the tracker since a considerable amount of the incident energy is deposited in the tracker, which has a much worse energy resolution compared to the calorimeter. At high energies (>10 GeV) the energy resolution is dominated by energy leakage from the back of the calorimeter.

One of the greatest differences between the EGRET and GLAST calorimeters is that GLAST has a segmented design instead of a single crystal. The scintillation light is measured at both ends of the crystal log, and the difference in the amount of light collected at each end, the so called light asymmetry, provides a determination of the position of the energy deposition along the crystal log. The light asymmetry is defined as the difference in light output from the two ends divided by their sum. The position resolution has been measured to be a few millimetres for low energy depositions ($\simeq 10$ MeV), and a fraction of a millimetre for large energy depositions (>1 GeV) [43]. The positioning possibility in a single crystal combined with the multi-layer construction allow a three-dimensional reconstruction of an electromagnetic shower in the calorimeter. Thus, the calorimeter alone can image the gamma-ray sky, although with much worse angular resolution than the silicon tracker. This is important at higher energies where photon can reach the calorimeter without undergoing pair conversion in the tracker.

The segmentation enables identification of the shower maximum in order to estimate the energy of the incident particle. It is also possible to correct for shower leakage from the calorimeter boundaries. Some of the methods employed in the energy reconstruction algorithms of GLAST will be described and further discussed in chapter 6. The imaging capability can also be used for background rejection through the condition that the electromagnetic shower should match with the pair conversion tracks in the tracker, and by discrimination between electromagnetic and hadronic showers.

In order to obtain good spatial resolution, the size of the crystal elements should be chosen to be smaller than the Molière radius which is 3.8 cm in CsI. In this way the lateral spread of the electromagnetic cascade is measured in several crystal modules (recall equation 3.26), allowing a reconstruction of the impact point of the incident particle from the shower axis of the electron and the positron. However, the dimensions of the crystals have to allow sufficient light yield, and be compatible with light transmission properties and light attenuation length. It has been verified experimentally that long and narrow CsI(Tl) crystals with GLAST-like dimensions give acceptable light yield [44] and response uniformity over the crystal length [45].

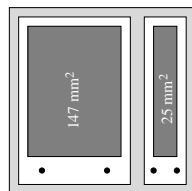


Figure 3.5. The dual PIN diode. The large active window covers the low-energy region and the small window the high-energy region.

The limit of segmentation is often a compromise between the spatial resolution and the number of readout channels whose number increases fast with the segmentation. As the number of channels increase, the readout noise will deteriorate the energy resolution.

3.5.2 Readout system

The scintillation light from the crystals are measured with dual PIN photodiodes mounted at both ends. Compared to photomultiplier tubes (PMTs), the PIN diodes have a good spectral match to the CsI(Tl) crystals, they are small, rugged, do not require high voltage and they are not sensitive to magnetic fields. The low power consumption is necessary since as a space mission, GLAST has a limited power supply.

The dual PIN diodes are custom-made and consists of two active windows on the same ceramic baseplate (figure 3.5), giving in total four diodes per crystal log. The dual configuration was implemented in order to obtain a high dynamical range of the readout of the scintillation light. The large area is 147 mm^2 and covers the low energy band whereas the small diode has an area of 25 mm^2 covering the high energy band. Each diode has a preamplifier and shaping amplifiers, and by using independent signal chains having different gain for the low- and high-energy ranges, a high dynamic range can be obtained. The low energy signal chain covers the energy range from 2 MeV to 800 MeV, and the high-energy signal chain covers the range from 40 MeV to 100 GeV. There is a significant overlap between the low- and high-energy range enabling cross-calibration of the electronics.

3.5.3 Calibration of the GLAST calorimeter

Changes in the calorimeter response may occur due to radiation damage of crystals and electronics, temperature changes or due to degradation of the PIN diode bonds, and therefore the calorimeter needs to be calibrated. The timescale of the interval between calibrations is of the order of weeks.

The GLAST calorimeter will be calibrated in orbit using heavy cosmic-ray ions (essentially C, N, O, Si and Fe). The ions have energies close to the minimum ionising part of the energy loss curve (equation 3.2), corresponding to about 2 GeV/nucleon. The ionisation energy deposited within the 1.99 cm thick CsI(Tl) crystals is therefore well-defined for the different ions. However, the light yield of the crystals is not strictly proportional to the energy deposit by the ions. This is due to ionisation quenching which is briefly discussed in section 4.1. Therefore, cosmic-ray calibration method requires prior knowledge of the response of the CsI(Tl) crystals to the relativistic ions of interest. The response of the GLAST calorimeter to heavy ions has been studied in a beam test [46].

Chapter 4

GLAST CsI(Tl) crystal elements

Detecting ionising particles by the scintillating light is one of the oldest techniques. Today, it is the most often and widely used particle detection method in nuclear and particle physics. Probably the earliest example of a scintillating detector is the spinthariscopes, invented by William Crookes in 1903 [47]. His device consisted of a small ZnS screen that produced weak scintillations when struck by α -particles.¹ Earlier devices for measuring radiation (e.g., photographic plates, electrometers, electroscopes) were integrating instruments, but the spinthariscopes detected individual decay events. However, the scintillations had to be counted by eye, a strenuous and tedious process with long periods of adaptation in the dark required before the researcher was ready. Still, it was used in the famous α -scattering experiment of Geiger and Marsden in 1909 [48], which led Rutherford to his model of the nucleus [49]. With the invention of the gaseous ionisation instruments, the optical scintillation counter fell into quick disuse. In 1944, Curran and Baker replaced the human eye with the then newly developed photomultiplier tube. The weak scintillations could now be counted with an efficiency and reliability equal to that of the gaseous ionisation instruments. The modern electronic scintillation detector was born.

This chapter describes the basic scintillation mechanism and the properties of inorganic scintillators. The effect of defects, non-uniform doping and radiation damage in the crystal will be discussed, followed by radiation damage tests of CsI(Tl) crystals.

¹The spinthariscopes soon became very à la mode amongst the London society, as it was small it easily fitted in a purse or a pocket. It also became a popular toy for children, like for instance the 1947 “Lone Ranger Atom Bomb Ring” which had a spinthariscopes and a polonium source attached to it, and came with a cereal box. In fact, the toy spinthariscopes is still sold today.

4.1 Crystal scintillators

There are two types of scintillators, the *organic*, for instance organic-based crystals, liquids and plastics, and the *inorganic* scintillators like crystals, ceramics, glasses and noble gasses. The scintillation mechanism in inorganic crystals are determined by electronic transitions in the crystal lattice, while in the organic the scintillation light is emitted as a consequence of de-excitations of molecular levels. In general, the inorganic scintillators have the best light output and linearity of the two, but are slow in their response time compared to the organic scintillators. In addition, because of high atomic number, Z , they have a high absorption ability of photons and are therefore suitable as high-energy gamma-ray detectors.

The inorganic scintillators can be divided into four main groups: halides, oxides, chalcogenides and glasses, where the alkali halide crystals, like NaI, CsI etc., are the most widely used.

The scintillation process is initiated with a particle losing energy to the material when passing through it, and the amount of scintillation light produced in the crystal depends on how much energy is deposited. A good approximation for inorganic scintillators is that the scintillating light is directly proportional to the energy deposited by the ionising particle. However, in reality some of the energy that would otherwise would go into luminescence is lost. According to equation 3.2 the ionisation density, i.e. the ionisation per unit length, increase with the incident particle mass and charge. However, as the ionisation density increase, less energy is transferred into scintillation light, a phenomenon is called *ionisation quenching* [50]. As a consequence, for same initial energy, heavy particles which deposits more energy per unit length yield less luminescence than electrons which deposits less. For example, the amount of light per unit energy deposited from an α -particle in CsI(Tl) is 67% of that of an electron [51]. This effect is present in both organic and inorganic scintillators, although it is of less extent in the latter.

4.1.1 Scintillation mechanism in inorganic crystals

The scintillation process has been widely studied since the beginning of the 20th century. However, the scintillation mechanisms are quite complex and are still not fully understood. The following is mainly based on the presentation of Birks [50] which also gives a good foundation for further reading, and Rodnyi [52] who presents the more recent advances in the field of scintillators.

The scintillation property of matter is called *luminescence*. If the energy absorbed by the scintillator is re-emitted immediately (within 10^{-8} s) the process is called *fluorescence*. When the re-emission is delayed because the excited state is metastable, the process is known as *phosphorescence*, or *afterglow*. Depending on the scintillating material, this delay between absorption and reemission can last from a few microseconds to hours.

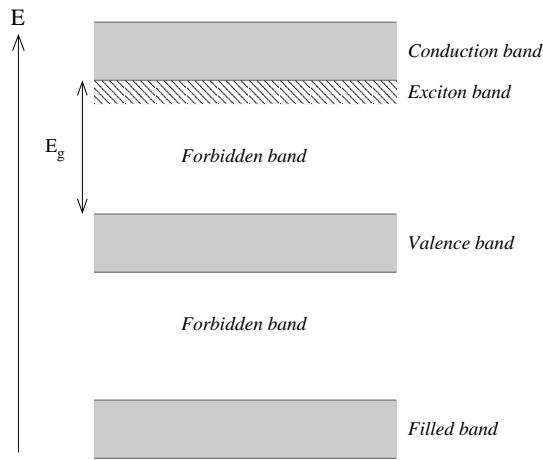


Figure 4.1. The energy band model of inorganic crystals.

Many of the inorganic scintillators used today are activated, that is their luminescence is due to a small concentration of impurities² added to the crystal melt during growth. These crystals are said to be doped, or *extrinsic*. In pure, or *intrinsic* crystals, the activator is not an added impurity, but an excess of the crystal constituents occupying positions between the lattice sites (interstitial ions). Although the intrinsic and extrinsic scintillators are similar in their interactions with ionising radiation, they differ in their scintillation processes, and as a result, in their properties as scintillators. The intrinsic scintillation process is very inefficient and only a few pure crystals are used in scintillation applications.

The periodic lattice of crystalline materials creates allowed energy bands for the electrons in the crystal. The energy of an electron is then confined to continuous “allowed” energy bands separated by “forbidden” energy gaps, as shown in figure 4.1. The lower filled band represent the inner-shell electrons of the lattice atoms, and the highest filled band is called the valence band, it corresponds to the outer-shell electrons (valence electrons). Electrons with sufficient energy to act as free electrons drift around in the upper conduction band. In semi-conductors the energy gap E_g between the valence and conduction band is sufficiently small for thermal excitation of electrons. In crystals, which are insulators, E_g is larger and the population of free electrons in the conduction band is negligible at room temperatures and in the absence of ionising radiation.

When the crystal is exposed to radiation it will either ionise lattice atoms or excite electrons along its path through the crystal. In the case of ionisation of lattice atoms, an electron is liberated and lifted to the conduction band, leaving the valence band with an empty state called *hole*. The neighbouring valence electron

²an impurity is an atom of other type than the host atoms

may jump from its bond to fill the hole, and if this is repeated, the hole appears to move. Since the hole is positive relative to the sea of negative electrons, the hole acts like a positive charge carrier and can be thought of as a particle, able to migrate through the crystal. When instead the radiation excites an electron, it remains bound to the hole forming a weakly coupled electron-hole pair, a so called *exciton*. It is also possible for electrons and holes already existing in the conduction band and valence band respectively, to form excitons. The energy state of the exciton lies just below the conduction band (see figure 4.1), and it behaves like a neutral particle, able to move freely through the crystal. It is common to include the exciton band when using the term conduction band.

The scintillation mechanism can be described as electronic transitions between the valence band and the conduction band, and can be summarised as the sequence of the following stages:

1. Absorption of ionising radiation and creation of secondary particles (electrons and holes, so called *e-h pairs*)
2. Relaxation of the secondary electrons and holes by production of tertiary e-h pairs
3. Thermalisation of the electrons and holes resulting in a number of e-h pairs with energy roughly equal to the bandgap energy
4. Energy transfer from the e-h pairs to the luminescence centres and their excitation
5. Emission of photons from the luminescence centres

The secondary electrons created by the incident radiation may further ionise the crystal atoms, producing a cascade of electrons and holes. This ionisation avalanche stops when the energy of the secondary, tertiary particles etc, is less than the ionisation threshold energy. At this point the electrons start to lose energy through interaction with crystal lattice vibrations. This is known as the *thermalisation stage*, and as the electrons lose energy they move down to the bottom of the conduction band. As a result, the e-h pair energy becomes equal to the band gap energy, E_g . Since the final result of all ionisation processes is creation of e-h pairs, the number of e-h pairs, N_{eh} , is proportional to the energy absorbed by the matter

$$N_{eh} = \frac{E_{abs}}{\xi_{eh}}, \quad (4.1)$$

where ξ_{eh} is the average energy required to create a thermalised e-h pair. ξ_{eh} is approximately $2E_g$ for ionic crystals. The excess energy of the e-h pairs lost during the thermalisation stage does not contribute to the scintillation light output, but is lost. Table 4.1 lists the size of the energy gap of some common inorganic crystals. After thermalisation, the electrons and the holes migrate in the crystal, a phase called the *migration stage*. The energy losses during the migration stage depend

Table 4.1. The band gap width in some common inorganic scintillators. From [52].

Scintillator	E_g (eV)
CsI	6.1
NaI	5.9
LiI	6.1
CaF ₂	12.2
BaF ₂	10.6

on the spatial distribution of electrons and holes relative to luminescence centres. The longer the charge carrier has to migrate before it encounters a luminescence centre, the greater is the probability to become captured by traps that hinders the luminescence process.

The luminescence centres can be either impurities, interstitial ions or lattice defects, and they introduce local discrete energy levels in the forbidden energy gaps due to the resulting electrical perturbation in the lattice. The excitation and emission of luminescence centres can be described by a diagram of the potential energy of the luminescence centre versus the mean distance between the luminescence centre and its surrounding ions. Figure 4.2 shows the potential energies of a luminescence centre in the ground state (curve 1) and excited state (curve 2). The change in the inter-atomic distance of the two states is due to the change in electric force between the luminescence centre and the lattice. Close to the equilibrium position of a state the potential can be described by a harmonic oscillator, having discrete vibration levels (shown as horizontal lines in figure 4.2). The minima A and B correspond to the stable energy positions in the two states. An excitation from ground to excited state occurs along the line AC and moves down to B through thermalisation and from there it can de-excite to D by luminescence emission. However, if thermal vibrations cause a displacement from the minimum potential energy position at B large enough to reach F. In that event a radiationless transition from the excited to the ground state can take place by heat dissipation, and the luminescence is quenched. The probability of this *thermal quenching* increases with temperature since it increases the thermal energy of the excited state and moves it up toward F.

The excitation of a centre requires the capture of an electron from the conduction band *and* the capture of a hole from the valence band, either simultaneously by the capture of an exciton, or by electron-hole recombination at a centre. The excited luminescence centres return to their ground states by emitting a photon, and this is the final stage of the scintillation process. The wavelength of the scintillation photon is determined by the energy levels of the luminescence centres, and therefore it is possible to tell which processes give rise to the scintillation light by studying the emission spectra. Usually the emission lies in the UV or visible-light range (see table 4.2 for the maximum emission wavelength of some common scintillators).

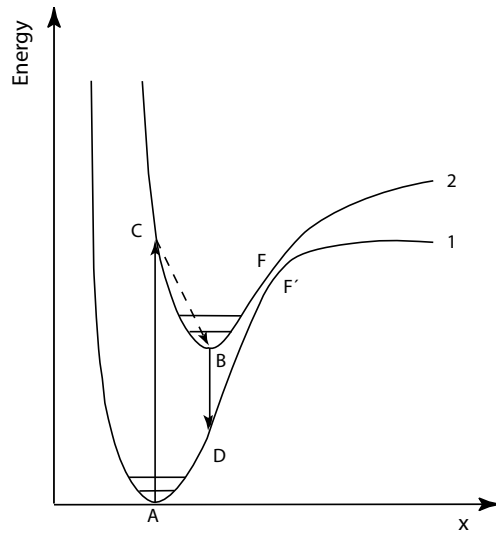


Figure 4.2. Potential energy diagram of the ground state (curve 1) and the excited state (curve 2) of a luminescence centre. x is the inter-atomic distance between the luminescence centre and its surrounding ions. The minima A and B corresponds to stable energy positions in the two states. FF' is the region of thermal quenching. Figure adapted from [50].

Lattice defects and trapping

The traps can be impurities and lattice defects in the crystal, introducing additional energy levels below the conduction band or above the valence band. Some of the traps can introduce energy levels near the middle of the forbidden gap and these are therefore referred to as deep traps, as opposed to those with energy levels close to the edges of the forbidden gap called shallow traps. The trapped electrons (or excitons) can return to the valence band by a nonradiative transition, or return to the conduction band by acquiring thermal energy from the lattice vibrations. The latter process results in afterglow, since the particle can participate in the scintillation process.

Defects at the atomic scale in crystals are at least of three types. The first is when an atom is missing from a lattice site, forming an atomic vacancy. A second type of defect is when an impurity is present at a lattice site. Finally, an extra atom might be situated at an interstitial site between the lattice sites. Since these defects constitutes a perturbation in the overall charge neutrality in the lattice, electrons or holes can be captured. For example, a missing *anion*, a negative lattice ion, leaves an area of positive ions which is an effective trap for electrons. When the anion vacancy captures an electron it is called *F-centre*, shown in figure 4.3. The electron in an *F-centre* can undergo photo-induced transitions between discrete

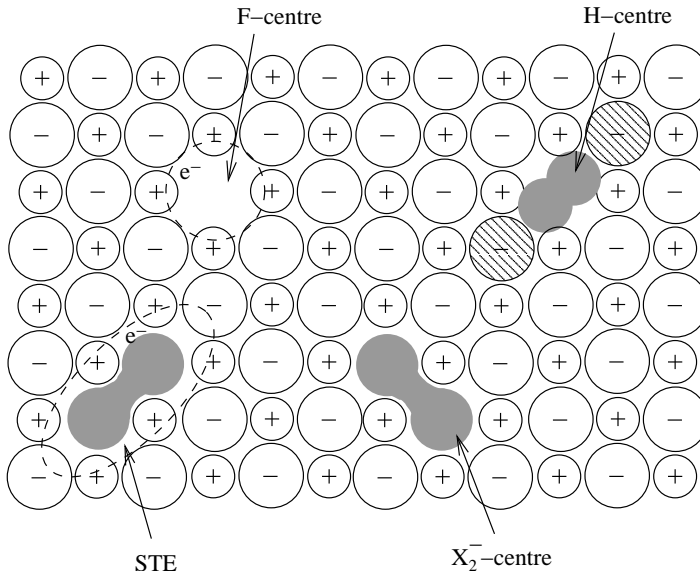


Figure 4.3. Trapping centres in crystal lattice. Shaded parts illustrate anions involved in the trapping centres. Trapped electrons are illustrated by dotted lines. Figure from [52].

energy levels, leading to optical absorption in the visible part of the spectrum, and therefore it is also called colour centre (F refers to *farbe*, the German word for colour). In principle, the counterpart of an *F*-centre, i.e. a hole trapped at a *cation* (positive lattice ion) vacancy and denoted *V*-centre should also exist. However, it appears to be unstable in alkali halides.

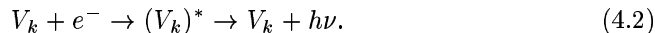
Another trapping centre is the so called “molecular ion”, X_2^- , formed when a hole is trapped by a pair of anions. In the process of thermalisation a hole reaches the top of the valence band and localises at an anion (X^-). The anion and the trapped hole form a covalent bond with the neighbouring anion, thus reaching a lower energy state. Somewhat confusingly, this defect configuration is often referred to as a V_k -centre, although it does not involve a cation vacancy. However, this will be the notation used in this thesis. The hole associated with the V_k -centre is referred to as being “self-trapped”, denoted as STH, and is relatively immobile compared to the holes in the valence band. If the hole associated with the V_k -centre is part of an exciton, it forms a self-trapped exciton (STE).

A more complicated centre, somewhat related to the V_k -centre is the so called *H*-centre. It consists of a neutral anion occupying an interstitial position between two neighbouring anions. A molecular-ion-like configuration as in the V_k -centre can form, but this is now located at a normal anion site interacting weakly with the two neighbouring anions (see figure 4.3).

4.1.2 Intrinsic Crystals

Since pure, perfect crystals do not have energy levels in the band gap, they should only be able to produce scintillation photons due to e-h recombination, in general not a very efficient process. However, lattice defects and traps can cause additional luminescence. In ionic crystals, two main types of the intrinsic luminescence are known, namely, *excitonic* and *core-to-valence* (CV) luminescence. The latter is also known as cross-luminescence.

The excitonic luminescence arises upon recombination of an electron of the conduction band with the self-trapped hole (STH) in a V_k -centre. If the V_k -centres captures an electron, either electron component of the exciton or a free electron, the excited $(V_k)^*$ molecule can emit a photon



Most of the holes in pure ionic crystals are rapidly changed into V_k -centres since the average time for STH formation is less than the life time for free holes (before they recombine with electrons in the conduction band). Thus, pure crystals can give an effective luminescence due to the formation of a large number of V_k -centres during irradiation of the crystal. The V_k -centres act as luminescence centres and vanish after emission of photons and the crystal regains its initial properties. There are a few intrinsic crystals that are luminescent, notably diamond, and some even have a fairly high light output. The excitonic luminescence of intrinsic alkali halides is only effective at low temperatures, when holes are self-trapped. However the alkaline-earth fluorides, e.g. CaF_2 and BaF_2 , show a high excitonic luminescence at room temperature. Some compounds with complex anions also show a high level of intrinsic luminescence, for example CdWO_4 .

CV luminescence is a result from transitions between the valence band and the core (filled) band which represents the inner shell electrons as shown in figure 4.5. After excitation of the inner shell electron, an electron in the valence band recombines with the core hole radiatively.

An advantage of the intrinsic crystals is that they have no problem with non-uniform impurity distribution as in the extrinsic. They also possess a higher radiation hardness than the doped crystals.

4.1.3 Extrinsic Crystals

The extrinsic crystal is doped with impurities, so called *activators*, in order to make the scintillation process more efficient. Some common activators are Tl, Eu or Ce. In general, the doped crystals give a higher light output than the pure crystals, and the luminescence is mostly due to the presence of activators, not from processes like in the case of a pure crystal. The activators introduce additional states in the band gap (see figure 4.4) corresponding to the ground and excited state of the activator. It is the transitions between the excited and the ground state of the activator that gives rise to the extrinsic luminescence. There are different ways

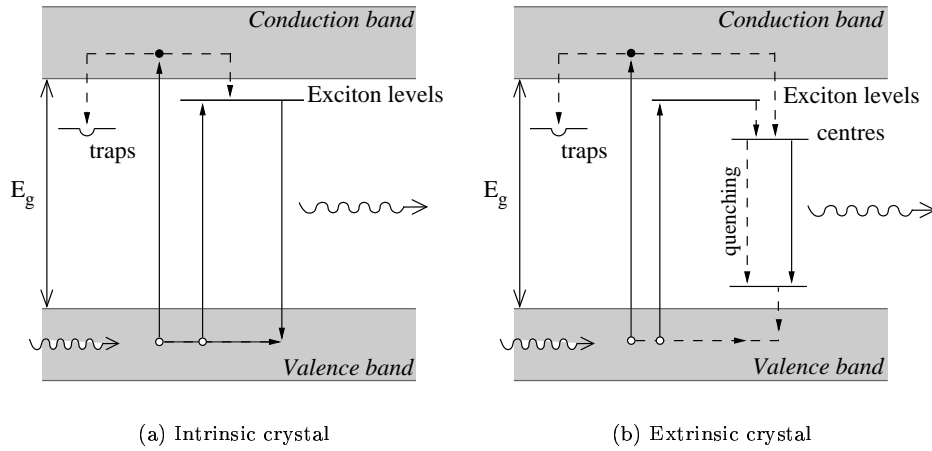
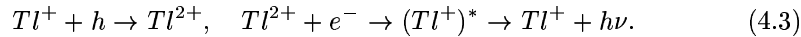
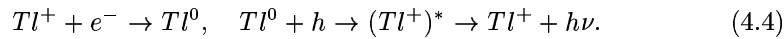


Figure 4.4. The energy band structure of the (a) intrinsic and (b) extrinsic crystal.

in which the activators can reach an excited state. The excitation energy can be transferred directly through particles or radiation, a scenario more common in crystals with large concentrations of activator. Another, more plausible, possibility is when an electron in the Tl^+ activator ground state is captured by a positive hole in the valence band, leaving the activator as a positive Tl^{2+} ion. The Tl^{2+} ion can subsequently capture an electron drifting in the conduction band resulting in an excited Tl^+



In the same way a Tl^+ may capture an electron forming a Tl^0 centre, which upon recombination with a hole emits a photon



In both cases the result is an excited activator atom which de-excites by emitting a photon.

One important consequence of luminescence through activator sites is the fact that the crystal is transparent to its own scintillation light. In the pure crystal, roughly the same energy would be required to excite an e-h pair as that liberated when that pair recombines. As a result, the emission and absorption spectra will overlap and there will be self-absorption in the crystal. In organic scintillators, the overlap between absorption and emission spectra is complete, and a wavelength shifting substance has to be added to the scintillator in order to avoid complete self-absorption of the scintillation light. In doped crystals, however, the transition

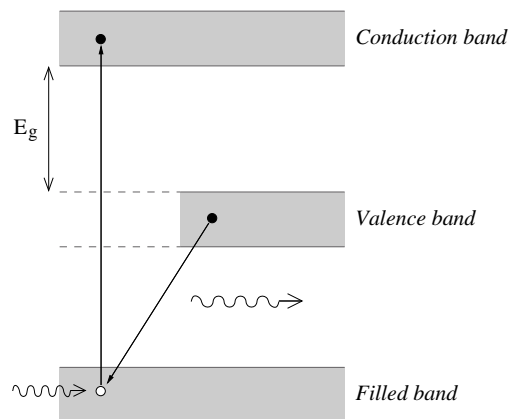


Figure 4.5. Core-to-valence luminescence.

energy from the excited activator to the activator ground state is usually smaller than the required excitation energy and there is no overlap. The shift of emission energy towards longer wavelengths compared to the excitation wavelength is called *Stokes shift* and plays an important role in optical qualities of a scintillator.

4.2 Properties of inorganic scintillators

Scintillators are currently being used in a great number of applications, from medical imaging devices, to accelerator- and space research. Despite the multitude of applications, there are some fundamental properties that constitute a good scintillator. An “ideal” scintillating crystal should have the following qualities:

- High conversion efficiency and high light output
- A short decay time (duration of scintillation light pulse)
- Radiation hardness
- Transparency to its own emission
- Low level of afterglow
- Temperature stability
- Proportionality of response
- Emission wavelength range should match that of the photosensor
- Chemical stability (low hygroscopicity)

- Good mechanical properties (hardness, ruggedness)
- Distribution of activator impurities should be homogeneous
- Low manufacturing cost

It is difficult, if not impossible to find a scintillator that exhibits all these qualities mentioned above, and a compromise is often necessary when choosing a material suitable for a certain experiment. In high-energy calorimeters, a high stopping power is required. This makes inorganic crystals suitable since they are usually made of elements with a high atomic number. They also have some of the highest light outputs of all scintillators, resulting in a better energy resolution.

4.2.1 Scintillation efficiency

One of the most important features of a scintillator is how well it converts the incident radiation to light. There are two parameters usually discussed when comparing scintillator light yield. First, there is the energy efficiency or the conversion efficiency, which is the fraction of the absorbed energy that is converted into scintillation light

$$\eta = \frac{\langle E_{ph} \rangle N_{ph}}{E_{abs}}, \quad (4.5)$$

where $\langle E_{ph} \rangle$ is the mean energy of scintillation photons, N_{ph} is the total number of scintillation photons created, and E_{abs} is the energy of the incident radiation absorbed by the scintillator. The second important parameter is the light yield, LY , which is the number of emitted photons per unit of absorbed energy

$$LY = \frac{N_{ph}}{E_{abs}}. \quad (4.6)$$

Assuming that every e-h pair produces one scintillation photon and using equation 4.1, the maximum light output of an ionic crystal scintillator can be approximated as

$$LY_{max} \approx \frac{0.5}{E_g} \quad (4.7)$$

This gives for CsI-based scintillators, where $E_g = 6.1$ eV, a maximum light yield of $LY_{max} \approx 80\,000$ photons/MeV, to be compared with experimental results shown in table 4.2. Determination of the absolute scintillation yield is difficult, since there are many processes that affect the number of scintillation photons, from creation until they are converted into an electrical signal. It requires an accounting of the size of the scintillator, its self-absorption, the reflective wrapping of scintillator, matching of the emission spectrum of the scintillator and the sensitivity spectrum of the photosensor, the quantum efficiency of the photosensor, the optical coupling between scintillator and photosensor, etc.

According to equation 4.7, a small band gap should give a large light output. This is true for intrinsic crystals at low temperatures, but at room temperature

Table 4.2. Properties of some common inorganic scintillators, and an example of a typical organic scintillator.

	Density (g/cm ³)	Refr. index	Decay time ^a (μs)	Abs. light yield ^a 10 ³ (photons/MeV)	Wavelength of max. emission ^a (nm)	Att. length at 511 keV (cm)
Alkali Halides						
CsI	4.51	1.80	0.002,0.02/multiple	2/varies	305/450	
CsI(Tl)	4.51	1.80	0.68, 3.34	65	540	2.29
CsI(Na)	4.51	1.84	0.46, 4.18	39	420	2.29
NaI(Tl)	3.67	1.85	0.23	38	415	2.91
LiI(Eu)	4.08	1.96	1.4	11	470	
Other Inorganics						
BGO (Bi ₄ Ge ₃ O ₁₂)	7.13	2.15	0.30	8.2	480	1.04
CdWO ₄	7.90	2.3	1.1, 14.5	15	470	1.11
CaF ₂ (Eu)	3.19	1.47	0.9	24	435	
CeF ₃	6.16	1.68	0.005, 0.027	4.4	310, 340	1.77
BaF ₂	4.89	1.56	0.0006/0.63	1.4/9.5	305/450	2.29
GSO (Gd ₂ SiO ₅)	6.71	1.85	0.056/0.4	9	440	1.41
YAP (YAlO ₃)	5.37	1.95	0.027	18	370	2.13
LSO (Lu ₂ (SiO ₄)O)	7.4	1.82	0.047	25	420	1.14
Typical Organic Plastic Scintillator						
NE102A	1.03	1.58	0.002	10	423	
References	[51]	[51]	[51]	[51, 53]	[51]	[52, 54]

^afast/slow components

this is not the case due to thermal quenching. However, crystals with very narrow band gaps have limited possibilities due to the fact that they usually are covalent crystals in which the energy required to create e-h pairs is higher than for the ionic crystals. The probability for self-absorption also increases with a narrow band gap.

4.2.2 Time characteristics

In general, scintillators are considered fast instruments in the sense that their response and recovery times are short. The organic scintillators have faster response time, usually around a few ns, than the inorganic which ranges around μs . One of the fastest inorganic scintillators is CsF with a decay time of only 5 ns.

The time characteristics of the scintillation light is governed by the lifetimes of the luminescence centres. The intensity of the emission, I (in photons/s), can be described by

$$I = I_0 e^{-\frac{t}{\tau}}, \quad (4.8)$$

where I_0 is the intensity at $t = 0$ and τ is the *decay constant*. The emission is in general more complex due to the different scintillation mechanisms and often consist of a fast and a slow decay component, τ_f and τ_s

$$I = I_1 e^{-\frac{t}{\tau_f}} + I_2 e^{-\frac{t}{\tau_s}}. \quad (4.9)$$

I_1 and I_2 are the intensity contributions from the decay modes 1 and 2, respectively. The emission of CsI(Tl) has a rise time determined by τ_R and two decay modes

$$I = I_1 \left(e^{-\frac{t}{\tau_1}} - e^{-\frac{t}{\tau_R}} \right) + I_2 e^{-\frac{t}{\tau_2}}, \quad (4.10)$$

where the decay constants are $\tau_R=19.6$ ns, $\tau_1=679$ ns and $\tau_2=3.34$ μs [52]. The decay times of some common scintillators are presented in table 4.2.

The intensity, spectral composition and decay time of the much more long-lived afterglow depend on the purity of raw material, crystal manufacturing conditions, heat treatment and doses of irradiation. The level of afterglow is measured in percentage to the total light yield, and can be as high as a few percent after 6 ms in most halide crystals. NaI(Tl), CsI(Tl) and CsI(Na) show a rather high level of afterglow, 0.3% to 5% after 6 ms. BGO, CsF and Cadmium Tungstate (CdWO_4) crystals are examples of low afterglow with levels down to parts per mille after 6 ms [52].

4.2.3 Light propagation and readout

An important issue when using scintillators is the collection of the light produced in the crystal. The quality of light collection affects the energy resolution of a scintillator: if less photons are collected, the energy resolution will get worse due to poor statistics. In other words, the measured light yield should be close to the absolute (physical) light yield determined by equation 4.6. When measuring the

scintillation light, a photosensor is placed against the scintillator surface, and the photons must travel through the crystal and through the crystal surface in order to be detected. Hence, there are two optical characteristics of a scintillator which are important when collecting the largest possible fraction of the light produced, namely transmission and index of refraction.

Light transmission

The optical transmission is a measure of how transparent a scintillator is to its own scintillation photons, and is defined as $T = I_t/I_i$, where I_i and I_t are intensities of incident and transmitted sample light, respectively. Light absorption in a scintillator is characterised by e^{-kx} with absorption coefficient k and the path of the light beam, x , but often it is more convenient to use the *attenuation length*

$$L_\lambda = \frac{1}{k} = \frac{x}{\ln\left(\frac{I_i}{I_t}\right)} = \frac{x}{\ln\left(\frac{1}{T}\right)}. \quad (4.11)$$

Since absorption lead to a reduced light output and hence a worse energy resolution, it is desirable to have a scintillator with a L_λ as long as possible. In small scintillators, light absorption is generally not a problem, but it becomes important when the light path length becomes comparable to L_λ . However, due to reflections of the light on the inside surfaces of the scintillator, the path x can significantly exceed the length of the crystal, and absorption can become a problem already at lengths smaller than L_λ .

The scintillation light can be absorbed in two ways in the crystal, by re-absorption and by background absorption. Re-absorption is when light is absorbed by the crystal itself, and depends on physical characteristics of the compound like band-gap width and properties of the activator. Background absorption is when light is absorbed by impurities and defects in the crystal.

Light uniformity

The concentration of impurities and point defects is dictated by the purity of the raw materials and the conditions during the crystal growth. Impurities can also be distributed nonuniformly throughout the crystal, causing a variation of the transmission along the length of the crystal. The absorption in the crystal can increase due to radiation damage, and this is further discussed in section 4.4.

The other important source of light loss is when light escape through the scintillator surfaces not facing the photosensor. When the light strikes a surface it will be either reflected or transmitted depending on if its angle of incidence θ is greater or less than a critical angle θ_c . The critical angle is given by

$$\theta_c = \arcsin\left(\frac{n_{out}}{n_{scint}}\right), \quad (4.12)$$

where n_{out} and n_{scint} are the refractive index of the surrounding medium and the scintillator, respectively. Since the scintillation light is emitted in all directions, only a fraction of the light is reflected and may hit the surface where light is collected. In order to minimise the losses from escaping light, the scintillator can be wrapped in or coated with reflective materials so that the transmitted light can be reflected back into the scintillator. Commonly used reflectors are metal sheets or foils, magnesium oxide powder, and white paper or teflon tape. One can also maximise the internal reflection, by surrounding the scintillator with a medium having an index of refraction which is small compared to that of the scintillator. This can be accomplished by leaving a layer of air between the reflector and the scintillator.

Readout

While it is important to minimise the light losses through the scintillator surfaces as discussed in the previous section, it is just as important to have as high transmission as possible at the surface facing the photosensor. According to equation 4.12, maximum transmission is obtained when the index of refraction of the photosensor is matched to that of the scintillator. Since air between the scintillator and photosensor results in large internal reflection, an optical coupling between the two is necessary. The coupling medium should be transparent to the scintillation photons and have an index of refraction close to that of the photosensor.

The most common light amplifier when measuring light from scintillators is the photomultiplier tube (PMT). The CsI(Tl) crystals of the GLAST calorimeter, however, are read out with $p-i-n$ junction photodiodes, or PIN diode. The PIN diode is a semiconductor and converts light into electrical charges much like the solar cell. It consists of a thin p -layer, a central intrinsic layer of pure silicon (the i -region) and a n -type contact (see figure 4.6). The p -layer is as thin as possible to allow transmission of the light to the active region where $e-h$ pairs are created due to ionisation. The PIN diode is reverse biased so that the entire i -layer is depleted of free electrons and holes. This reverse bias creates an electric field across the i -layer

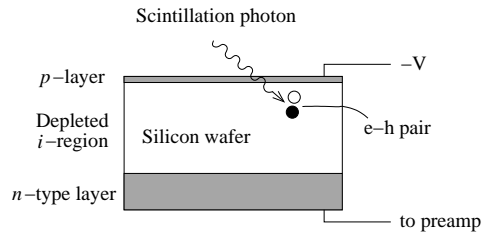


Figure 4.6. Schematic view of a PIN diode. Typical thickness of the p -layer and the depleted region (silicon wafer) is $<1 \mu\text{m}$ and between $200\text{-}500 \mu\text{m}$, respectively. Figure adapted from [51].

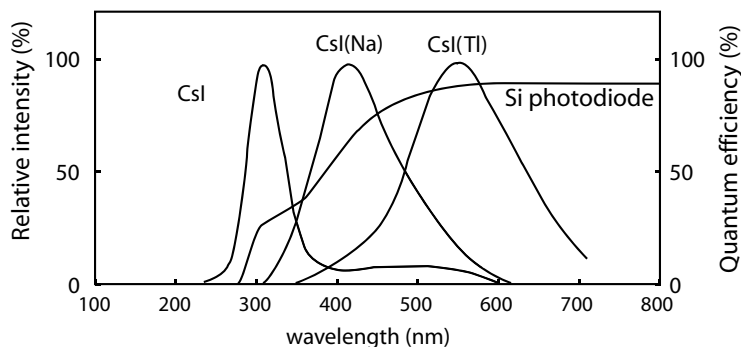


Figure 4.7. Emission spectrum of various CsI-based crystals, each spectrum is normalised separately (from Kubota et al. [55]), and quantum efficiency of a Hamamatsu S3590 PIN diode (from Hamamatsu [56]). The quantum efficiency of a typical PMT has a maximum around 400 nm and decreases fast at longer wavelengths.

so that the electrons are swept to the p -layer and the holes, to the n -layer. This flow of carriers in response to a pulse of radiation, gives rise to a electrical current that can be measured. The typical energy of a scintillation photon is about 3-4 eV, and the bandgap energy E_g in a PIN diode is of the order of 1-2 eV. Consequently the light photons have sufficient energy to create an e-h pair.

The PIN diode has no internal gain, they convert the optical photons from the scintillator to e-h pairs that are collected, and therefore the signal needs additional amplification. The construction of the PMT, on the other hand, allows a large amplification (of the order $10^5 - 10^7$) of the rather weak light output from the scintillator.

Still, the advantages of PIN diodes are many. For instance, the conversion of visible light to electrical carriers is not limited by the need for charge carriers to escape from a surface as in a conventional photocathode. Thus, the quantum efficiency of the process is much higher than in PMTs. The quantum efficiency also spans a much wider wavelength range than is typical for photocathodes in PMTs. As a consequence, a much higher primary charge is created by the light from the scintillator in photodiodes. The extended spectral response is particularly important for scintillators as CsI(Tl) with emission spectra that peaks at longer wavelengths and not in the UV, as is the case for most scintillators. This makes the CsI(Tl) scintillator ideal for PIN-diode readout since the PIN-diodes are sensitive in the red part of the spectrum. The overlap of the emission spectra of CsI(Tl) and the sensitivity range of the PIN diode is shown in figure 4.7. They also have a low power consumption, whereas the PMTs require high voltage. The fact that diodes are small is also an advantage on-board a satellite where the component space has to be minimised.

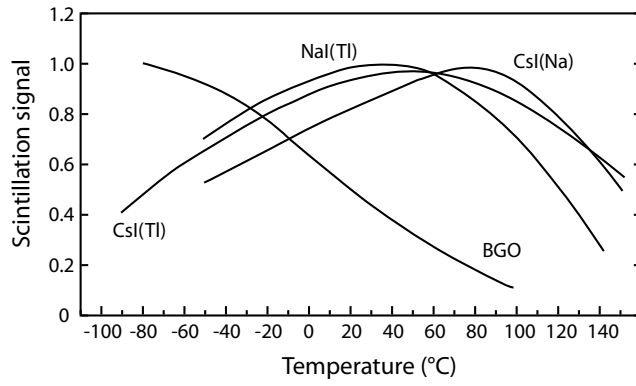


Figure 4.8. Temperature dependence of some inorganic scintillators.

4.2.4 Temperature dependence

The light yield of most scintillators is also a function of the temperature. This is caused by the fact that the probability for radiative transitions, which are responsible for the production of scintillation light, is temperature dependent. The radiative transitions dominate at low temperatures, but at higher temperatures, the nonradiative transitions become increasingly important and the luminescence is quenched (see section 4.1.1). The light output as a function of temperature for NaI(Tl), CsI(Tl), CsI(Na) and BGO is shown in figure 4.8, and should be compared to the expected temperature of -10°C for GLAST in orbit. When scintillators are used at room temperature where it is fairly easy to maintain a stable temperature, but this is more difficult for detectors used in space applications. The temperature dependence of the light yield has been measured for the GLAST CsI(Tl) crystals in the range -20°C to $+30^{\circ}\text{C}$, showing a light yield loss of the order of 8% at -10°C as compared to room temperature [44].

Since changes in temperature cause variations in light output, it causes an uncertainty in the energy measurement, and it is therefore necessary to calibrate the calorimeter in orbit.

4.2.5 Mechanical and chemical properties

The mechanical and chemical properties are important for the handling and maintenance of the scintillator. Mechanical hardness and ruggedness are important for detectors exposed to shocks and pressure, for instance in space applications where the detector must be able to handle the stress during launch. As the GLAST crystals are long and narrow, the material should not be too “soft” or brittle so that the crystal is easily deformed or breaks. Also, the scintillator should not easily split

along its crystal planes when being cut, an ability called cleavage. This is especially a problem when intricate shapes are required.

When the detector is exposed to temperature changes, the crystal can expand or contract. This property is governed by the crystal thermal expansion coefficients, which should be as small as possible. CsI has a rather large coefficient of thermal expansion (50 ppm/°C) and even moderate temperature variations lead to substantial dimensional fluctuations of the CsI(Tl) crystals. The temperature range is assumed to be between approximately -20°C to $+30^{\circ}\text{C}$, which implies a dimensional change of approximately 0.3% for a 50°C swing.

It is also desirable that the crystal is chemically stable, i.e. it does not react with its surrounding environment. A major disadvantage of inorganic scintillators is the fact that many of them are hygroscopic, that is chemically instable when exposed to moist air. One example is NaI, which liquefies unless it is contained in an air-tight casing. CsI(Tl) is slightly hygroscopic, but can in general be handled without protection from the open air.

4.3 Radiation environment of GLAST

GLAST will orbit the earth at an altitude of 600 km and at an 28.5° of inclination. At this altitude there are four main sources of background particles: galactic cosmic rays (GCR), trapped particles, solar energetic particles (SEP) and albedo particles. The trapped particles are confined in belts, caught by the magnetic field surrounding the Earth. The field lines looping from pole to pole, shield us from the charged particles in the solar wind. Some of the particles deflected by the magnetic field become trapped, spiralling around the magnetic field lines. At the magnetic poles where the field lines are tighter, the trapped particles bounce off and reverse their trajectory spiralling to the opposite pole where they are reflected again (figure 4.9). Moving from pole to pole they form the *van Allen radiation belts*. The inner belt extends over altitudes of about 2000 km–5000 km and contains a population of protons with energies 10 MeV–100 MeV. The outer belt is about 6000 kilometers thick centred at about 16000 km from the earth, and contains mainly ions and electrons with energies above 10 MeV. These bands of trapped radiation are well above the GLAST orbit. However, a part of the inner Van Allen belt dips down to about 200 km over the southern Atlantic Ocean off the coast of Brazil causing a region of increased particle flux called the *South Atlantic Anomaly* (SAA). This is due to an irregularity in the Earth's magnetic field, probably caused by a tilt in the magnetic axis of the Earth by approximately 11° from the spin axis, and an offset of the centre of the magnetic field from the geographical centre of the Earth by 45 km. The boundaries of the SAA vary with altitude above the Earth. At an altitude of 500 km, the SAA ranges between -90° and $+40^{\circ}$ longitude and -50° to 0° latitude (figure 4.10). The radically increased particle flux makes it impossible to separate interesting events from the huge background, and it can also cause radiation damage to instruments and electronics on-board. When instruments pass

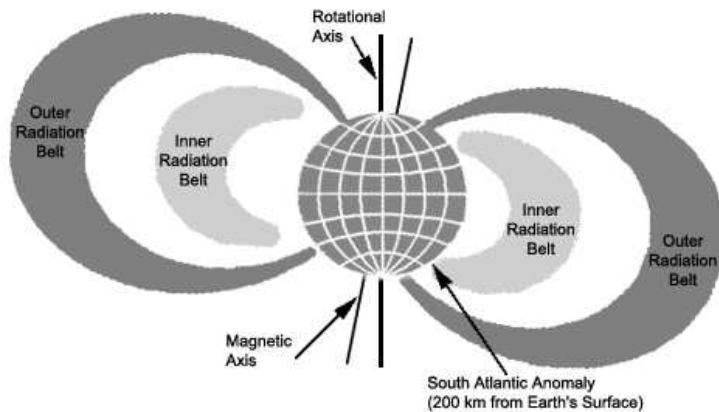


Figure 4.9. Charged particles spiralling around the Earth's magnetic field lines, forming the Van Allen belts. The inner belt extends over altitudes from about 2000 km to 5000 km and contains mainly of protons. The outer belt contains mainly low-energy electrons and is about 6000 km thick centred at about 16000 km from the earth.

through the SAA, the electronics are usually turned off due to the large amount of unwanted data, but also because radiation damage of electronics can be worse when powered.

It is the GCRs that are the dominant source of charged particles in the GLAST orbit outside the trapped-particle belts. The major contribution to the total dose, however, is the low-energy trapped protons and electrons from the SAA, where GLAST will spend about 10% of its orbit. These particles are important when considering radiation damage of the instruments. The expected particle flux for GLAST has been estimated using models of the radiation environment in near-Earth orbits, and data from earlier experiments. The spectra of cosmic-ray nuclei from space has been calculated using the CREME96 code [57]. The charged albedo particles near the Earth are secondary products created in collisions of cosmic-rays with the upper atmosphere. They are not included in CREME96, but the flux is known through measurements by, for instance, AMS (Alpha Magnetic Spectrometer) [58]. Cosmic-ray electrons are not included in CREME96 either, but are estimated from the data from the balloon-borne experiment HEAT [59]. The orbital average particle flux of cosmic-rays is estimated to be $\sim 200 \text{ m}^{-2}\text{sr}^{-1}\text{s}^{-1}$ with a peak value of $\sim 500 \text{ m}^{-2}\text{sr}^{-1}\text{s}^{-1}$, and the average flux from trapped particles in SAA is $\sim 10^6\text{--}10^7 \text{ m}^{-2}\text{sr}^{-1}\text{s}^{-1}$ [60].

GLAST is designed for a 5 year mission, i.e. all detector elements and electronics are required to withstand the radiation dose received during that period with a maintained performance. The estimated dose for a calorimeter CsI(Tl) crystal

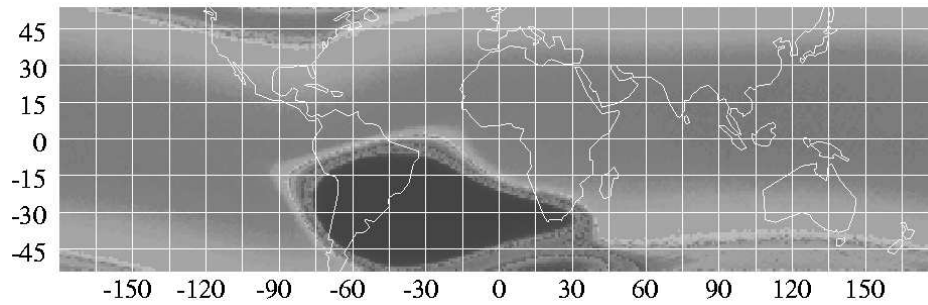


Figure 4.10. The South Atlantic Anomaly as seen by the ROSAT satellite at an altitude of ~ 560 km. The dark area represents high particle intensities. The y-axis show longitude and x-axis latitude (in degrees). Credit: S.L. Snowden, adapted from [62].

element during 5 years is 100 Gy. This dose is based on an estimation of the maximum dose deposited in a crystal element, which is expected to be around 20 Gy for a 5 year mission [61], multiplied with a safety factor. It is primarily the outer layers of crystals in the calorimeter that will receive such a dose, since the trapped charged particles are not energetic enough to penetrate to the inner parts of the calorimeter. However, protons can induce radioactive isotopes in the crystal material, and the activity of these crystals could cause background noise in the calorimeter deteriorating the energy resolution. Radiation damage induced by particles and radiation will be discussed in the following section.

4.4 Radiation damage of CsI(Tl) crystals

At high doses and dose rates irradiation by particles and photons can deteriorate the properties of a scintillator, and in some applications it is necessary to include radiation hardness as a parameter when choosing scintillator material. Note that radiation in the term radiation hardness here refers to both particles and photons. To understand how heavy or long-term irradiation will affect the performance of the GLAST calorimeter, the damage mechanisms in the CsI crystals must first be understood. There are a plethora of studies of radiation effects on scintillating crystals. However, radiation hardness is not a well-defined quality and usually the term radiation hardness is used as a measure for the maximum dose tolerated in actual detectors, i.e. the limit for the relative reduction of the light yield for a given detector configuration. Therefore most studies are of specific detector configurations and sizes, different particle species and doses.

4.4.1 Mechanism of radiation damage

Radiation damage can be defined as a process which alters the scintillator properties by introducing defects in the crystal. Defect formation is an alternative to the scintillation process, where the energy of the incident particle is converted into various lattice defects instead of scintillation light. Further, the defects acts as traps, preventing or delaying the scintillation process. The formation of defects is a complicated process which depends on many variables like dose rate, particle type, energy of the incident particles, and it involves not only the host material but also the impurities and defects in the crystal. The dose rate affects the degree of radiation damage when the production rate of defects and traps is higher than the liberation of trapped electrons and holes.

The most basic form of defect formation is by atomic displacement, where an atom is displaced from its equilibrium position in the lattice, followed by a return to its original place or a migration to some alternative point of stability in the lattice. If the lattice atom is “knocked-out” it may collide with other lattice atoms and produce a cascade of displacements. Each displaced atom will either meet a vacancy and recombine, or settle to an interstitial position in the lattice. A vacancy is usually mobile and can move through the lattice and can interact with impurity atoms or cluster with other vacancies.

The mechanism of radiation damage may be different between the photon (or electron/positron) induced damage and the hadron induced one. Photons interact through photoelectric effect, pair production and Compton scattering which cause a small recoil of the nuclei in the material. The photons cannot displace a lattice atom permanently due to their relatively small momentum, however they may generate secondary high-energy electrons which can produce larger displacements through collisions. The displacement caused by photons is usually small, and can be partly or mostly restored by adding energy to the lattice through e.g. thermal heating or UV irradiation. When hadrons (protons, neutrons etc.) pass through a scintillator, the atoms may be permanently displaced in the crystal, or fragment into light nucleons, resulting in static point defects in the lattice. In this case the radiation damage can not be restored by for instance thermal heating as in the case of photon- or electron-induced damage. Hadrons can also interact with the nuclei, causing radioactivation of the crystal. The rate of activation depends on incident particle type, its energy and the atomic number of the scintillator, the rate increasing with higher atomic number.

Defects can also be produced in other, more complicated ways and often involves various impurities in the crystal. Usually there is a number of defects already introduced in the crystal at the growing stage, in the form of impurities in the crystal raw material. The amount of impurities can be reduced by improving the growing technique and purification of the crystal melt. This can improve the radiation tolerance of the scintillator crystal. It should be noticed that the activators introduced in the crystal to enhance the light production can also increase the radiation

damage, since it is an impurity. The activator concentration has to be balanced against optimised light yield and radiation hardness.

In alkali halide crystals there exist another mechanism of defect production called *self-trapping*, a process described in section 4.1.1. It is a more efficient process in halides than the knock-out collision, and it often dominates the radiation damage in these crystals. The STH can capture an electron and form a STE, which can decay radiatively or nonradiatively. There are two channels for nonradiative decay: F - H pair production, and thermal quenching. During the nonradiative annihilation or dissociation of an STE, a pair of F and H centres are formed (see figure 4.3). The F-H pair is unstable and will recombine unless the H centre moves away from the F centre. If the H centre migrates far enough not to feel the attractive force from the lattice distortion of the F-centre, a stable F-H pair is created. The process of F-H defect formation competes with the scintillation process and is a source of energy loss in the crystal. The radiation hardness of alkali halides thus depends to a large extent on the production efficiency of the V_k centres, which produce distortions in the crystal lattice and improve the conditions of defect creation.

4.4.2 Effects of radiation damage

The defects and traps cause changes in both optical and scintillation properties of the scintillator. The radiation-induced defects and traps decrease the number of carriers available to transfer energy to the luminescence centres, resulting in a decrease of the scintillator light output. An additional effect is degradation of the optical transmission of the scintillator, due to the formation of colour centres (F -centres), which introduce absorption bands in the emission spectrum of the scintillator. Self-absorption is especially problematic in the large gamma-ray detectors for high energy physics, where large scintillators are required. A small decrease in optical transmission can become significant when accumulated over the length of the scintillator. Some radiation hardness studies refer to the attenuation length L_λ (equation 4.11) of a scintillator irradiated by various doses. As the transmission becomes worse, the attenuation length decreases.

Another effect of irradiation is worse uniformity of light output due to a non-uniform distribution of impurities or activators along the scintillator. A perfect uniformity ensures that all events depositing the same energy give rise to the same total scintillation light, regardless of where they occur in the scintillator. If defects are formed non-uniformly throughout the scintillator during irradiation, the light output is not linear with position and the position resolution gets worse. The uneven distribution of impurities is a result of the crystal growing process, and might not be noticeable before the scintillator has been exposed by radiation.

Irradiation can create shallow traps, states with energy level just below the conduction band. Trapped carriers cannot return to the ground state, but can be released thermally and return to the conduction band. In this way traps delay the scintillation light, creating a constant level of light output, afterglow. The induced afterglow increases the background noise in the detector. When exposed

to hadrons, the induced radioactivity can also cause background noise due to the radioactive decay products. The amount of induced activity depends on the rate of isotope creation in the crystals and half-life of the induced isotopes. If the isotopes decay slower than the production rate, radioactivity is built up and there will be a constant level of noise at energies of the gamma-rays from the decays.

It is difficult to rank scintillators after radiation hardness, since there are so many variables involved. Among the crystals most sensitive to radiation damage are the thallium activated crystals which show an effect already at 10 Gy, and at the other extreme, the most radiation hard crystal is GSO(Ce), which can take a dose up to 10^7 Gy without showing any significant effects of damage [63]. The inorganic crystals can be ranked in order of increasing radiation resistance: NaI(Tl), CsI(Tl), CsF, BGO, YAP, CeF₃, BaF₂ and GSO(Ce) [64].

The radiation hardness of CsI(Tl) has been studied quite extensively due to its widespread use in particle detectors. It shows a reduction in light output already after a dose of a few Gy of gamma irradiation, saturating above a few tens of Gy. However, there is often a variation from sample to sample, due to the level of impurities introduced at the growth process. It should be noted that measurements of light output from CsI(Tl) after irradiation is often problematic due to the high level of afterglow [65]. Usually the crystals have to “cool down” up to a few days before light output can be measured, so that afterglow does not interfere with the measurements. It was also observed that damaged crystals can recover, however, the recovery rate for CsI(Tl) is slow in room temperature.

It is believed that the main cause of light loss is predominantly due to increased self-absorption, not to decreased scintillation light yield [66, 67]. Studies of CsI(Tl) transmission show that the light absorption caused by irradiation is significant at short wavelengths. A group of six radiation-induced absorption bands in the 350-600 nm has been seen, and an additional band at 840 nm [67]. However, studies of radiation damage in CsI and CsI(Tl) by Woody et al. show that the degradation in light output after irradiation is greater than what would be expected simply from the loss in internal transmission [65].

The radiation hardness seem to be connected to the oxygen contamination in the CsI(Tl) [66], and the radiation tolerance can be improved using growing techniques eliminating oxygen impurities in the crystal melt. It is also verified that the radiation tolerance in CsI(Tl) depends on the thallium concentration, where a higher thallium concentration tends to make the crystal more susceptible to radiation damage [67].

To conclude, the large number of variables makes it difficult to predict the dose required for measurable damage in CsI(Tl) and therefore tests are a crucial part of determining the radiation tolerance of the GLAST crystals.

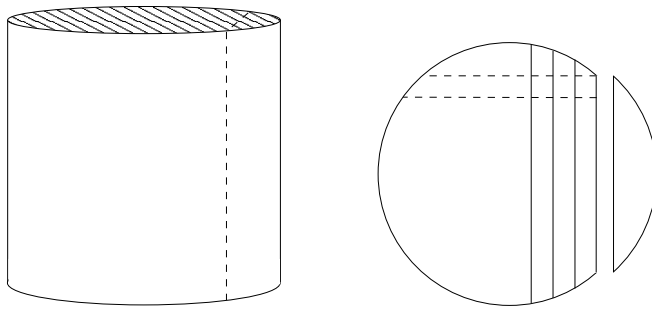


Figure 4.11. CsI(Tl) boule cutting procedure. Left: A slice of the boule is cut along its side. Right: The boule is seen from above, the dashed lines indicates how the crystal logs are cut.

4.5 Radiation hardness tests of CsI(Tl) crystals

The method used when producing the GLAST crystals is based on the so called Bridgman-Stockbarger method, a commonly used method when growing CsI(Tl) crystals (see e.g. [68]). This technique is relatively simple and uses a seed of CsI in a crucible, fed with a melt of CsI enriched with thallium. The result of the growing procedure is a so called *boule*, a cylindrical clump of CsI(Tl) crystal typically weighing about 400 kg with a diameter of 30 cm and a height of 40 cm, approximately. About 25 to 50 crystal logs can be cut from one boule. When a crystal boule is ready for machining, a slice is cut along the side of the boule with a band saw (see figure 4.11). Two sample crystals are cut from this slice, one from the top of the boule and one from the bottom. To test the radiation hardness of the crystals, the bottom sample of every boule is irradiated with gamma-rays. This is taken as a measurement of the radiation hardness of the boule. The boules are accepted if the boule sample exhibit less than 50% degradation in light output after 100 Gy of ^{60}Co gamma-rays. When a boule is approved, further slices are cut parallel to the first. Each slice is then cut into bars according to figure 4.11, the top end being marked out on every crystal log in order to keep track of the original crystal orientation in the boule. Every crystal is also given an ID number according to their original place in the boule. The crystals also undergo optical and mechanical quality tests [69] before they are accepted as flight crystals.

Three different types of radiation tests have been performed. The two first being irradiation of boule samples and “full-size” crystals, i.e. crystals with the same dimensions as flight crystals, with ^{60}Co gamma-rays. ^{60}Co decays in a cascade, giving two gamma-rays with energies 1.173 MeV and 1.333 MeV. The purpose of the second test was to obtain a correspondence between the radiation hardness of the boule sample and a full-size crystal. By using the result from this it is possible to get an estimate of the expected performance of the full-size crystals from that

boule. Finally, a full-size crystal was irradiated with 180 MeV protons. The purpose of this test was to measure the effect of protons, the main background for GLAST, and compare the results with those of gamma-ray irradiation.

4.5.1 Radiation hardness tests of boule samples

A total of 52 boule samples were irradiated at the ^{60}Co source at the Karolinska Hospital (KS) in Stockholm. It consists of a point source in a lead casing. Collimating lead blocks can be manually separated and define the size of the radiation field. The samples to be irradiated are placed onto a vertically adjustable table under the opening. The source is calibrated once a year by using ionchamber dosimetry, where the dose rate is measured in a water sample 80 cm from the source, and at 5 mm depth in the water where the dose is maximum (see for instance [70]). Since the concentration of thallium (and possibly other tracers) might differ between boules and in particular from top to bottom within individual boules, some variation in radiation tolerance can be expected. The thallium concentration at the bottom of the boule is equal or higher than that at the top, and therefore only the bottom samples were irradiated to give a lower limit of the radiation tolerance of respectively boules.

The dose rate in CsI is different from that in water, and can be calculated by considering the ratio of mass energy-absorption coefficients, μ_{en} , for water and CsI at 1.25 MeV, the average energy of a decay event of ^{60}Co . The gamma absorption coefficients (in cm^2/g) for CsI(Tl) and water at 1.25 MeV are 2.402×10^{-2} and 2.965×10^{-2} , respectively [71]. The result is that the dose rate in a CsI(Tl) crystal sample is 81% of that in water. Using this, and the fact that the dose rate is inversely proportional to the distance between source and crystal, one can adjust the height of the table to obtain a required dose rate in the CsI(Tl) crystal. The dose rate for the boule sample tests was 20 Gy/h, and was chosen as a compromise between the much lower mean dose rate in the GLAST orbit and the time for the duration of the tests.

Test set-up and procedure

Each sample crystal had both end surfaces highly polished, all other surfaces are rugged. A PIN diode (Hamamatsu 3590-05) was attached on the polished surface (figure 4.12), using a wax-like meltmount substance (Cargille) having a refraction index of 1.704. The meltmount had to be heated to 70 °C to become enough viscous for application. It was left on the epoxy surface of the diode for about 2-3 minutes in the oven. By then it had spread over the entire surface and it could be pressed onto the crystal. Once the wax cools and hardens, the PIN diode can only be removed by reheating the crystal and the diode. The sample crystal with its PIN diode was wrapped in white Tyvek and light tight black Tedlar. The light yield of the crystal sample was measured by using a 73 kBq ^{22}Na source, with gamma-energies of 0.511 MeV and 1.275 MeV. The source was placed directly in front of the

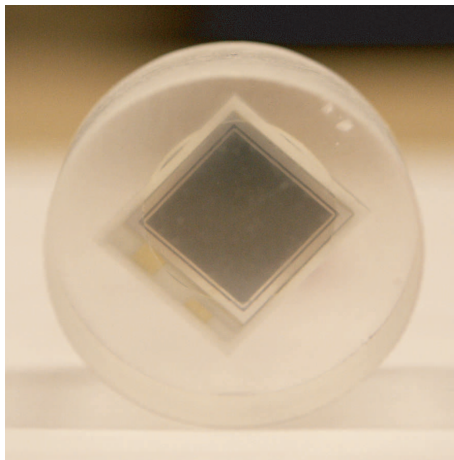


Figure 4.12. A PIN diode ($0.9 \times 0.9 \text{ cm}^2$ active area) seen through the bottom surface of a boule sample (2.5 cm diameter).

crystal, against the crystal surface being opposite to the PIN diode. A preamplifier (5093 eV Products) was mounted close to the PIN diode. Since it was necessary to shield the preamplifier to reduce noise pickup from external fields, the ^{22}Na source, crystal and preamplifier were housed in a metal box. An overview of the test set-up is shown in figure 4.13. The signals from the preamplifier were fed to a NIM linear amplifier (Tennelec TC205A), and were further collected by a multichannel analyser (Amptek MCA-8000) having 4096 channels. Data was collected during 200 seconds, and the spectrum was recorded with a laptop computer. The 0.511 MeV annihilation peak was fitted with a Gaussian and an exponential plus a constant background, as shown in figure 4.14. The centroid of the Gaussian was used as a measure of the light output from the crystal.

Before the irradiation of a crystal started, a reference spectrum was taken with the ^{22}Na source. The crystal, with its diode mounted, was after the initial light yield measurement disconnected from the electronics set-up and placed in the radiation field of the ^{60}Co source. After an irradiation period, the crystal was removed from the radiation field, the crystal was left to "cool down" for one hour to remove any effects from afterglow. The crystal was subsequently connected to the data taking system again, and the crystal response to the ^{22}Na source was measured, as prior to irradiation. The dose intervals were 20, 50, 100 and 200 Gy accumulated dose. To ensure an uniform irradiation, the boule sample was rotated 90° each irradiation period. The effect of afterglow was monitored for one of the sample crystals by measuring the light output with the ^{22}Na source every 20 minutes after irradiation during one hour. Temperature and humidity was monitored throughout the test.

Since the PIN diodes are attached to the boule samples during irradiation, two

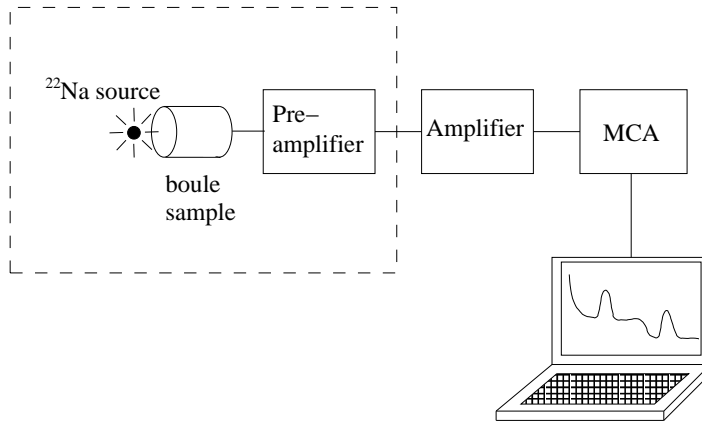


Figure 4.13. Test set-up electronics and data taking system for the light yield measurement of the boule samples. The ^{22}Na source, crystal and preamplifier were housed in a metal box (dashed line).

PIN diodes of the same kind as used in the boule sample tests were irradiated with photons from a ^{60}Co source with a dose of 150 Gy. One of the diodes had a reverse bias of 45 V during the irradiation. The leakage current of the diodes as a function of applied voltage was then measured in room temperature in the voltage range 0 to 100 V.

4.5.2 Gamma irradiation of full-size crystals

The full-size CsI(Tl) crystal log, measuring $326.0 \times 26.7 \times 19.9 \text{ mm}^3$, was also irradiated at the ^{60}Co radiation facility at KS. The dose rate was 20 Gy/h in the crystal, the same as for the boule sample tests.

Test-setup and procedure

Scintillation light was read out at each end by PMTs (Hamamatsu R669) via a 2 mm air gap, as shown in figure 4.15. The crystal log had all surfaces polished and was wrapped in VM2000 (3M), a highly reflective multi-layer polymeric film, with the ends facing the PMTs left naked. VM2000 gives up to 30% larger light output than Tyvek [44]. The reason for using air gaps was that it assured better reproducibility as compared to an optical connector, in this context it was considered being an advantage as compared to the relatively small additional loss of light. Crystal performance before and after irradiation was monitored with the 0.846 MeV gamma-ray peak from a 7.4 MBq ^{56}Co source, collimated to a 2 mm slice beam. The reason for the change of reference source was that it has a higher energy gamma-line, easier to resolve against the induced background, as compared

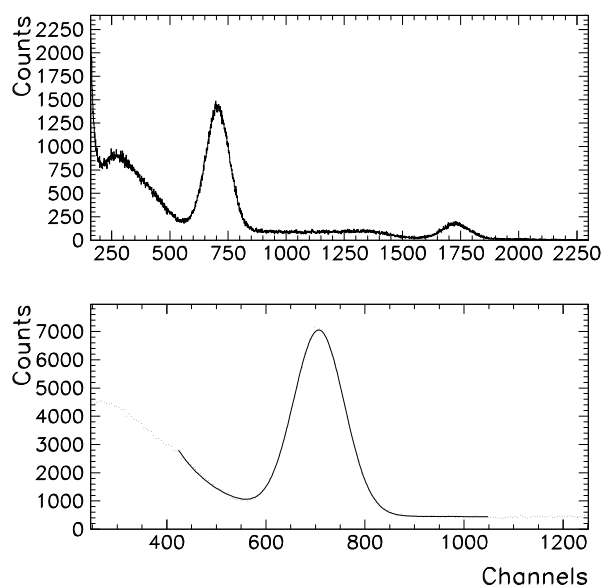


Figure 4.14. A typical ^{22}Na spectrum measured with a CsI(Tl) boule sample (upper figure), and the 0.511 MeV peak fitted with a Gaussian, an exponential and a constant (lower figure). Only a part of the spectrum is shown, the total number of channels is 4096.

to ^{22}Na . When measuring the light yield, the crystal, PMTs and the ^{56}Co reference source were contained in an optically closed box. The collimator and source can be mechanically moved, enabling the light yield to be measured stepwise at specified positions along the crystal. The absolute accuracy in position relative to the left end of the crystal is about 2 mm. The signals from the PMTs are amplified using a NIM dual amplifier (ORTEC EG&G 855) and fed to two ADCs (Canberra 8701). The collected spectra of the light output from the crystal ends are monitored by a PC. When the crystal was to be irradiated, it was removed from the test box and put in the radiation field of the ^{60}Co source. The field size at the location of the crystal was set to its maximum (about $45 \times 45 \text{ cm}^2$). The radiation field decreases in strength towards the edges of the field and only about 80% of the field is homogenous. Therefore, the crystal log was placed on the diagonal in order to get as a uniform radiation field as possible along the crystal.

Before irradiation, a reference measurement of the light output from the crystals was made by placing the ^{56}Co source along 7 different longitudinal positions of the crystals, at 20, 56, 92, 163, 234, 270 and 306 mm from the left end. The light output from both ends was measured for each position of the ^{56}Co source.

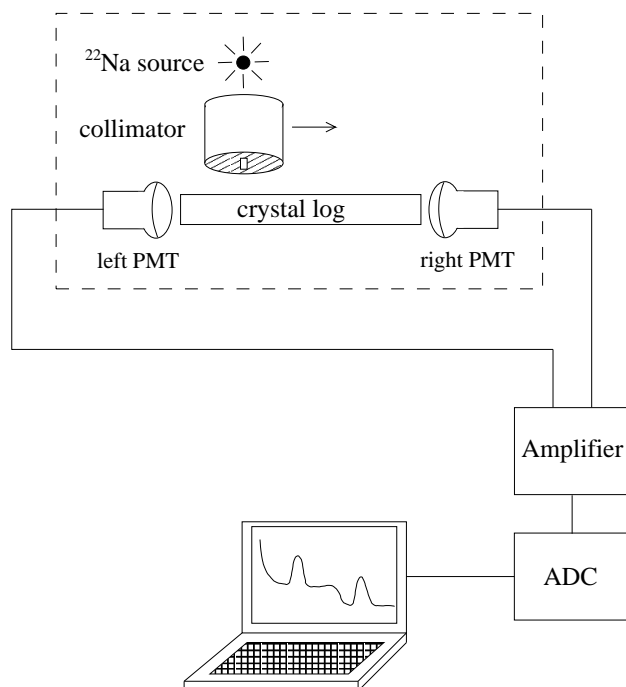


Figure 4.15. Test set-up for the radiation hardness test of a crystal log. The PMTs and the crystal were contained in a lighttight box (dashed line).

The crystals were rotated 180° after each irradiation step, so that deposited gamma energy would be as uniformly distributed as possible throughout the crystal volume. The irradiation was done in steps so that the accumulated dose became 20, 50, 150, and 180 Gy, respectively (200 Gy was the goal but beam time ended before it was reached).

The crystal performance was measured after each irradiation period with the ^{56}Co source as described above after a few hours of cool-down. However, after 6 hours, light pile-up due to afterglow was still substantial. In fact, a clear green-blue light could be seen with the naked eye and figure 4.16 shows how the crystal log glows from its ends after one of the irradiation periods. In order not to lose too much of allocated beam time the crystal performance was measured anyway. The decay of afterglow was measured after the last irradiation period in order to determine the afterglow decay as a function of time. In this way the previous measurements could be corrected for the afterglow.

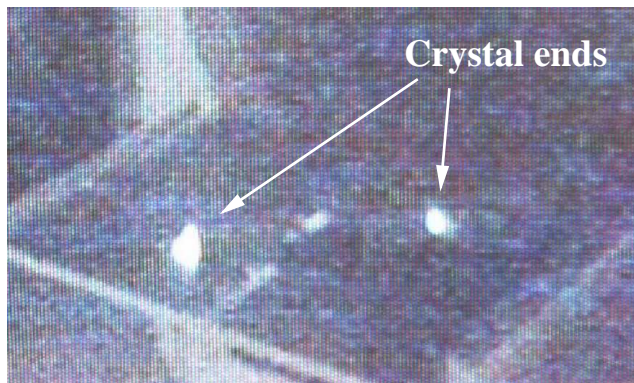


Figure 4.16. Photo of irradiated CsI crystal log “glowing” from both ends in the dark.

4.5.3 Proton irradiation of full-size crystals

A crystal log with same dimensions as in the previous gamma irradiation test was irradiated at the TSL (The Svedberg Laboratory) cyclotron at Uppsala University, which delivered a proton beam with 180 MeV energy. Both the change in light yield and the induced radioactivity in the crystal was measured.

The calibration of the telescope counting rate versus beam intensity at the crystal location was performed before irradiation, giving a dose rate of 7.4 Gy/h in the CsI(Tl) crystal.

Test set-up and procedure

During irradiation, the CsI(Tl) crystal log was placed 13 m downstream from the beam pipe window as shown in figure 4.17. The protons were scattered in an aluminum foil at the window, resulting in a wide beam profile at the location of the crystal. Before irradiation, the beam profile was mapped out and is shown in figure 4.18. Since the proton intensity drops radically from 10 cm and outwards from the beam centre, the crystal log was placed at an angle of 45° to the beam axis in order to obtain as uniform illumination as possible. The variation in beam intensity along the length of the crystal was 20% from the middle of the crystals to its ends, and the average value was 93.8% of the peak value of the beam. The 26.7 mm side was put transverse to the beam direction so that the protons had to penetrate the shortest distance. The photodiodes were attached during proton irradiation and were therefore shielded by 10 cm lead blocks, placed in front of each crystal end.

The beam intensity was continuously monitored by a beam telescope put at 30° scattering angle from the aluminum window. Protons deposited 41 MeV in the crystal with a variation of 18% less at the front surface than at the rear surface

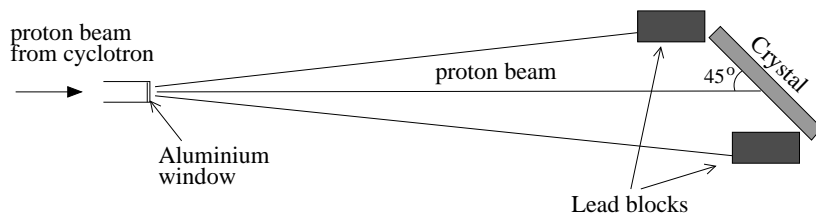


Figure 4.17. Schematic figure of the proton beam test set-up.

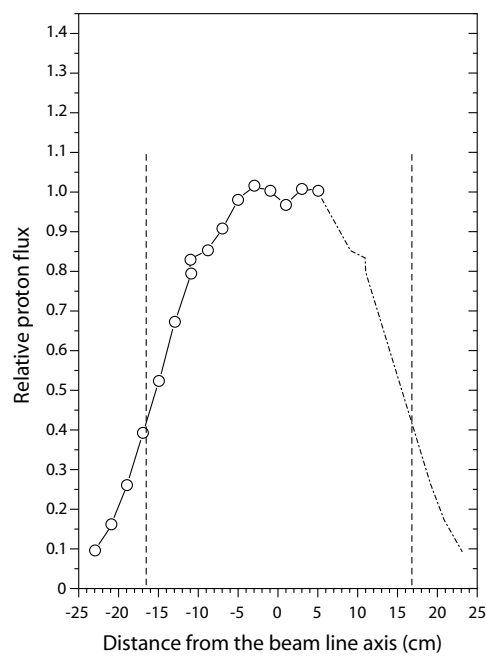


Figure 4.18. Proton intensity measured at the location of the crystal. The open circles represents measurements of the relative proton flux at different positions orthogonal to the beam axis. The dashed-dotted line show deduced "mirror points", and the dashed lines show expected geometric boundaries of the beam.

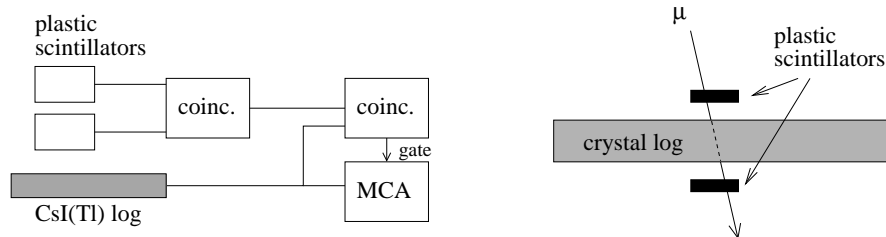


Figure 4.19. Overview of light yield measurement set-up. To the left is a schematic figure of the electronic set-up with its threefold coincidence. The right figure shows the position of the plastic scintillators.

because of the increase of energy loss dE/dx with decreasing proton energy. The crystal was rotated 180° between irradiation periods to get a more uniform energy deposition throughout the penetration depth. The dose was given in steps of 20, 70 and 175 Gy accumulated dose.

The CsI(Tl) signal was read out with photodiodes attached to each end of the crystal, using silicon grease (Viscasil) as an optical connector. The crystal was wrapped in reflective VM2000, and the crystal with photodiodes were then wrapped in several layers of lighttight Tedlar. The photodiodes were connected to preamplifiers (5093 eV Products) and the signal was further amplified using NIM linear amplifiers (Canberra 2026).

The degradation in light output from the crystal after irradiation was measured with cosmic muons. The cosmic muons have energy loss dE/dx close to minimum and therefore deposit on average 5.6 MeV/cm per particle in the crystal [15]. A penetrating muon was identified by a telescope made of two plastic scintillators placed above and below the crystal at its middle (see figure 4.19), covering a 2 cm wide area across the crystal. A simultaneous signal from both plastic scintillators and from the CsI(Tl) crystal triggered the readout of the scintillation light from the crystal. The centroid of the fitted muon peak was taken as a measure of the light output from the crystal. The set-up had been calibrated by taking a muon spectrum before the crystal was exposed to any protons.

Radiation induced activity

In order to identify the dominant radioactive isotopes, the gamma spectrum from the crystal was measured with a Ge(Li) detector. The crystal and the Ge(Li) detector was placed inside a lead cave, shielding it from external gamma radiation sources. As a background reference, the crystal was measured with the Ge(Li) detector prior to irradiation. The first Ge(Li) measurement of the activated crystal was taken 2.5 hours after the last irradiation period and again 3.5 and 6 hours

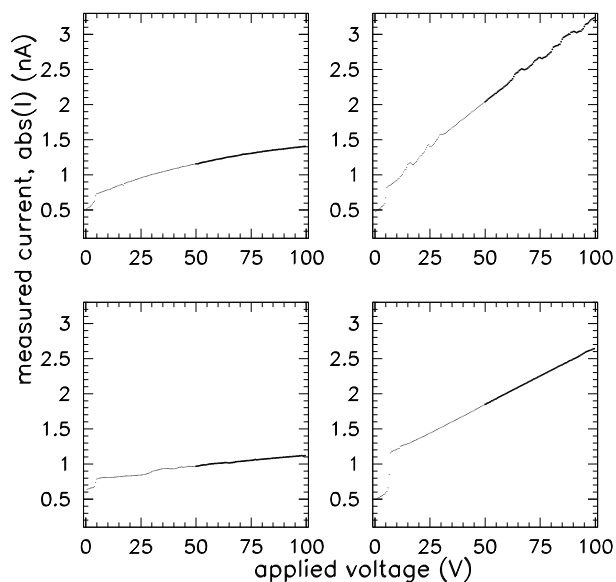


Figure 4.20. Leakage current before and after 150 Gy irradiation of PIN diodes. The upper figures show the reverse biased diode before (left) and after (right) irradiation. The lower figures show the diode without bias before (left) and after (right) irradiation.

after irradiation. The measurement was repeated after 5, 14 and 40 days after the irradiation stopped in order to observe the decay of some of the gamma lines.

4.5.4 Results of boule sample tests

The irradiation of the PIN diodes showed a small increase of leakage current (figure 4.20), however it is of the order of a few nA and within the manufacturers specifications. Thus, it should not affect the measurement of light yield from the crystals after irradiation.

As an effect of afterglow the crystals became more noisy after irradiation, with an increased background and wider gamma-lines as a result. Figure 4.21 shows the monitoring of the response of a boule sample to the 0.511 MeV gamma-rays, directly after ^{60}Co irradiation. The 0.511 MeV peak becomes much wider after irradiation, and gradually narrows down until it stabilises after approximately one hour. Its full width at half maximum (FWHM) is about 24% broader one hour after 182 Gy irradiation compared to the non-irradiated crystal. About one hour after irradiation, the light yield has stabilised.

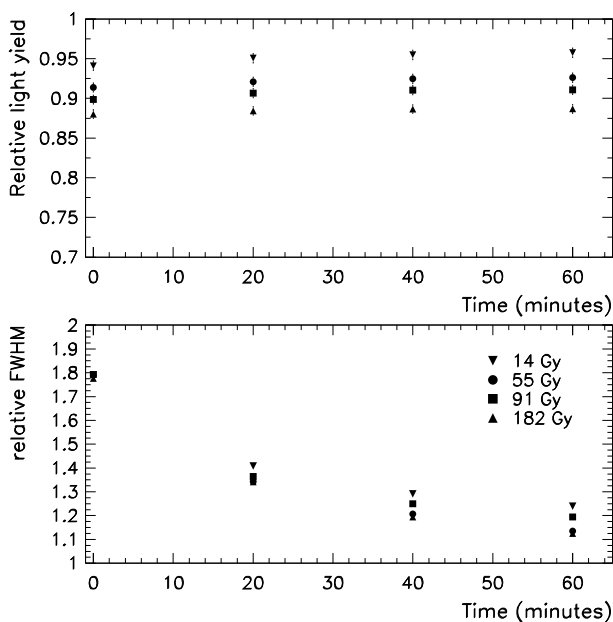


Figure 4.21. Measured light yield (top) and the relative FWHM (bottom) during 1 hour after irradiation.

Figure 4.22 shows how the relative light yield of a typical boule sample decrease with dose. All crystals showed a fast decrease in light output to about 95% for a 10 Gy dose. This fast decrease is followed by a slower decrease, reaching 88-90% for 90 Gy.

Figure 4.23 shows the distribution of the degradation in light yield at 100 Gy for the boule samples. The observed decrease in light performance is expected [67, 66] and is well within the limits specified for the GLAST CsI(Tl) crystals. The decrease in light output is less than 27% for all crystal samples after a dose of 100 Gy, and the variation between different boules is less than 20%. Average degradation at 100 Gy is 13.4%, and 15.6% at 200 Gy.

For the boule sample tests, statistical uncertainty from the fit is small, and the dominant error in peak position is systematic and comes from limited reproducibility of light output measurement. The stability of the test set-up was tested by measuring the light output from a crystal after disconnecting and reconnecting the crystal from the test set-up. The reproducibility of the ^{22}Na spectrum during the time of a radiation hardness test was found to be 0.7%.

The ionchamber calibration of the ^{60}Co source is accurate to 0.1%. The main

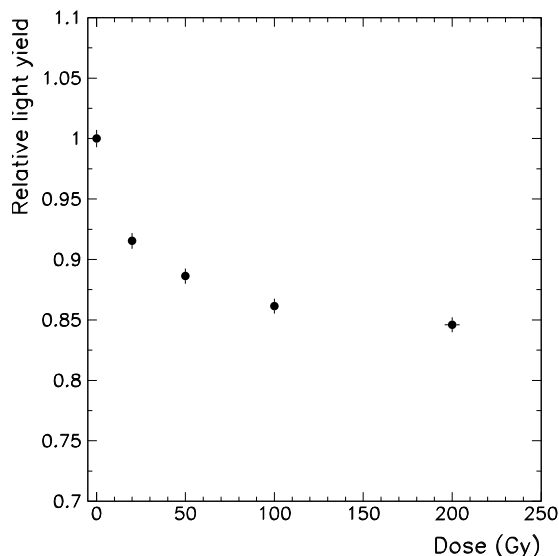


Figure 4.22. Relative light yield of a typical boule sample.

contribution to the dose error is due to the uncertainty of the distance from the ^{60}Co source to the crystal, which cannot be determined more accurate than ± 0.25 cm. This gives a relative error in dose of the order of 1%. The error in exposure time is negligible, since the uncertainty is of the order of 1 second, and the exposure time ranges from 30 minutes to 5 hours.

4.5.5 Results of gamma irradiation of full-size crystals

After 6 hours of cool-down after irradiation, the afterglow from the crystal log still gives a 20-30% larger pulse when measuring the response to the 0.846 MeV gamma line from ^{56}Co . After 16 hours some afterglow was still present. After 70 hours, though, the asymptotic value had clearly been reached. The decrease in light output from the crystal measured after 20, 50, 150 and 180 Gy accumulated dose, is presented in table 4.3. The light output measured after 20, 50 and 150 MeV has been corrected for afterglow. No significant difference could be seen between left and right PMT with the source located at the middle of the crystal. The errors in the first (0 Gy) and last (180 Gy) rows of table 4.3 are estimated to be less than 0.05 times the listed percentage. This uncertainty comes mainly from the limited reproducibility of light yield measurement due to the air gaps between crystal and PMTs. In the three middle rows the errors are larger due to the correction of

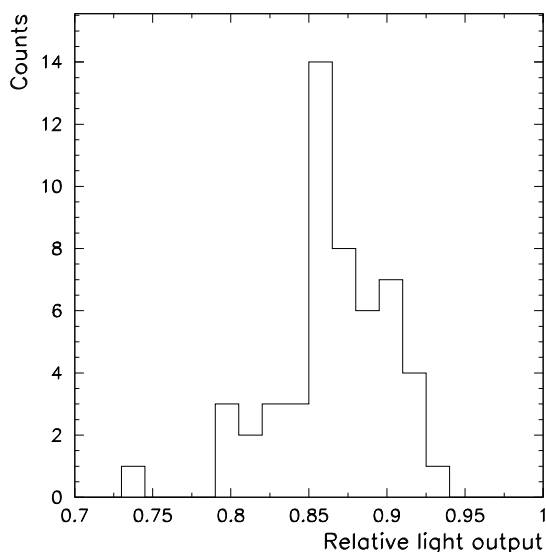


Figure 4.23. Degradation in light output at 100 Gy for the CsI(Tl) boule sample crystals tested at KS.

afterglow. The last row's numbers are the directly measured asymptotic values after 70 hours of cool-down, which remained stable up to more than 140 hours after irradiation had stopped. After 180 Gy, the average light output from the crystal had decreased by $(24 \pm 4)\%$. Average light output is here average of left and right PMT signals and averaged over source positions along the crystal.

There is a significant difference in the decrease between the close and the far PMT. For a 180 Gy dose, the close PMT shows a decrease of $(18 \pm 4)\%$, whereas the far PMT shows a $(30 \pm 4)\%$ decrease. This is interpreted as being due to two different components contributing to the damage. When the source is placed far from the PMT, and the light has to travel throughout the crystal, the decrease in light output is significantly larger than when the source is placed close to the PMT. This effect was similar for both left and right PMT. Thus, the conclusion is that both light production as well as light attenuation in the crystal material becomes worse after irradiation.

The result of the gamma irradiation of the crystal log can be compared with the results of boule sample tests, by considering the light yield when the reference source is close to the PMT. In this position the scintillation light travels roughly the same distance to the photosensor as for the boule sample. The average decrease in light output of 15.6% for the boule samples after 200 Gy agrees well with the

Table 4.3. Relative light output from the crystal log in response to a gamma line from ^{56}Co . The second column shows the average of left and right PMT with the source positioned close to the PMT, the third column with the source positioned at the far end of the crystal. The forth column shows the average of columns two and three.

Dose (Gy)	Close PMT (%)	Far PMT (%)	Average (%)
0	0	0	0
20	1	18	10
50	14	29	22
150	18	34	26
180	18	30	24

number $(18 \pm 4)\%$ after 180 Gy found in the present test when the source was placed close to the PMT. No significant difference could be seen between left and right PMT with the source at the same relative position.

4.5.6 Results of proton irradiation test

Before the crystal was irradiated with protons, gamma activity was measured with the Ge(Li) detector during approximately 4 hours. The gamma lines were few and are presented in table 4.4. The total intensity of the background was found to be approximately 2 counts/s, mainly coming from β^+ annihilation giving a line at 511 keV, and ^{40}K . It is possible that the lines at 583 keV and 2614 keV are due to ^{208}Tl .

There was substantial noise from the crystal, already after the first irradiation step. This could be seen by collecting the signals from the crystal without an external reference source. Figure 4.24 shows a spectrum collected 2.5 hours after

Table 4.4. Gamma lines in the background spectrum measured with the Ge(Li) detector of non-irradiated CsI(Tl) crystal. The gamma activity from the crystal was measured during approximately 4 hours.

Energy (keV)	Counts/s	Possible isotope
511	1.20	β^+ annihilation ^{40}K
1461	0.31	
596	0.13	
609	0.10	
2223	0.06	^{208}Tl ^{208}Tl
2614	0.06	
583	0.05	
3536	0.02	

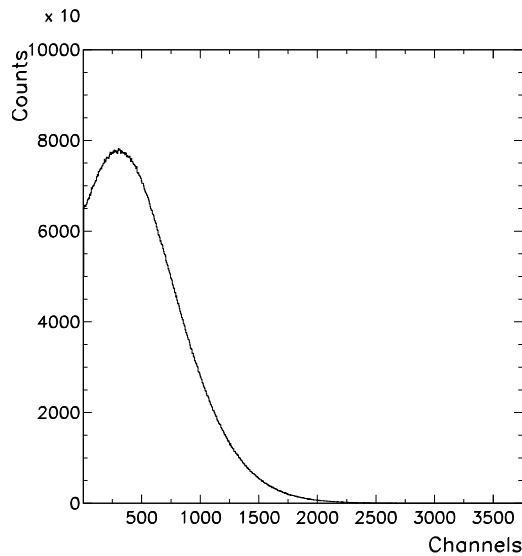


Figure 4.24. Spectrum measured without reference source or coincidence requirement 2.5 hours after a dose of 70 Gy from the proton irradiated crystal. Data was collected during 300 seconds. For comparison, a 0.511 MeV peak would be located around channel 100, and a muon depositing 11.2 MeV in the crystal at channel 2250. Only a part of the spectrum is shown, the total number of channels is 4096.

a dose of 70 Gy, by measuring the light yield without coincidence or any reference source during 300 seconds.

In addition to the large background, the count rate of the cosmic muons was low and it was not possible to measure the light output from the crystal in the short time available between the irradiation periods. Therefore, a muon spectrum could only be taken after the last irradiation step, and not in between irradiation periods. Only after waiting approximately 24 hours after irradiation a signal from cosmic muons could be seen. Muon spectra before and after irradiation are shown in figure 4.25. The average of the signals from the left and right end was taken as a measurement of the light output. An average of the light yield measurements during the first 7 days shows that after 175 Gy of proton radiation the light output has decreased with $(22 \pm 5)\%$, where the error given is the maximum deviation from the average.

The first gamma spectrum of the irradiated crystal measured with the Ge(Li) detector consisted of some 40 gamma lines (see figure 4.26). In order to identify the isotopes, it is necessary to consider all possible reactions between the crystal atoms ^{133}Cs and ^{127}I , and the incident protons. Nuclear reactions with thallium has been neglected due to its low abundance ($<0.1\%$) in the crystal. If the induced isotope

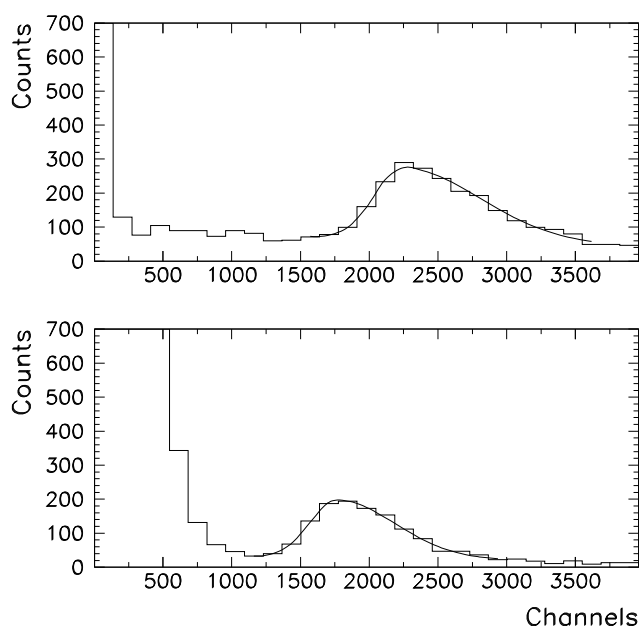


Figure 4.25. Muon spectra taken before irradiation and 34 hours after irradiation. The peak corresponds to an energy of 11.2 MeV, which is the average energy deposition of the muons in the crystal. The increased background after irradiation is clearly seen in the lower figure. Acquisition time was 11.7 hours for upper and 21.7 hours for lower spectrum, respectively.

is unstable, it will continue to decay until it reaches a stable nucleus. The energies of the possible decay modes giving rise to gamma-rays can then be compared with the measured gamma lines. Since the energy of the protons in the crystal depends on the distance from the front surface, different nuclear reactions will take place at different depths. This results in a variety of reactions and thus in a large number of gamma lines in the Ge(Li) spectrum. The possible reactions considered were: (p, xn) , (p, pxn) and $(p, \alpha xn)$, where the number of neutrons, x , depends on the proton energy. As an example, the reaction $^{127}\text{I}(p, n)^{127}\text{Xe}$ will give rise to gamma emission at energies 203, 375 and 172 keV when ^{127}Xe decays to ^{127}I which is stable. Since the half-life of ^{127}Xe is 36 days, emission should not be noticeable until days after the creation of the isotope. Looking at the Ge spectra, all three lines emerge after 5 days, their activity increasing after an additional 9 days. In the same way it is possible to identify the isotope ^{125}Xe , created in the reaction $^{127}\text{I}(p, 3n)^{125}\text{Xe}$. It decays to ^{125}I , giving gamma emission at the energies 188 and 243 keV. It has a rather short half-life of 17 hours and should therefore only be visible during the

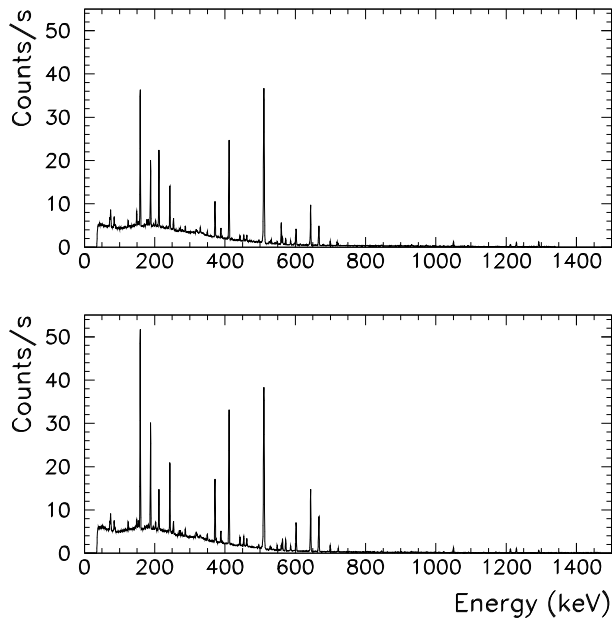


Figure 4.26. Gamma spectrum of the activated crystal measured with a Ge(Li) detector 2.5 hours after irradiation (upper figure) and after 6 hours (lower figure). It is possible to see how some of the gamma lines have decayed due to some short-lived isotopes. Others have increased, due to isotopes with slightly longer half-lives. It can also be that two different isotopes have gamma lines with the same energy.

first days. The lines are visible in the Ge spectrum measured 2.5 hours after the proton irradiation, and they are still present after 5 days, however much weaker. After 14 days they are not visible anymore. The isotope ^{125}I is not stable and will subsequently decay to ^{125}Te (stable), but it has a half-life of 62 days and will therefore not be visible. It should also be possible to identify isotopes by looking at the gamma intensity versus time dependence and calculate the half-life. However, since the same energy lines can arise from more than one specific nuclear process, it is difficult to identify the isotopes only from their half-life. All nuclear data like decay modes and half-lives etc., are from [72].

Not all gamma lines in the measured spectra could be identified. However, through the gamma energies and, partially, gamma intensity versus time dependence, some isotopes could be identified. Table 4.5 shows the identified isotopes.

It is possible that the isotope ^{133}Ba is created in the reaction $^{133}\text{Cs}(p, n)^{133}\text{Ba}$, which has gamma lines at 356 and 160 keV. Since it has a half-life of 10 years, we should not be able to see them in such short time. However, it is the isotopes with

Table 4.5. Identified isotopes from the activated CsI(Tl) crystal. The identification was partly possible from studies of the decay of gamma lines.

Measured gamma energy (keV)	Isotope	Half-life	Energy (keV)
496, 373, 216	¹³¹ Ba	12 d	496.2, 373.2, 216.0
667	¹³² Cs	6.5 d	667.7
372, 412	¹²⁹ Cs	32.3 h	371.9, 411.5
203, 172, 375	¹²⁷ Xe	36.4 d	202.8, 172.1, 375.0
411, 287, 462, 587	¹²⁷ Cs	6.2 h	411.1, 286.6, 461.8, 586.7
188, 243	¹²⁵ Xe	17.0 h	243.4, 188.4
603, 1691	¹²⁴ I	4.2 d	602.7, 1691.0
159	¹²³ I	13.0 h	159.0
564	¹²² Sb	2.7 d	564.0
573	¹²¹ Te	16.8 d	573.1
159	¹¹⁷ Sb	2.8 h	158.6

long half-lives that could cause problems since they accumulate over time. The short-lived isotopes decay faster than the activation rate.

In figure 4.27 the total intensity (number of gamma events in the Ge-detector) is plotted as a function of the time after irradiation stopped. Clearly, the bulk of the induced activity has decreased after a few days, indicating that activation of the calorimeter crystals should not be a problem since the activation rate in space is a factor of 10^4 lower than during the TSL test.

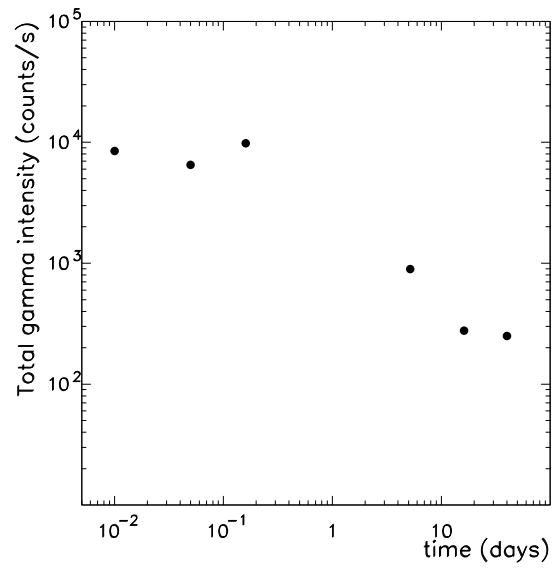


Figure 4.27. The total gamma intensity of the activated crystal measured with a Ge(Li) detector.

Chapter 5

Simulation studies of a segmented calorimeter

5.1 Shower fluctuations

The statistical nature of a cascade is usually not a problem when the shower is fully contained within the calorimeter. However, with limited calorimeter depth, individual shower fluctuations introduce leakage fluctuations that can be large and often dominate the precision of the calorimeter energy resolution. In order to interpret calorimeter data correctly, detailed knowledge of the energy fluctuations is necessary. To illustrate this point, figure 5.1 shows two individual longitudinal shower profiles, one normal and one more extreme, both induced by a 10 GeV electron in CsI as generated by Geant4 [73]. The first profile has a clear maximum and is well fitted with the Gamma distribution described by equation 3.22. The second shower profile is more irregular having two maxima, and is not as easily fitted with the Gamma distribution.

With limited calorimeter depth, fluctuations cause large uncertainties in energy estimation. This is even further enhanced in the study of study of cosmic-ray particles where the flux of particles of energy E often decreases as $dN/dE = \text{const} \times E^{-\alpha}$ with α in the range 2–3. Since one important method of energy reconstruction is to fit the longitudinal energy profile (this is further discussed in chapter 6), it is important to understand the individual shower fluctuations. Also, a good parametrisation of the energy fluctuations at a given depth can be important if part of a segmented calorimeter is malfunctioning. Although motivated by GLAST, this study is more general and focused on fluctuations in longitudinal shower samples.

In a segmented calorimeter, where the energy deposition is sampled in layers along the shower, the fluctuations of energy deposition in a layer at a given depth arise from fluctuations in starting point and development of the shower. Already in 1937 Bhabha and Heitler [74], in their work on electromagnetic cascades, studied

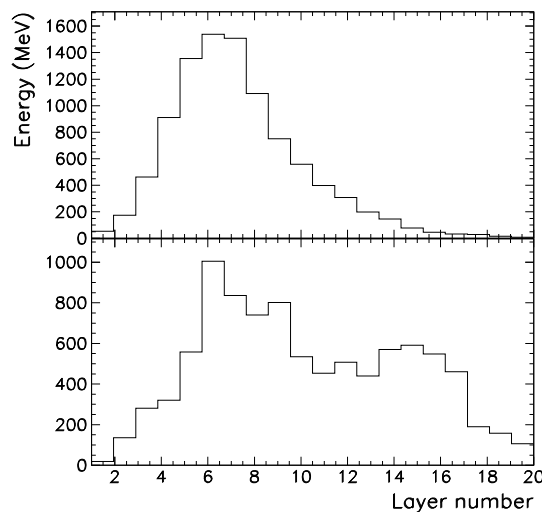


Figure 5.1. Examples of individual electromagnetic showers, induced by 10 GeV electrons as seen by a segmented CsI calorimeter. The layer thickness is 1.99 cm (1.08 radiation lengths).

fluctuations and proposed that these follow a Poisson distribution. Furry [75] used a multiplicative model for the shower development and arrived at a wider distribution, often called the Furry distribution. Mitra [76] used the negative binomial or Pólya distribution to describe the development of air showers, with the Poisson and Furry distributions as limiting cases. The Pólya distribution is mentioned in conjunction with cosmic rays for the first time in 1943 [77]. It has been used e.g. to describe photomultiplier electron statistics [78], and in particle physics to describe hadronic multiplicity distributions [79, 80]. In this latter application, an inelastic, high-energy process produces a number of particles that decay into a varying number of hadrons. In this interpretation the negative binomial describes the probability of having a n -particle production process, and its parameters describe the average multiplicity, and number of independent sources giving rise to the distribution. Fluctuations in electromagnetic cascades have been considered as an application of Markov processes [81] and analytic solutions have been found [82].

Only few experimental or simulation based studies of fluctuations at a given depth can be found in the literature. Longo and Sestili [27] have used simulations to study fluctuations in the last radiation length of lead glass of different depths for photons with energies up to 1 GeV. They compared the results of the Monte Carlo simulation with the Pólya distribution.

Gaisser [83], in discussing cosmic air showers, suggests that the fluctuations

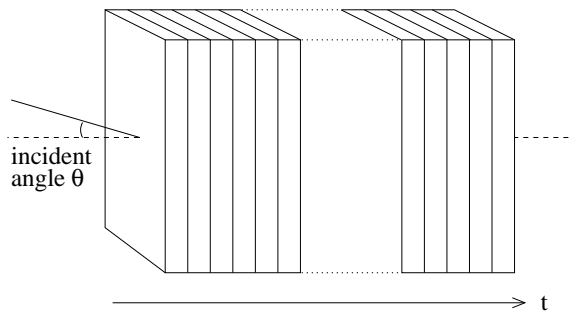


Figure 5.2. Sketch of the segmented CsI calorimeter used in the simulations. Each layer is 1.99 cm (1.08 radiation lengths), in total 20 layers were implemented.

approximately follow a log-normal distribution, reflecting the multiplicative nature of the shower development. It is also suggested that the relative fluctuations are smallest near shower maximum. In a recent paper, Souza et al. [84] studied the fluctuations of number of particles at shower maximum in air showers in order to estimate how well the shower size at maximum depth can determine the shower energy.

5.2 Simulation of energy fluctuations using Geant4

In the simulation studies the calorimeter consisted of CsI crystal layers. Each layer measured $4 \times 4 \text{ m}^2$, and had a thickness of 1.99 cm (1.08 radiation lengths). The layout is shown in figure 5.2. In order to study the basic fluctuation phenomena, the simulated calorimeter does not contain any supporting material or gaps, and in total 20 layers were implemented. Furthermore, in the simulations the energy deposited in the crystals was taken as the measured energy, i.e. no readout system has been employed in the simulations. It is clear that in a more directly project-oriented work these latter conditions must be taken into account.

The simulations were performed using Geant4 (v7.0p01), a Monte Carlo particle transport toolkit which is well supported and used by several experiments [73] including the GLAST collaboration. Only standard electromagnetic processes were considered, all photonuclear interactions have been neglected. Ajimura et al. [85] have measured these interactions to contribute to less than 2×10^{-7} in CsI for energies above 1 GeV. Electromagnetic processes are well simulated by Geant4 in the energy range relevant here, for a validation see e.g. [86]. Geant4 uses the particle range to set the energy cut-off below which secondary particles are no longer tracked and the energy is simply dumped at that location. A range cut of 1 mm was used, corresponding to an energy cut-off of 38 keV, 692 keV and 658 keV for respectively

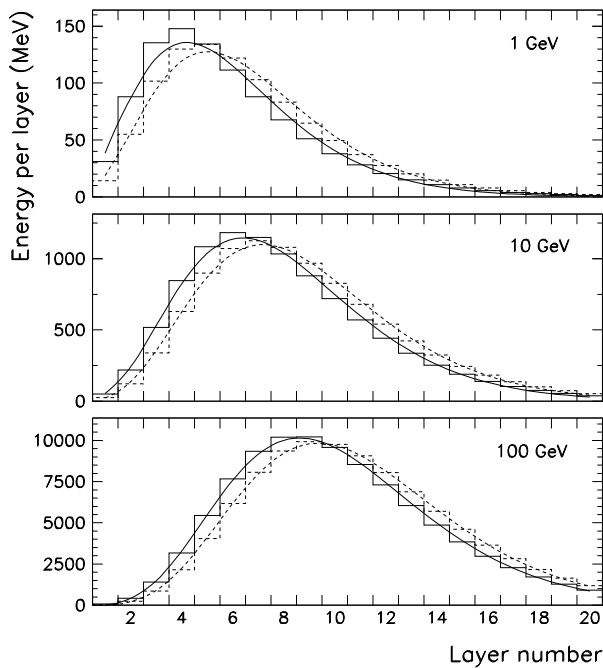


Figure 5.3. Average energy deposition in the calorimeter layers, here shown for both electrons (solid line) and photons (dashed line) having initial energies of 1 GeV, 10 GeV and 100 GeV. The distributions have been fitted with a Gamma function.

photons, electrons and positrons in CsI. Simulations were performed with incident electrons and photons in the energy range 1–100 GeV with a minimum of 100000 events in each simulation. Most studies were done with perpendicular input, but the case with non-perpendicular input having an incident angle of 30° and 60° was also examined.

5.3 Longitudinal shower profiles

Figure 5.3 shows the average longitudinal profiles of energy deposition for showers induced by electrons and photons having initial energies of 1 GeV, 10 GeV and 100 GeV. The shower maxima occur at layer 4, 6 and 8 for electrons, and at layer 5, 7 and 9 for photons. The Gamma fit gives the corresponding values 4.2, 6.1 and 8.1 (corresponding to 4.5, 6.6 and 8.7 radiation lengths) for electrons and 4.9, 6.9 and 8.7 (5.3, 7.4 and 9.4 radiation lengths) for photons. This can be compared to t_{max} calculated from equation 3.21 which gives 4.0, 6.3 and 8.6 radiation lengths for electrons and 5.0, 7.3 and 9.6 for photons. On average, the showers induced by

Table 5.1. The Gamma parameters obtained from fitting the average profiles of longitudinal energy deposition. Zero angle correspond to “on-axis” events, which have perpendicular incidence.

Particle type	Energy (GeV)	Incident angle	Gamma parameters			t_{max} (X_0)
			a	b	E_0 (GeV)	
e^-	1	0°	3.83	0.58	1.01	4.85
γ	1	0°	4.43	0.60	1.02	5.70
e^-	10	0°	5.22	0.59	10.13	7.11
γ	10	0°	5.77	0.60	10.13	7.89
e^-	10	30°	5.29	0.68	10.12	6.30
γ	10	30°	5.82	0.69	10.13	6.99
e^-	10	60°	5.87	1.19	9.96	4.09
γ	10	60°	6.32	1.19	9.99	4.48
e^-	100	0°	6.72	0.61	101.27	9.38
γ	100	0°	7.24	0.62	101.20	10.12

photons reach their maxima later than those induced by electrons. This is due to the differences in electron and photon interaction mechanisms. An electron starts losing energy immediately as it enters the calorimeter media, while photons may travel a distance before interacting. See further the work of Wigmans and Zeyrek [87] for a study on differences between photon- and electron-induced showers.

The profiles induced by the initial energies 1 GeV, 10 GeV and 100 GeV are well fitted by the Gamma distribution described by equation 3.22, returning the initial energy, E_0 , as a parameter. The energies estimated by fitting the average profiles, and the parameters a and b with corresponding t_{max} are presented in table 5.1. The non-perpendicular events are discussed in section 5.4.1.

The individual energy profiles show quite large fluctuations. To illustrate this, figure 5.4 shows the fluctuations of showers, and the resulting average profile induced by 25000 electrons with an energy of 10 GeV.

5.4 Sample fluctuations

In this study the energy fluctuations in a sample at a given depth are parametrised with the negative binomial distribution, log-normal and the Gaussian distribution. The negative binomial distribution expresses the probability of having to wait exactly r trials until k successes have occurred if the probability of a success in a single try is p . It can be interpreted as the probability for a number r of particles to be produced at a depth t . The distribution can be expressed in terms of the number of failures occurring while waiting for k successes, $n = r - k$, giving

$$P(n; k, p) = \binom{n+k-1}{k-1} p^k (1-p)^n. \quad (5.1)$$

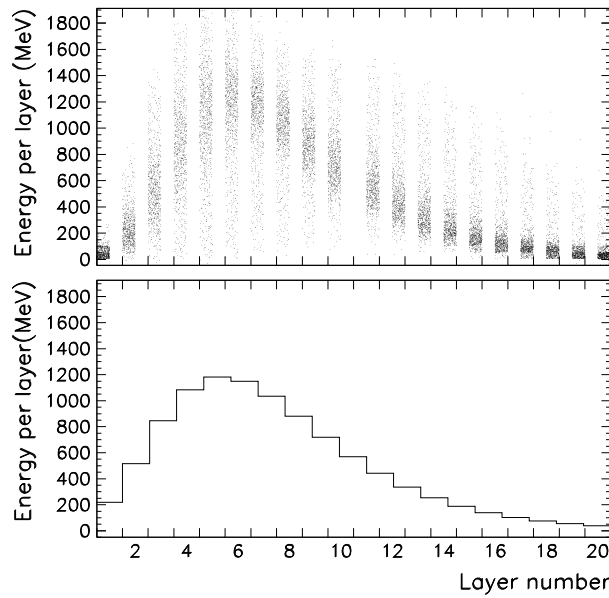


Figure 5.4. Individual longitudinal profiles for 25000 10 GeV electrons (top), and the corresponding average profile (bottom). The widths of the distributions along the abscissa are arbitrary and serve only to spread the distribution of energies for display.

Its expectation value and variance are $E(n) = k(1-p)/p$ and $V(n) = k(1-p)/p^2$ respectively. The negative binomial distribution can be regarded as a generalized form of the Poisson distribution, which is obtained when $k \rightarrow \infty$ [88]. The Poisson distribution has a variance equal to the average whereas the negative binomial has a variance larger than the average, thus a wider distribution. Excluding the case $n = 0$ in the negative binomial and letting $k \rightarrow 0$ the distribution becomes logarithmic $P(n; p) = -(1-p)^n / n \ln p$ [88].

The log-normal distribution is given by

$$P(x; \mu, \sigma^2) = \frac{1}{\sqrt{2\pi\sigma^2}} \frac{1}{x} \exp\left(-\frac{(\log x - \mu)^2}{2\sigma^2}\right). \quad (5.2)$$

Note that μ and σ^2 are not the expectation value and variance of x , but rather the parameters of the corresponding Gaussian distribution for $\log x$.

Figures 5.5–5.7 show how the fluctuations change from layer to layer in the first 15 layers (16 radiation lengths) for 1 GeV, 10 GeV and 100 GeV incident energies. The energy fluctuations in layer 16–20 have the same exponential-like shape as layer 15, only shifted towards lower energy as the depth increases, and are not shown here. The differences between electron- and photon-induced showers

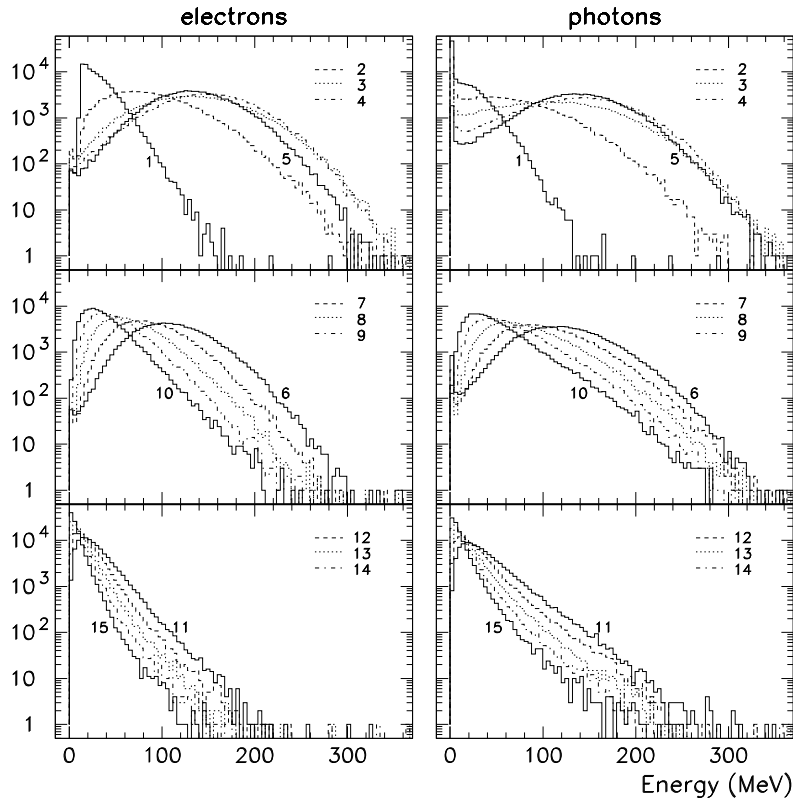


Figure 5.5. Fluctuations of energy deposition in the CsI calorimeter layers for showers induced by 1 GeV electrons and photons. The histograms show the number of events depositing in an energy interval corresponding to the bin size (here 4 MeV). Each layer of CsI is 1.99 cm (1.08 radiation lengths) thick.

are clearly seen. Electrons have a clearer peak in the energy distribution whereas photons, having a probability of non-interacting, give wider distributions with a less pronounced peak. All of the 10 GeV electrons have deposited energy in the first layer (1.08 radiation lengths) whereas about 5% of the 10 GeV photons have not interacted at this depth.

The shape of the energy fluctuations changes systematically with depth for the three different energies (1 GeV, 10 GeV and 100 GeV). Both electron- and photon-induced showers show fluctuations with a high-energy tail at small depths, which is reduced as the depth increases and the distribution becomes more symmetric and Gaussian-like. Moving deeper into the calorimeter, a low-energy tail develops. Eventually the fluctuations become more symmetric again, and finally a high-energy tail emerges. This behaviour of the energy distributions can be readily understood

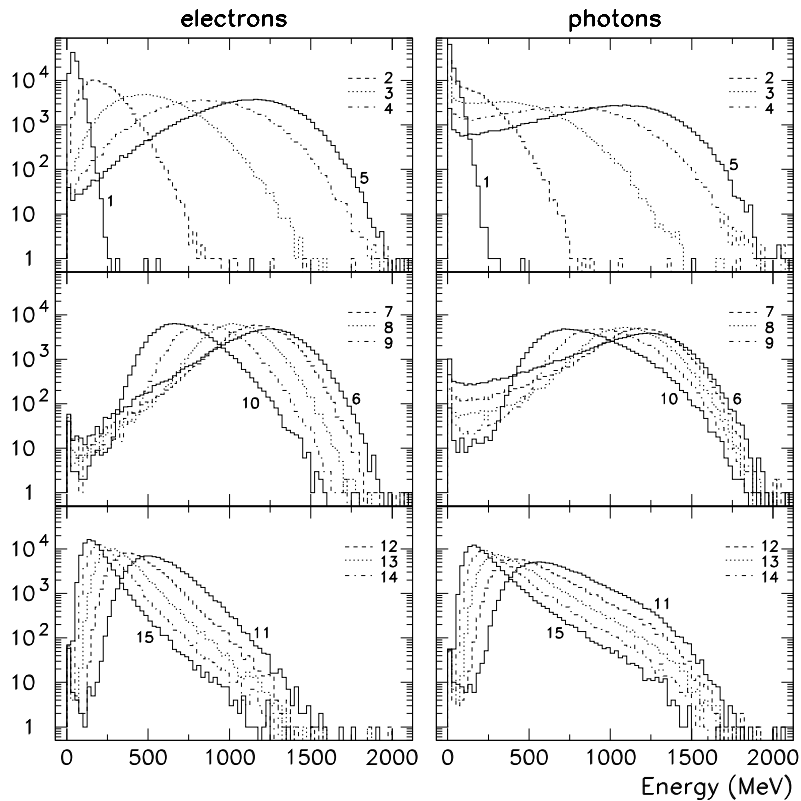


Figure 5.6. Fluctuations of energy deposition in the calorimeter layers, here shown for showers induced by 10 GeV electrons and photons. The histograms show the number of events depositing in an energy interval corresponding to the bin size (here 25 MeV). Each layer of CsI is 1.99 cm (1.08 radiation lengths) thick.

from fluctuations in the shower developments. Indeed, in the first few radiation lengths early shower developments can give rise to large total energy deposits giving a high energy tail. At the location of the average maximum energy deposition, fluctuations to higher energies are less frequent than those to lower energies, giving distributions with a slight low-energy tail. The most symmetric Gaussian-like distributions occur just before and after the maximum energy deposition where there are both high- and low-energy contributions from early respectively late initiated showers. These tendencies become more pronounced with increasing energy as the longitudinal shower profile becomes more stretched out.

The energy fluctuations in each layer were fitted with negative binomial, log-normal and Gaussian distributions for incident electrons and photons of energy 1 GeV, 10 GeV and 100 GeV. The fits were performed over a range in energy

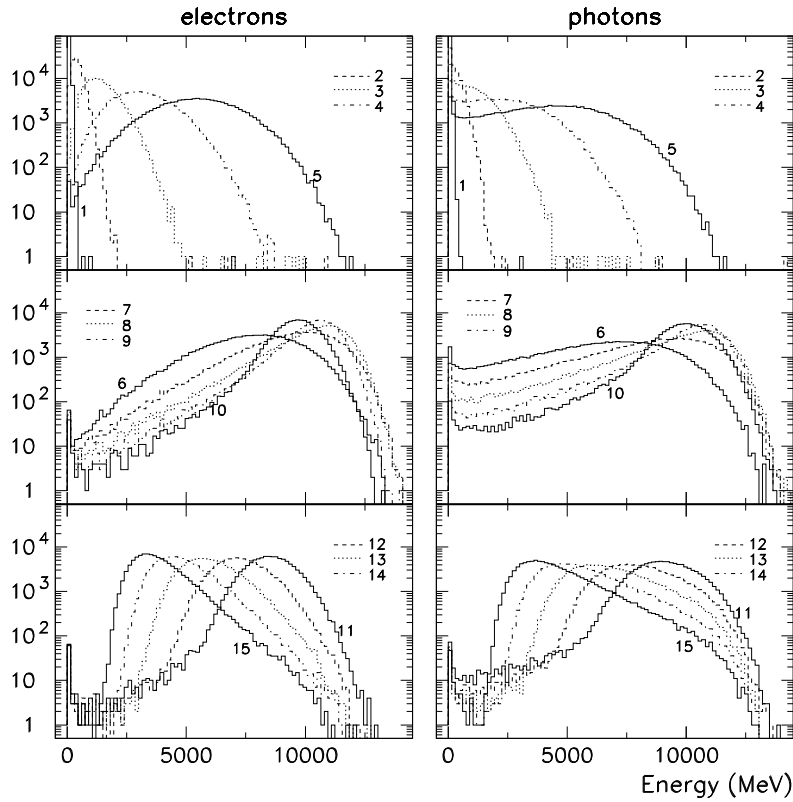


Figure 5.7. Fluctuations of energy deposition in the calorimeter layers, here shown for showers induced by 100 GeV electrons and photons. The histograms show the number of events depositing in an energy interval corresponding to the bin size (here 150 MeV). Each layer of CsI is 1.99 cm (1.08 radiation lengths) thick.

corresponding to 1% of the peak value of the distribution. As expected from the variations as function of depth, quality of fits varies considerably and in most cases there are deviations from the fit due to the tails of the distributions. An important conclusion from the fits is that for each layer one – but not the same – distribution gives the best fit. With 100000 simulated events only a few layers give a fully acceptable fit as judged by the χ^2 . Lowering the number of events will decrease the χ^2 -value and increase the goodness of the fit.

As an example figure 5.8 shows the 10 GeV electron and photon energy distributions in layers 5, 8 and 12 (4.8, 8.1 and 12.4 radiation lengths).¹ These three layers are before, close to and after the shower maximum. The fitting range covers

¹The corresponding radiation length is here taken to be the distance from the calorimeter front to the centre of the layer.

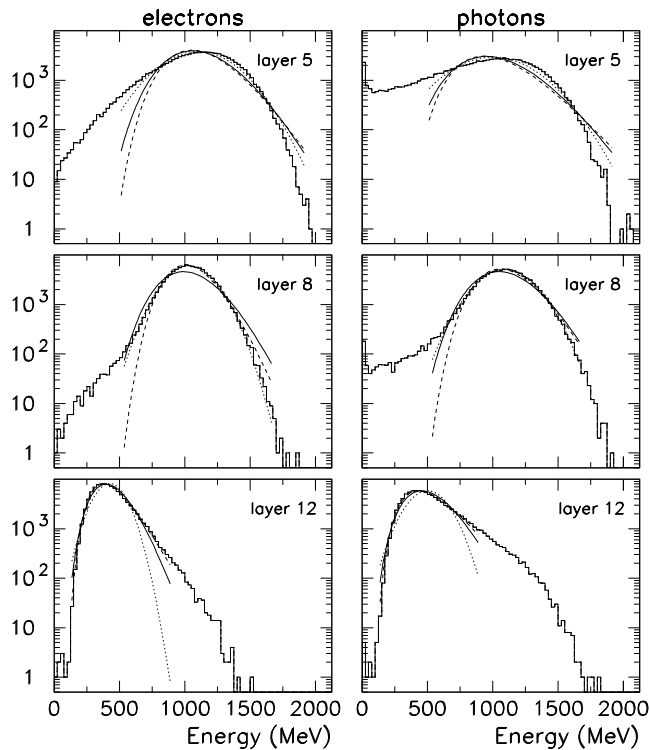


Figure 5.8. Fitting the energy fluctuations for incident electrons and photons having an initial energy of 10 GeV with negative binomial (solid line), log-normal (dashed line) and Gaussian (dotted line) distributions. The histograms show the number of events depositing in an energy interval corresponding to the bin size (here 25 MeV). The fitting range covers 97.1%, 99.5% and 98.9% (88.8%, 97.8% and 98.4%) of the distribution for electrons (photons).

96.7%, 99.3% and 98.6% (82.1%, 97.8% and 91.6%) of the 100000 events in the simulation for electrons (photons). The low energy tails in layers 5 and 8 are not well fitted. The high energy tails are quite well described by the log-normal or negative binomial distributions. Figure 5.9 shows as function of layer number the reduced χ^2 of the fits, giving a relative evaluation of how well the three distributions fit the energy fluctuations. The systematic change of the fluctuations with depth can be seen. The reduced χ^2 is included in figure 5.9 for layers 16–20 although the number of events there is small.

For 1 GeV incident electrons and photons, the Gaussian distribution gives the best fit in the first 5 layers which is expected since the average shower maximum occurs in layer 4. At larger depths the energy fluctuations are best fitted with the negative binomial. Note that the energy fluctuations become close to exponential

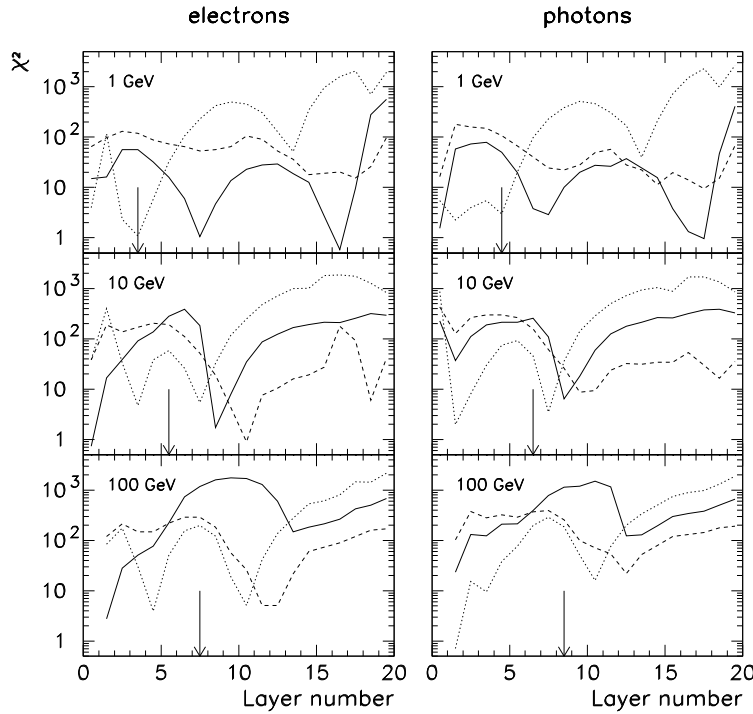


Figure 5.9. The reduced χ^2 of the negative binomial (solid line), log-normal (dashed line) and the Gaussian (dotted line) fit for 1 GeV, 10 GeV and 100 GeV electrons and photons. The lines have been drawn to guide the eye. The arrows mark the average shower maximum.

at layer 14 and beyond, giving a large uncertainty in the fitted parameters. For 10 GeV, the Gaussian distribution gives the best fit a few layers before and after the average shower maximum, as expected. When the high-energy tail emerges the best fit is given by the negative binomial and as it becomes more prominent the log-normal. For 100 GeV, the Gaussian again gives the best fit before and after the location of the shower maximum, and when the high-energy tail emerges the log-normal distribution gives the best fit. The negative binomial gives quite a good fit up to layer 4, but after that it completely fails. There are no larger differences in the χ^2 between electron- and photon-induced showers since the width changes but not the shape of the fluctuations.

Figures 5.10–5.12 show the parameters from the fits as a function of energy. The plateau emerging at high energies in figure 5.10 for the negative binomial parameter k is due to the extremely poor fit of the fluctuations in the mid-layers.

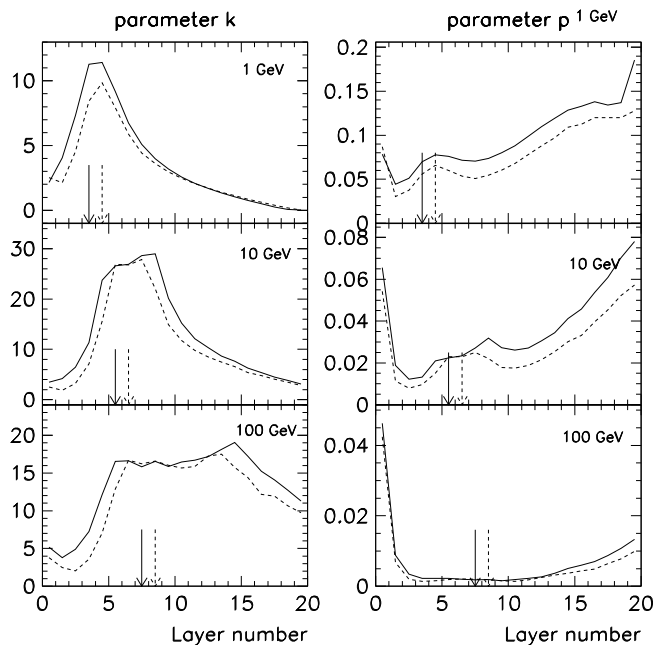


Figure 5.10. The negative binomial parameters as a function of layer, for 1 GeV, 10 GeV and 100 GeV electrons (solid line) and photons (dashed line). The lines have been drawn to guide the eye. The arrows mark the average shower maximum.

The parameter μ of the log-normal and the Gaussian distributions corresponds to the logarithm of the expectation value and the expectation value, respectively. Figures 5.11 and 5.12 show that its peak value corresponds well to the location of the average shower maximum both for electrons and photons.

Because of the large fluctuations in shower development, the energy deposited in a calorimeter with limited depth shows large fluctuations. This is illustrated in figure 5.13 showing the distribution of the total energy measured in 8 layers (8.6 radiation lengths, corresponding to the depth of the GLAST calorimeter) of CsI are illustrated in figure 5.13. The results for three initial energies, 10 GeV, 50 GeV and 100 GeV, each with 100000 events with 0° incident angle, are shown both for electrons and photons. No events deposited zero energy in the calorimeter. The top panel shows unscaled energy distributions, whereas the distributions shown in the bottom panel the intensities have been scaled following a typical cosmic-ray $E^{-2.7}$ flux dependence. The energy loss distributions show a low-energy tail which increases with particle energy. This is due to the decreased longitudinal containment of the showers with increasing incident energy. As expected, contaminations be-

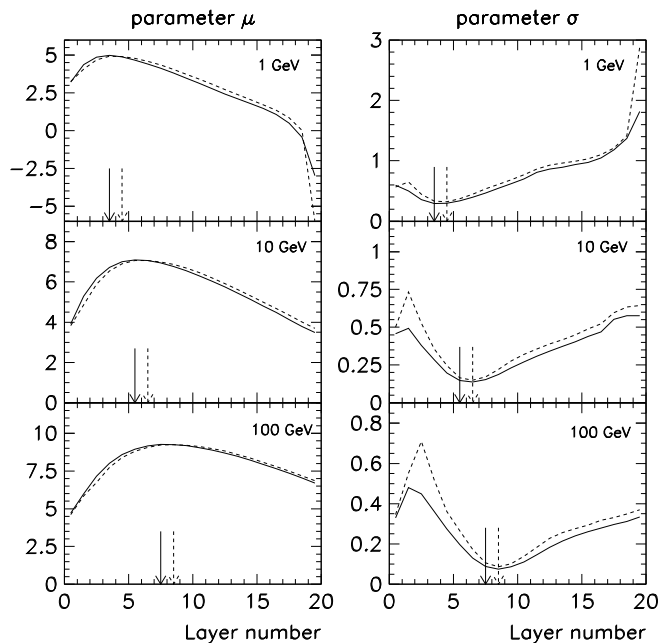


Figure 5.11. The log-normal parameters as a function of layer, for 1 GeV, 10 GeV and 100 GeV electrons (solid line) and photons (dashed line). The lines have been drawn to guide the eye. The arrows mark the average shower maximum.

tween showers of different energies are larger for photons than for electrons. About 59% of the 100 GeV photons fall in the range for 50 GeV photons. For electrons the corresponding contamination is about 34%.

5.4.1 Non-perpendicular incidence

Since the shower is induced in the same direction as the incident particle, a shower induced at an angle is not sampled perpendicular to its longitudinal axis. Therefore, a non-perpendicular input will result in a larger energy deposit in each layer, and it does not reach as deep into the calorimeter as a perpendicular input of same energy. This is clearly seen in figure 5.14 which compares the average longitudinal energy profiles for 10 GeV electrons and photons having an angle of incidence of 0° , 30° and 60° . The longitudinal profile for events with 30° incidence reaches its maximum slightly earlier than the 0° profile, and it also shows a somewhat faster development with larger energy deposition. The 60° profile, however, has a much more compact energy deposition, reaching its maximum much earlier. Each

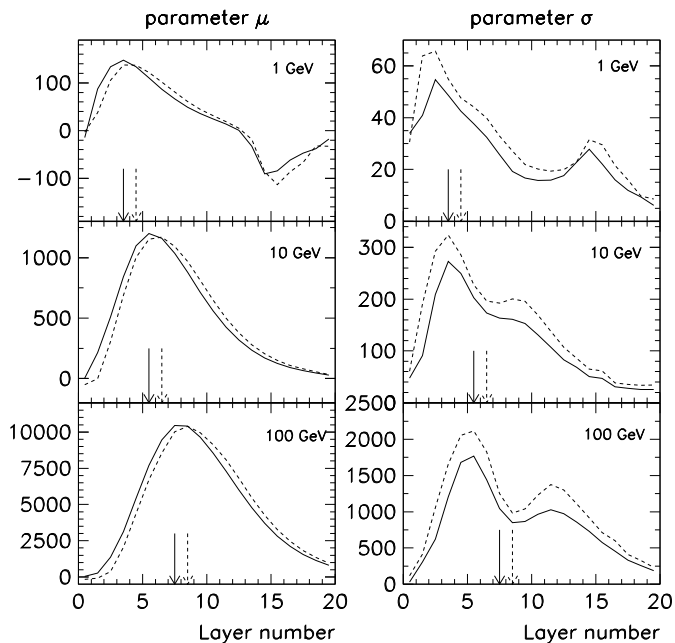


Figure 5.12. The Gaussian parameters as a function of layer, for 1 GeV, 10 GeV and 100 GeV electrons (solid line) and photons (dashed line). The lines have been drawn to guide the eye. The arrows mark the average shower maximum.

of the average longitudinal profiles was fitted with a Gamma distribution, and the resulting parameters are shown in table 5.1.

The energy fluctuations in the calorimeter layers for non-perpendicular incidence behave in the same way as the events with normal incidence. Figures 5.15 and 5.16 show how the energy deposition is distributed in the calorimeter layers for incident angles 30° and 60° . Fluctuation distributions for events with 30° incidence are quite similar to the 0° distributions, but the more rapid shower development is evident as the angle of incidence increases.

5.5 Discussion

The average energy deposition of the simulated showers in the CsI layers is well described with a Gamma distribution both for electrons and photons. Electron-induced showers reach their energy deposition maximum somewhat earlier than the photon-induced ones due to the differences in electron and photon interaction mechanisms.

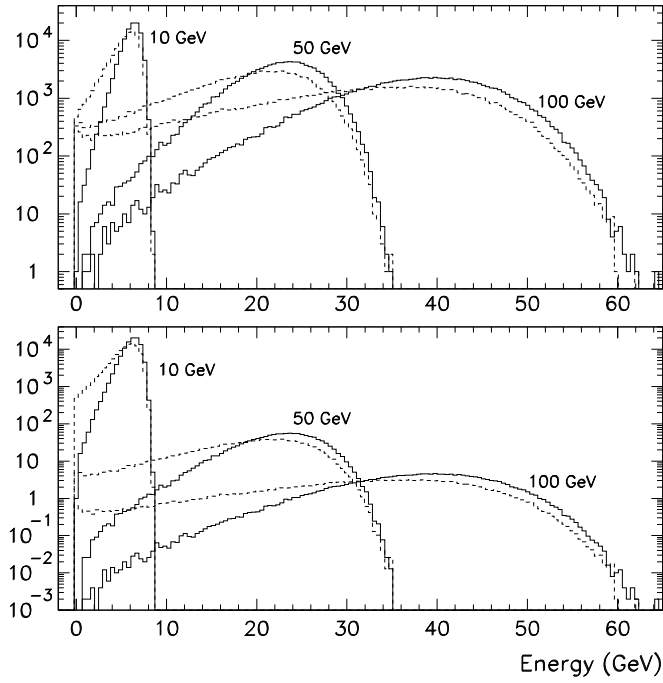


Figure 5.13. The total energy deposited in the CsI calorimeter having 8 layers. The top panel shows the energy distribution of 100000 events each of electrons (solid line) and photons (dashed line) having 1 GeV, 50 GeV and 100 GeV initial energy. In the bottom panel the intensities have been scaled with the cosmic-ray spectrum with $\alpha = 2.7$.

The simulations show that the shape of the energy fluctuations vary significantly with the calorimeter depth. When comparing the energy fluctuations over the calorimeter depth for three initial energies 1 GeV, 10 GeV and 100 GeV, it is clear that this change is systematic. The variations are similar for electrons and photons and can be understood by considering the average longitudinal development of the shower. In the first layers the fluctuations show a high-energy tail due to early large energy deposits. Before and after the location of the average shower maximum, the energy deposition may fluctuate both to lower and higher energies giving a more symmetric distribution. At the depth corresponding to the average shower maximum, the fluctuations have a low-energy tail since the energy deposition can only be equal to or smaller than the maximum. Deep into the calorimeter where most of the showers have started to diminish, a high-energy tail emerges from the

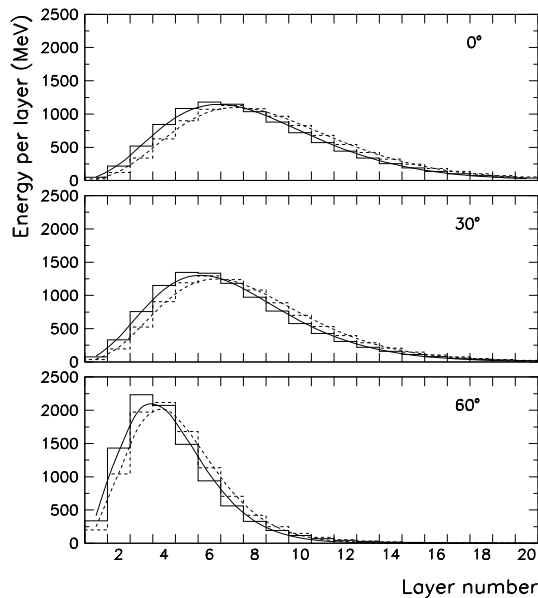


Figure 5.14. Average longitudinal energy profiles for 10 GeV electrons (solid line) and photons (dashed line) of 0° (perpendicular incidence), 30° and 60° incident angle.

symmetric distribution which finally grow into an exponential-like distribution.

None of the three probability distributions give an acceptable fit over the full shower length. The Gaussian distribution gives the best fit to the energy fluctuations in the region before and after the average shower maximum. The negative binomial and log-normal distributions give best fit to the fluctuations a few layers after the shower maximum, when the fluctuations have developed a high-energy tail. However, at 100 GeV the negative binomial fails to fit the energy fluctuation in any layer.

The energy fluctuations generated from non-perpendicular input are similar compared to those for perpendicular input. As expected, the shower development is more compact with a larger energy deposit in the layers around the maximum. Their shower maximum is located earlier, and the showers do not reach as deep into the calorimeter as a perpendicular input of same energy. These features are more pronounced as the angle increases.

The total energy measured in 8 layers (8.6 radiation lengths) for the three initial energies, 10 GeV, 50 GeV and 100 GeV and perpendicular input, show that contaminations between showers of different energies are larger for photons than for electrons. About 30% of the 100 GeV electrons fall in the range for 50 GeV electrons, and for photons the corresponding contamination is about 55%.

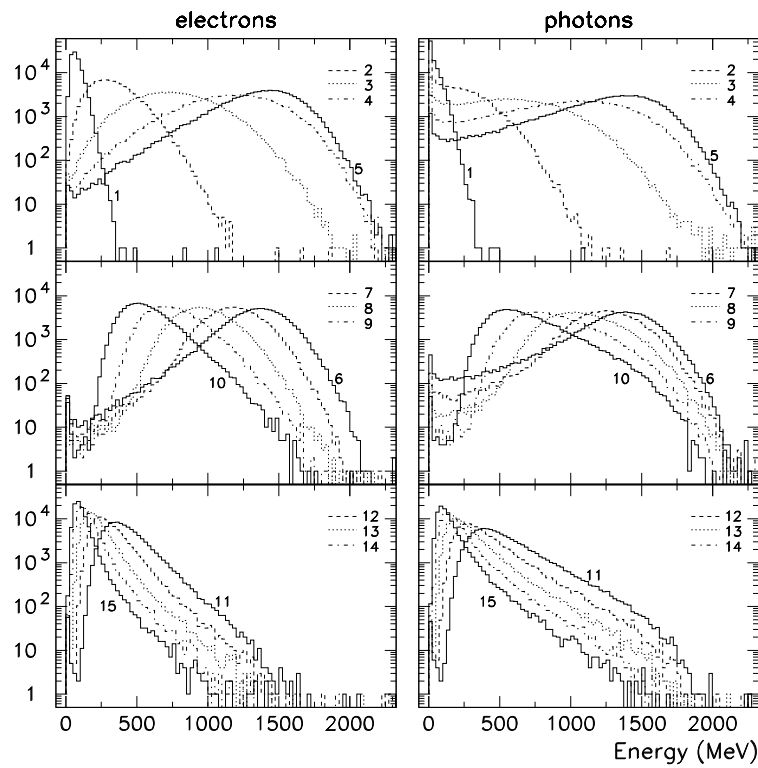


Figure 5.15. Fluctuations of energy deposition in the calorimeter layers, here shown for showers induced by 10 GeV electrons and photons at 30° incident angle. The histograms show the number of events depositing in an energy interval corresponding to the bin size (here 25 MeV). Each layer of CsI is 1.99 cm (1.08 radiation lengths).

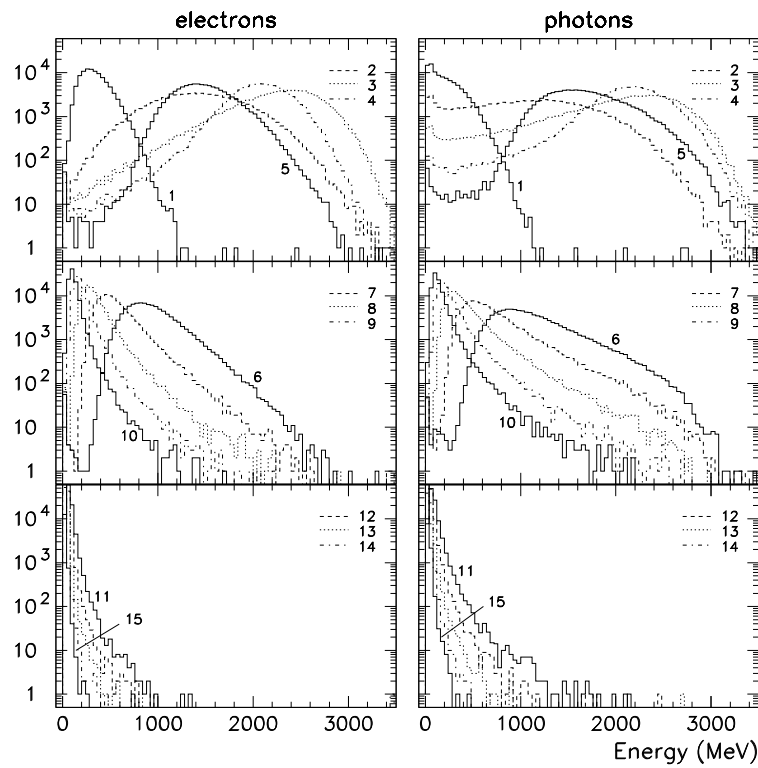


Figure 5.16. Fluctuations of energy deposition in the calorimeter layers, here shown for showers induced by 10 GeV electrons and photons at 60° incident angle. The histograms show the number of events depositing in an energy interval corresponding to the bin size (here 25 MeV). Each layer of CsI is 1.99 cm (1.08 radiation lengths).

Chapter 6

Energy estimation in a segmented calorimeter

6.1 Energy reconstruction methods

The most straightforward way to reconstruct the energy of the incident particle is by summing the energy deposited in the calorimeter layers. Using this simple reconstruction method, the energy resolution is then simply the variance of the distributions. This method is feasible when the shower is well contained in the calorimeter, but as the incident energy increases, energy leakage deteriorates the energy resolution and introduces a non-linear response of the calorimeter. This is clearly seen in figure 5.13 of chapter 5, where the total energy deposition in 8 layers (8.6 radiation lengths) is shown for 10 GeV, 50 GeV and 100 GeV electrons and photons.

In segmented calorimeters there exist several other ways of reconstructing the energy of the incident particle using information from the segments, and often more than one method are implemented in the reconstruction algorithms. Two main correction techniques are currently employed in GLAST, and have been tested experimentally in a beam test [89] with $10X_0$ deep calorimeter having 2.3 cm thick layers.

The first is to fit the longitudinal energy profile with the Gamma function (equation 3.22). This is a frequently used energy reconstruction method in segmented calorimeters, and also in air-shower experiments. It is based on the knowledge of the average longitudinal profile whose parameters depend on energy. The second method corrects for the energy leakage. It uses the correlation between the escaping energy and the energy deposited in the last layer of the calorimeter. These methods are however only applicable as long as the shower maximum is contained within the calorimeter.

In this chapter different methods for energy estimation are discussed and simulation results presented. In addition there will be a short discussion of the maximum likelihood method, however the focus will be on the shower profile fitting and last layer corrections. The analysis is based on the simulations described in chapter 5, and includes only events with perpendicular incidence.

6.1.1 Shower profile fitting

One of the advantages of a segmented calorimeter is that there are information about the development of the shower. If the individual showers behaved much like the average shower, the initial energy E_{true} can simply be extracted from the position of the shower maximum t_{max} by using for example equation 3.21. The maximum is taken to be the layer (in radiation lengths) with the maximum energy deposition. However, the individual shower fluctuations introduce large deviations of the location of t_{max} as compared to the average maximum $\langle t_{max} \rangle$. This is evident in for example figure 5.1. The longitudinal profile fitting method is in this case a better method since it takes into account the energy deposition in all layers.

The distributions of the Gamma parameters, a , b and E_0 (the initial energy), were studied by fitting individual showers induced by electrons and photons of initial energies of 1 GeV and 10 GeV. The result from fitting 25000 individual showers induced by 10 GeV electrons and photons are shown in figure 6.1 for a 20 layer (21.5 radiation lengths) calorimeter, and in figure 6.2 for a GLAST-like calorimeter of 8 layers (8.6 radiation lengths). The parameters a and b are strongly correlated and approximately follow a log-normal and a Gaussian distribution respectively. As expected, the a and b distributions are wider for photons than for electrons. The average values $\langle a \rangle$, $\langle b \rangle$ and the corresponding $\langle t_{max} \rangle$ (from equation 3.23) for the energies 1 GeV and 10 GeV are given in table 6.1.

The strange feature in the scatter-plot of a and b in figure 6.1 for 10 GeV photons, with a strong negative correlation between a and b , corresponds to late

Table 6.1. The average parameters obtained from fitting 25000 individual longitudinal profiles with a Gamma distribution.

Particle type	Energy (GeV)	No. layers	parameter a		parameter b		$\langle t_{max} \rangle$ (X_0)
			$\langle a \rangle$	σ_a	$\langle b \rangle$	σ_b	
e ⁻	1	20	4.81	1.30	0.80	0.22	4.76
γ	1	20	6.17	1.43	0.97	0.30	5.33
e ⁻	10	20	5.70	1.16	0.67	0.11	7.01
γ	10	20	6.75	1.26	0.75	0.15	7.67
e ⁻	1	8	5.42	1.38	1.01	0.44	4.38
γ	1	8	7.17	1.55	1.26	0.52	4.90
e ⁻	10	8	6.42	1.23	0.88	0.26	6.16
γ	10	8	7.54	1.30	1.03	0.31	6.35

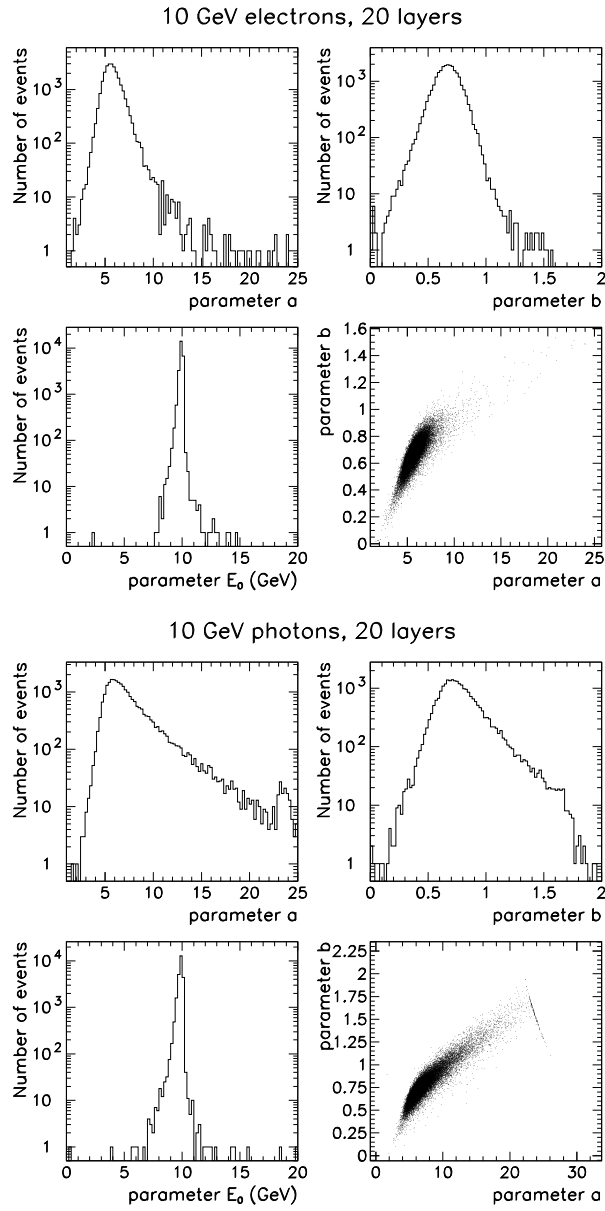


Figure 6.1. Distribution of Gamma parameters a , b and E_0 obtained from fitting individual shower profiles. The showers were induced by 10 GeV electrons (top figure) and photons (bottom figure), each with 25000 events. All 20 layers were included in the fit.

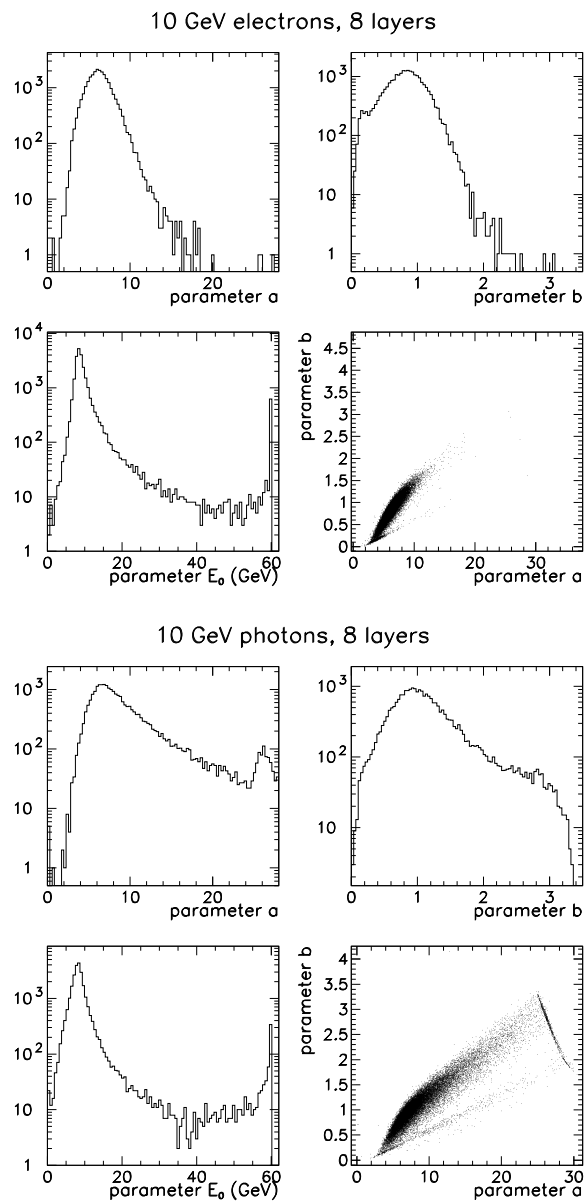


Figure 6.2. Distribution of Gamma parameters a , b and E_0 of individual shower profiles in the first 8 layers. The fitted showers were induced by 10 GeV electrons, and the simulation included 25000 events.

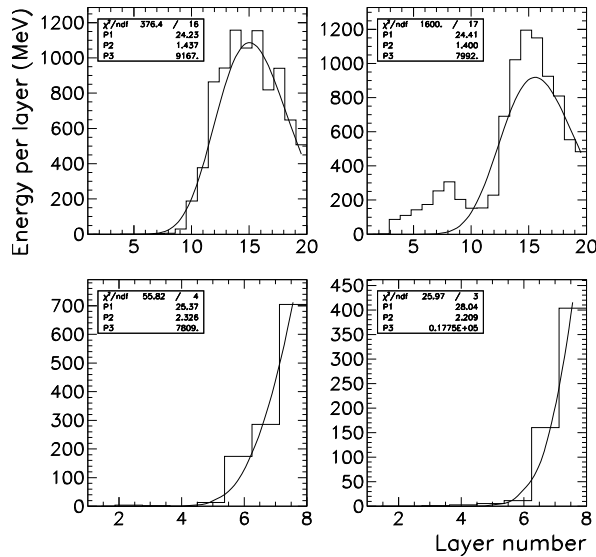


Figure 6.3. Typical 10 GeV photon events with large values of the parameters a and b . The upper panel shows events sampled in 20 layers and the bottom panel events sampled in the 8 first layers.

developed showers. It is visible as a straight line with about 1% of the events, for high values of a and b . The feature is also present in the a and b distributions as small peaks. These events, however, do not in general give a poor estimation of E_0 , but as a increases, the energy is overestimated. In the case of electron-induced showers, which in general develop as soon as they enter the calorimeter, this feature is not present. Some examples of photon-induced showers yielding these negative correlated values of a and b are shown in the upper panels of figure 6.3. The same feature is also present in the case of 8 layers (figure 6.2) also corresponding to showers induced late, as shown in the bottom panel of figure 6.3. The negative correlation between a and b is more pronounced in the case with 8 layers, since with fewer layers the maximum is outside the calorimeter resulting in larger values of a .

The distribution of the parameter E_0 varies considerably with energy and with calorimeter depth. With 20 layers the showers are well contained, and the resulting energy resolution is of the order of a few percent (table 6.2). For 10 GeV electrons and photons a fraction of 0.1% of the events gives E_0 values larger than 11 GeV and about 0.5% gives E_0 values less than 9 GeV. For a calorimeter with 8 layers the widths of the distributions are significantly larger, and E_0 values larger than 20 GeV are present at the 1% level. The high-energy tail is due to fluctuating

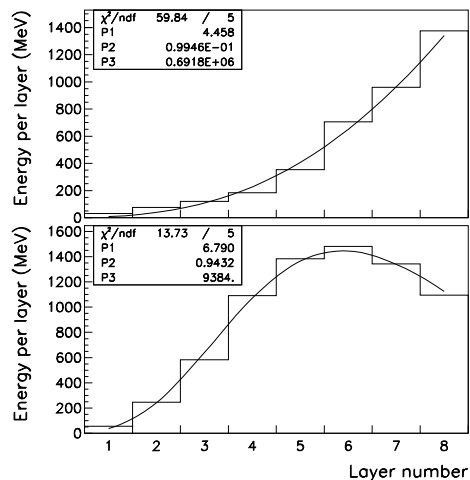


Figure 6.4. Longitudinal shower profiles initiated by an on-axis 10 GeV photon. The profiles have been fitted with Gamma distributions, with parameters a (P1), b (P2) and E_0 (P3).

events not having a clear maximum within the calorimeter, thus overestimating E_0 . Figure 6.4 shows examples of two individual showers initiated by a 10 GeV photon, both fitted with the Gamma distribution. In the lower panel the shower maximum is located in layer 6, and the fitted parameters give $t_{max} = 6.1$ radiation lengths, which corresponds approximately to the average shower maximum, and the fit results in a value of $E_0 = 9.4$ GeV. In the top panel, the maximum is not visible within the seven first layers yielding $E_0 = 691.8$ GeV, a largely overestimated value of initial energy.

The peak in the E_0 distribution around 60 GeV in figure 6.2 is due to the parameter boundary of E_0 set to 60 GeV during the fit. It also appears in the scatter-plot of a and b as a straight line with smaller slope, all events (about 2–3% of total) having an estimated energy of $E_0 \approx 60$ GeV. It is also recognisable in the case of electrons, however with much fewer events. Table 6.2 shows the average energy $\langle E_0 \rangle$ and the fluctuation σ_E obtained for the energies 1 GeV and 10 GeV. It also compares the extent of the low- and high-energy tails of the E_0 distribution.

If only events with maximum located within the first 7 layers are selected, this overestimation is reduced. This is shown in figure 6.5, where E_0 is plotted for events fulfilling this criteria. The number of fits yielding overestimated values of E_0 is clearly reduced.

It is also possible to reduce the overestimation of the initial energy by constraining the parameters of the fit. This can be achieved by parametrising the

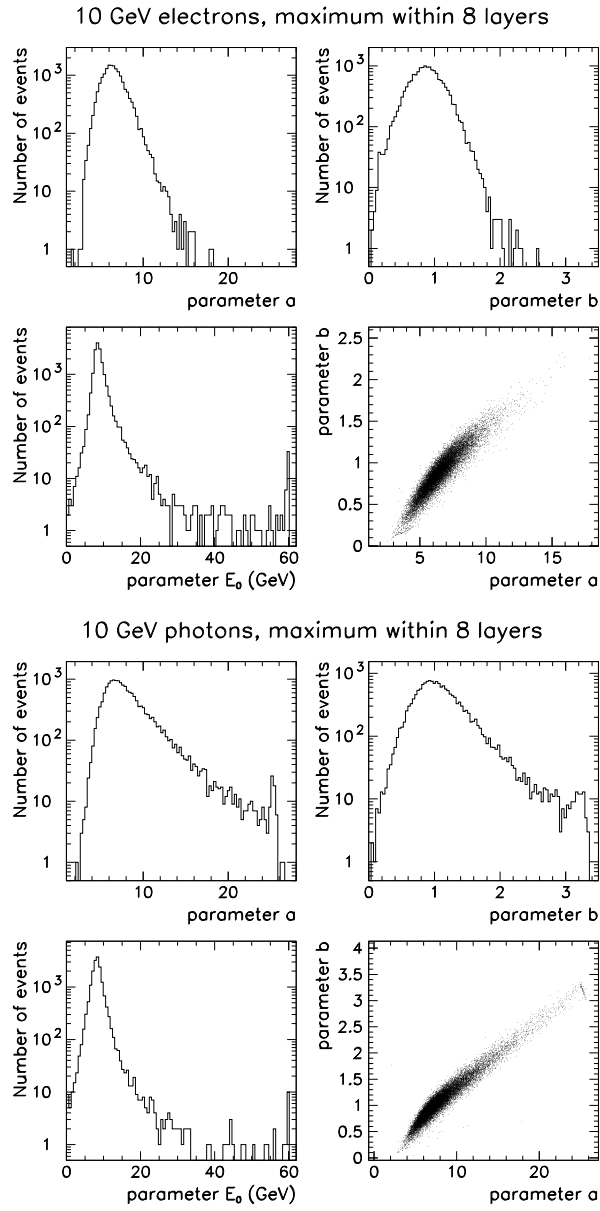


Figure 6.5. Distribution of Gamma parameters a , b and E_0 of individual shower profiles in the first 8 layers. Only events with maximum within the first 7 layers are included.

Table 6.2. The average E_0 obtained from shower profile fitting. Events with a maximum within the first 7 layers are denoted (max).

Particle type	Energy (GeV)	No. layers	parameter E_0 (GeV)				
			$\langle E_0 \rangle$	σ_E	$\frac{\sigma_E}{E}$ (%)	Fraction (%)	
						$< 0.9E_{true}$	$> 1.1E_{true}$
e^-	1	20	0.91	0.04	4.4	40	0.1
γ	1	20	0.90	0.04	4.9	50	0.2
e^-	10	20	9.9	0.2	2.3	0.3	0.1
γ	10	20	9.8	0.2	2.4	0.8	0.1
e^-	1	8	0.83	0.09	10.7	73	11
γ	1	8	0.79	0.10	12.1	80	8
e^-	10	8	8.6	1.0	13.0	56	19
γ	10	8	8.2	1.2	14.8	68	14
e^-	1	8 (max)	0.83	0.09	10.4	75	9
γ	1	8 (max)	0.79	0.10	13.1	84	5
e^-	10	8 (max)	8.6	1.1	12.3	63	10
γ	10	8 (max)	8.2	1.3	15.4	75	6

profile parameters and their fluctuations as a function of the energy. Grindhammer et al. [35] have developed parametrisations of simulated electromagnetic showers in the energy range 1–100 GeV, where shower to shower fluctuations are taken into account. Using the variables $y = \frac{E}{E_c}$, where E_c is the critical energy, and $t_{max} = (a - 1)/b$, the average longitudinal profiles and their fluctuations can be described by

$$\begin{aligned}
 \langle \ln a \rangle &= \ln(A_0 + A_1 \ln y) \\
 \langle \ln t_{max} \rangle &= \ln(B_0 + \ln y) \\
 \sigma_{\langle \ln a \rangle} &= (C_0 + C_1 \ln y)^{-1} \\
 \sigma_{\langle \ln t_{max} \rangle} &= (C_0 + C_1 \ln y)^{-1}
 \end{aligned} \tag{6.1}$$

where E is the incident energy of the particle, and A, B and C are constants. The correlation between $\ln a$ and $\ln t_{max}$ is given by

$$\rho(\ln t_{max}, \ln a) = D_0 + D_1 \ln y.$$

Then during the fit, one can constrain the parameters using these relations. The constraint depends of the containment of the shower; the less the shower is contained, the more the profile should tend to the average profile.

The radial profile becomes important if there are radial leakage. This can happen if the shower develops close to calorimeter sides or when part of the shower passes through the gaps within the calorimeter. The radial distribution was described in section 3.2.2, and varies with longitudinal depth of the shower according to equation 3.27. This is however not studied in this thesis, see for instance [90] for more information about how the radial profile is used in the energy reconstruction in GLAST.

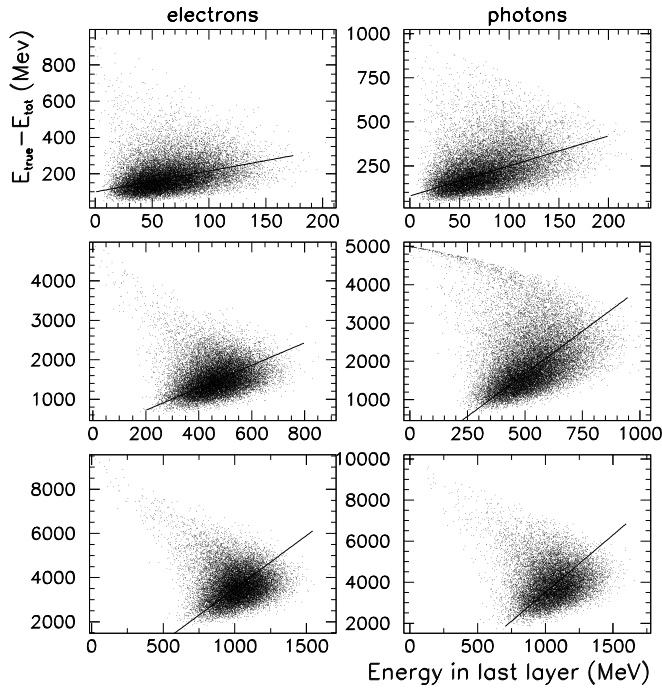


Figure 6.6. Total energy deposited in 8 layers by 1 GeV, 5 GeV and 10 GeV electrons versus the energy deposited in last layer. The number of events in the simulation are 25000. The straight lines are the bi-dimensional fits to the data.

6.1.2 Energy leakage compensation

After the shower maximum, the multiplication of particles has stopped and the energy of the shower particles are at the critical energy. Thus, the total number of particles escaping through the back should be proportional to the energy deposited in the last layer. Using this correlation between the energy deposited in the last layer and the total energy deposited in the calorimeter, the energy leakage can be estimated. This is however only feasible for showers having its maximum within the calorimeter. The energy corrected for leakage is

$$E_{corr} = E_{tot} + E_{leak} = E_{tot} + k \cdot E_8, \quad (6.2)$$

where E_{tot} is the total energy deposited in the calorimeter, E_8 is the energy deposited in the last layer and k is a constant. k can be found by plotting $E_{true} - E_{tot}$ as a function of E_8 , and should be positive since a larger E_8 must correspond to a larger leakage. Figure 6.6 shows the correlation between $E_{true} - E_{tot}$ as a function of E_8 for 1 GeV, 5 GeV and 10 GeV electrons. In order to find the slope of the

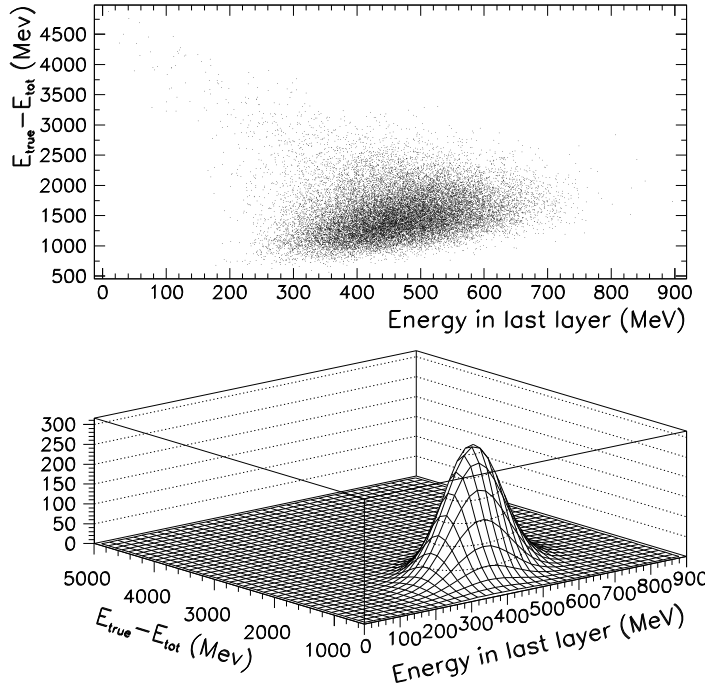


Figure 6.7. Example of a bi-dimensional Gaussian fit of $E_{true} - E_{tot}$ versus E_8 for 5 GeV electrons.

distribution, it was fitted with a bi-dimensional Gaussian

$$f(E_8, E_{tot}) = A \exp \left[-\frac{1}{2\sigma} \left(\frac{x'^2}{\alpha^2} + \frac{y'^2}{\beta^2} \right) \right] \quad (6.3)$$

$$\begin{aligned} x' &= (E_8 - E_8^{max}) \cos \theta + (E_{tot} - E_{tot}^{max}) \sin \theta \\ y' &= -(E_8 - E_8^{max}) \sin \theta + (E_{tot} - E_{tot}^{max}) \cos \theta \end{aligned}$$

This is an ellipse with centre at $(E_8^{max}, E_{tot}^{max})$, α and β are the major and minor axis respectively, A is a normalisation constant and θ is the angle of the major axis to the x -axis and from which the slope k can be obtained. An example of the bi-dimensional Gaussian fit is shown in figure 6.7, where the energy leakage versus the energy deposited in the last layer is fitted for 5 GeV electrons.

The last layer correction method was found to be feasible for events with energy 1–10 GeV. At higher energies the shower is less and less contained, and the correlation between the leakage energy and E_8 becomes negative. Figure 6.8 shows this for 50 GeV and 100 GeV electrons.

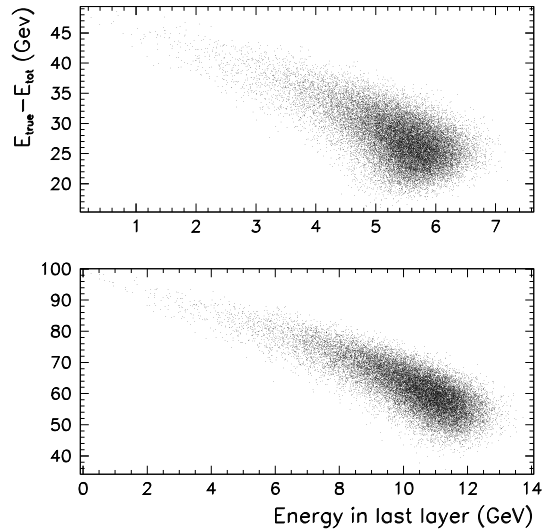


Figure 6.8. Total energy deposited in 8 layers by 50 GeV and 100 GeV electrons versus the energy deposited in last layer.

The corrected energy, E_{corr} plotted in figure 6.9 for 1 GeV, 5 GeV and 10 GeV electrons, and the corresponding total energy deposited in the calorimeter for comparison. The results from the last layer correction are summarised in table 6.3 and shows a significant improvement over using the only the total deposited energy. It also gives a better energy resolution than the shower profile fitting method.

6.1.3 Maximum likelihood method

The idea behind the maximum likelihood (ML) (e.g. [91]) method is to determine the parameter, in our case the true energy E_{true} , that maximises the likelihood function $L(x|E)$ of the sample data x . The distribution of the variable x for given E_{true} is obtained from many repeated experiments using Monte Carlo simulations. The likelihood function is the probability for fixed x seen as a function of the hypothesis E_{true} . This implies that in order to use the ML method, distributions have to be constructed for ideally all the hypothesis space, in our case all E_{true} . In a more realistic case the hypothesis would also include other parameters characterising each events energy deposit like, for example, the incidence angle θ . However, more than one parameter will increase the complexity of the method, and is not discussed further here.

An example of using the ML method for energy reconstruction in a segmented calorimeter having 8 layers is to use the layer energy distributions E_1, \dots, E_8 ob-

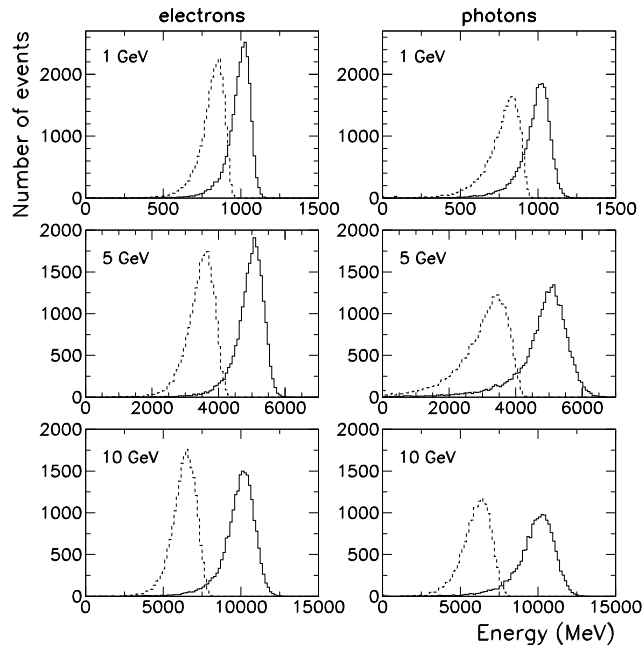


Figure 6.9. Reconstructed energy with the last layer method for 1 GeV, 5 GeV and 10 GeV electrons.

tained in chapter 5. If normalised, the energy fluctuations in the calorimeter layers generate the distributions that describe the probability of measuring a certain energy in a layer for a given initial energy. From simulations, the distributions of E_1, \dots, E_8 are obtained for a range of true energies and the likelihood $L(E_1, \dots, E_8 | E_{true})$ can be mapped. When reconstructing the energy, the most probable value of E_{true} is that maximising L for fixed E_1, \dots, E_8 . The ML method can also be used with the last layer correction variables, E_8 and E_{tot} , or the parameters a , b and E_0 obtained from longitudinal profile fitting. A ML method using the profile parameters can be found in [92].

The ML method is advantageous since no analytic expression is needed, and detector effects are included. The drawback is that it is a cumbersome method, since parameters must be calculated for a wide range of true energies and incident angles. It is also crucial that simulations are verified with experimental data.

Table 6.3. Results from the last layer method.

Particle type	Energy (GeV)	Last layer method		Total energy	
		E_{corr}	$\frac{\sigma_E}{E}$ (%)	E_{tot}	$\frac{\sigma_E}{E}$ (%)
e^-	1	1.0	5.1	8.3	6.7
γ	1	1.0	6.6	8.1	8.9
e^-	5	5.0	6.4	3.5	9.7
γ	5	5.0	9.3	3.3	14.5
e^-	10	10.1	7.6	6.4	10.8
γ	10	10.1	9.1	6.2	13.3

6.2 Summary

To conclude, the ML method can be used with the parameters of the different reconstruction methods. In our study the longitudinal profile fitting was found to be feasible for the true energies 1 GeV and 10 GeV, but not for 50 GeV due to non-contained shower maximum. In reality, material in front of the calorimeter and non-perpendicular incidence will push this limit. In GLAST, where the tracker adds an extra $1.3X_0$, the upper limit is approximately 100 GeV for perpendicular incidence. The low energy limit is due to poor statistics of the shower energy deposition, however no energies below 1 GeV were simulated. Due to non-negligible energy absorption in the tracker this lower limit is around 100 MeV in GLAST. Hence, below about 100 MeV, tracker parameters must be included in the likelihood functions. The energy leakage variables are useful roughly in the same energy range as the profile fitting method, since it also depends on whether the shower maximum is contained or not. The energy distributions in the layers are useful in the same energy range as discussed above.

Chapter 7

Conclusions and outlook

The choice of CsI(Tl) crystals is well suited for space missions calorimetry for several reasons; it allows the construction of a compact and segmented calorimeter, it has a high light yield which enables good energy resolution and it is a rugged and non-hygroscopic material. CsI(Tl) is also suitable for PIN diode readout. The modularity of the GLAST calorimeter makes it easy to integrate and test before launch, and less vulnerable to component failure during flight. It also provides information of the electromagnetic shower development radially and longitudinally. The flight crystals measure $32.60 \times 2.67 \times 1.99 \text{ cm}^3$, their size chosen as a compromise between channel readout noise and sufficient segmentation to resolve the shower. The segmentation also enables assistance in background rejection.

7.1 Radiation hardness tests

In orbit, GLAST will be exposed to radiation from cosmic-rays and the radiation belts surrounding Earth, and therefore it is necessary to test the radiation tolerance of the detector components. The flight crystals are cut from large CsI(Tl) boules, and in order to test the radiation hardness of the calorimeter crystals, samples from each boule have been irradiated with gamma-rays. In this way each CsI(Tl) boule was tested and approved before cutting the flight crystals. The boule samples are cylindrical, measuring 2.5 cm in diameter and 2.5 cm in height, and are read out with PIN diodes at one end. In total, 52 boule samples were irradiated with gamma-rays from a ^{60}Co source at a dose rate of 20 Gy/h. The relative decrease in light yield from each crystal was measured after 20, 50, 100 and 200 Gy accumulated dose, to be compared to the expected dose in orbit of 20 Gy over a 5 year mission. The requirement for the GLAST crystal performance is that the decrease in relative light yield should not be larger than 50% after having received a total dose of 100 Gy. A crystal log, having the same dimensions as a flight crystal, was also irradiated with gamma-rays in order to check the correspondence of radiation damage of the

samples with the crystal logs in the calorimeter. Since a large fraction of the radiation environment consists of protons, a crystal log was also irradiated with 180 MeV protons.

All boule samples were well within the limits of the required radiation hardness, showing an average decrease in light output of $(15.6 \pm 0.7)\%$ after 200 Gy. The largest decrease in light yield was $(27 \pm 0.7)\%$, and the variation between the boule samples was less than 20%. A similar result, $(24 \pm 4)\%$, was found in the radiation hardness test of the crystal log irradiated with 180 Gy at the same ^{60}Co facility and at the same dose rate. Light output was measured with PM tubes. Two different components of the radiation damage were found as a cause of the decrease in light output, namely decreased light production and increased self-absorption. Measurements of light yield were difficult to perform up to 48 hours after irradiation due to induced afterglow. The irradiation of a CsI(Tl) crystal log with 180 MeV protons showed a decrease in light output of $(21 \pm 7)\%$ after a dose of 175 Gy. The light output was measured with PIN diodes. There was induced activity due to the proton irradiation, and some of the isotopes could be identified. A large fraction of the induced activity had settled after a few weeks. Due to the low average dose rate in orbit, not much activity will be induced in the crystals. The half-life of the isotopes found are short with respect to the actual activation rate in orbit, and should not cause any significant noise in the detector. The GLAST CsI(Tl) crystals show radiation damages of similar magnitude for equivalent doses of ^{60}Co gamma-rays and 180 MeV protons.

The GLAST CsI(Tl) crystals show acceptable radiation tolerance, and no more radiation hardness tests are planned. The next important step in handling aging effects of the crystals, will be to map the calorimeter response to heavy ions in order to perform calibration in orbit

7.2 Simulations of energy fluctuations

The fluctuations in starting point and development of electromagnetic showers affect the estimation of the initial energy. This is especially problematic at high energies when large parts of the shower leaks from the calorimeter boundaries. It is therefore important to study the shower-to-shower fluctuations.

Detailed Geant4 simulation studies of electromagnetic shower fluctuations in a GLAST-like CsI calorimeter was performed in the energy range 1–100 GeV and at incident angles 0° , 30° and 60° . The showers were sampled in layers of 1.99 cm ($1.08X_0$) thickness, and the energy distributions in the layers were studied. The energy distributions are similar for incident electrons and photons and were found to change systematically along the shower, varying little with the initial energy. Three probability distributions were fitted to the data: negative binomial, log-normal and Gaussian distributions, none of which gives a good fit over the full shower length. The energy fluctuations generated from non-perpendicular incident were similar compared to those for perpendicular incidence. The total energy measured

in 8 layers ($8.6X_0$) for perpendicular incident shows distributions that become wider with increasing energy. Contaminations between showers of different energies are larger for photons than for electrons. About 30% of the 100 GeV electrons fall in the range for 50 GeV electrons, and for photons the corresponding contamination is about 55%.

The segmentation of the calorimeter enables several energy reconstruction algorithms to be employed, where information from the segments can be used to estimate the energy leakage out from the calorimeter boundaries and in cracks and gaps between calorimeter modules.

Two energy reconstruction methods were studied, shower profile fitting, and leakage correction. The aim was to compare the existing methods, and investigate whether the parametrisation of the layer fluctuations could assist in the reconstruction of the initial energy. Shower profile fitting gave an energy resolution of 10.7% (13.0%) and 12.1% (14.8%) for 1 GeV and 10 GeV electrons (photons) respectively. The method was found to overestimate the initial energy when the shower maximum was outside the detector. In a calorimeter having 8 layers (corresponding to $8.6X_0$), this occurred already at 10 GeV for electrons and photons with perpendicular incidence. Note that the GLAST calorimeter has additional material of about $1.3X_0$ in front of the calorimeter, and should therefore be able to use this method at higher energies. If only events having maximum within the first 7 layers are included, the overestimation of the energy is reduced. In order to even further reduce the energy resolution with this method, it is necessary to constrain the parameters of the longitudinal profile fit. The last layer correction method used the correlation between the energy deposited in the last layer and the leakage energy. It resulted in the best energy resolution, 5.1% (6.6%) and 7.6% (9.1%) for 1 GeV and 10 GeV electrons (photons), respectively.

A maximum likelihood method was discussed, and a more extensive study is needed to evaluate the possibility to further improve the energy reconstruction.

At the time of writing, a beam test is being prepared with 2 complete towers, which will enable the simulations to be compared with experimental data.

Acknowledgments

Everyone who has produced a doctoral thesis knows all about the mixed emotions one goes through, excitement, fear, angst, stress, exhaustion (in that order) much similar to the five Kübler-Ross stages of grief, except with a much happier ending. For me, there have been much hard work with late nights and early mornings, but I could not have finished the thesis without the help of some people I now would like to thank.

Foremost, I would like to thank my supervisor, professor Per Carlson, for your invaluable help and encouragement, and also for giving me the opportunity to work with such an exiting project. You have taught me that, to quote Göran Zachrisson, “Drivern är bara en av 14 klubbor i bagen. Den viktigaste klubban sitter mellan axlarna, huvudet”. I would also like to thank Jan Conrad for his short but intense help with energy reconstruction and profile (neurosis?) fitting. I am also most grateful to Tore Ersmark and his invaluable help with Geant4, and for reassuring me that in a perfect world everything works just fine and people are happy. Last, but not least, I would like to thank Dr Janina Östling, for her excellent guidance through the five stages, which I experienced at least twice.

I would like to thank everyone in the Particle- and Astroparticle group, these five years have really been interesting and happy thanks to the comfortable atmosphere. A big hug to all the students and former students in my room Jens, Silvio, Petter, Hank. And of course an equally big hug to all the other students and former students Pelle, Erik, Cecilia, Björn, Lisa, Karl-Johan, Leo, Ylva, Martin. I would also like to give a special thanks to Johan Lundqvist and Mark Pearce for encouraging me to join the fabulous group in the first place.

A big kiss to all my friends, if I could only remember what you look like.

To my family Bengt, Hannele and David who always makes me feel safe and loved. Kustaa Kusi Kallen ikkunan alle. To my husband Anders for your love and patience, I love you above all.

The author would like to thank the K A Wallenberg foundation and the Swedish Space Board for financial support. Computing resources made available by a grant from the Göran Gustafsson Foundation are also acknowledged.

List of Figures

1.1	Sensitivity of gamma-ray detectors	7
2.1	The LAT instrument	13
2.2	LAT tracker tower	14
2.3	The GLAST CsI(Tl) Calorimeter	15
2.4	ACD scintillator tile	16
2.5	GLAST GBM	18
3.1	Electron/positron energy loss in Pb	21
3.2	Cross section CsI	24
3.3	Simple electromagnetic shower model	26
3.4	Electromagnetic and hadronic shower	30
3.5	Dual PIN diode	34
4.1	Energy band model of inorganic crystals	39
4.2	Potential energy diagram of luminescence centre	42
4.3	Trapping centres in a crystal lattice	43
4.4	Energy band structure of the intrinsic and extrinsic crystal	45
4.5	Core-to-valence luminescence	46
4.6	Sketch of a PIN diode	51
4.7	Emission spectrum of CsI	52
4.8	Temperature dependence of inorganic scintillators	53
4.9	The Van Allen belts	55
4.10	The South Atlantic Anomaly	56
4.11	Boule cutting	60
4.12	Boule sample with PIN diode	62
4.13	Boule sample test set-up	63
4.14	Typical ^{22}Na spectra from boule sample	64
4.15	Crystal log test set-up	65
4.16	Afterglow of irradiated CsI log	66
4.17	Proton irradiation test set-up	67
4.18	Proton beam profile	67
4.19	Proton test set-up for measuring light output	68

4.20	Leakage current measurement of PIN diodes	69
4.21	Afterglow measurement	70
4.22	Degradation of light yield of irradiated boule sample	71
4.23	Degradation of light yield of boule samples after 100 Gy	72
4.24	Background noise	74
4.25	Muon spectrum measured with crystal log	75
4.26	Ge-spectrum from activated crystal	76
4.27	Total gamma intensity from crystal log	78
5.1	Examples of 10 GeV electron showers	80
5.2	Geant4 simulation calorimeter	81
5.3	Average shower profiles 1, 10 and 100 GeV	82
5.4	Individual longitudinal profiles for 25000 10 GeV electrons	84
5.5	Energy fluctuations in the calorimeter layers, 1 GeV	85
5.6	Energy fluctuations in the calorimeter layers, 10 GeV	86
5.7	Energy fluctuations in the calorimeter layers, 100 GeV	87
5.8	Fits of energy fluctuations, negative binomial, log-normal and Gaussian	88
5.9	The reduced χ^2 of the fits	89
5.10	The negative binomial parameters as a function of layer	90
5.11	The log-normal parameters as a function of layer	91
5.12	The Gaussian parameters as a function of layer	92
5.13	The total energy deposited in 8 layers	93
5.14	Average longitudinal energy profiles for 0° , 30° and 60°	94
5.15	Energy fluctuations in the calorimeter layers, 10 GeV, 30°	95
5.16	Energy fluctuations in the calorimeter layers, 10 GeV, 60°	96
6.1	Gamma parameters, 10 GeV photons and electrons, 20 layers	99
6.2	Gamma parameters, 10 GeV photons and electrons, 8 layers	100
6.3	Events with large values of a and b	101
6.4	Example of overestimated E_0	102
6.5	Gamma parameters, shower maximum within 7 first layers	103
6.6	Total energy versus energy in the last layer	105
6.7	Bi-dimensional Gaussian fit	106
6.8	Negative correlation of last layer and total energy	107
6.9	Reconstructed energy, last layer correction method	108

List of Tables

1.1	High-energy gamma-ray missions	6
2.1	EGRET and GLAST mission parameters	10
3.1	Properties of some absorber materials	28
3.2	Calorimeter requirements	32
4.1	Band gap width of common scintillators	41
4.2	Properties of inorganic scintillators	48
4.3	Light yield of gamma-irradiated crystal log	73
4.4	Measured background with Ge(Li) detector	73
4.5	Identified isotopes	77
5.1	Gamma fit parameters, average profiles	83
6.1	Gamma fit parameters	98
6.2	Shower profile fitting results	104
6.3	Results from last layer correction method	109

Bibliography

- [1] S.W. Digel, Proc. PHYSTAT2003 eConf **C030908** (2003) WEAT001.
- [2] A. Morselli, Surveys High Energ. Phys. **16** (2002) 255.
- [3] GLAST Facilities Science Team, *GLAST Science Requirements Document – Final*, July (1999)
- [4] G. Jungman, M. Kamionowski, K. Griest, Phys. Rep. **267** (1996) 195.
- [5] L. Bergström, J. Edsjö, P. Ullio, Phys. Rev. D **66** (2002) 123502.
- [6] P. Ullio, L. Bergström, J. Edsjö, C. Lacey, Phys. Rev. Lett. **87** (2001) 251301.
- [7] P.E. Michelson, Proc. SPIE Int. Soc. Opt. Eng. **2806** (1996) 31.
- [8] W.B. Atwood, Nucl. Instrum. Methods Phys. Res. A **342** (1994) 302.
- [9] R.P. Johnson, Proc. SPIE Int. Soc. Opt. Eng. **4784** (2003) 288.
- [10] W.N. Johnson, IEEE Nucl. Sci. Symp. **1** (1997) 27.
- [11] A.A. Moiseev et al., Proc. 26th Int. Cosmic Ray Conf, (1999) 160.
- [12] D.J. Thompson et al., Astrophys. Journal **86** (1993) 629.
- [13] A. von Kienlin et al., Proc SPIE Int. Soc. Opt. Eng. **5488** (2004) 763.
- [14] C. Leroy and P.G. Rancoita, *Principles of Radiation Interaction in Matter and Detection*, World Scientific Publishing Co. Pte. Ltd. (2000).
- [15] Particle Data Group, S. Eidelman et al., Phys. Lett. B **592** (2004) 1.
- [16] A. Borsellino, Phys. Rev. **89** (1953) 1023.
- [17] H. Olsen, Phys. Rev. **131** (1963) 406.
- [18] K. Kleinknecht, *Detectors for particle radiation*, 2nd ed., Cambridge University Press (1998).

- [19] H.J. Bhabha and W. Heitler, Proc. R. Soc. A **519** (1937) 432.
- [20] J.F. Carlson and J.R. Oppenheimer, Phys. Rev. **51** (1937) 220.
- [21] B. Rossi and K. Griesen, Rev. Mod. Phys. **13** (1941) 240.
- [22] J.C. Butcher and H. Messel, Nucl. Phys. **20** (1960) 15.
- [23] A.A. Varfolomeev and I.A. Svetlollobov, Soviet Physics JETP **36** (1959) 1263.
- [24] G. Bathow et al., Nucl. Phys. B **20** (1970) 592.
- [25] C.J. Crannell, Phys. Rev. **161** (1967) 310.
- [26] G. Grindhammer, M. Rudowicz and S. Peters, Nucl. Instrum. Methods Phys. Res. A **290** (1990) 469.
- [27] E. Longo and I. Sestili, Nucl. Instrum. Methods **128** (1975) 283.
- [28] C. Fabjan in T.I. Ferbel., *Experimental techniques in high energy physics*, Addison-Wesley Publishing Company, Inc. (1987) 257.
- [29] L. Landau and I. Pomeranchuk, Dokl. Akad. Nauk SSSR **92** (1953) 735.
- [30] A.B. Migdal, Phys. Rev. **103** (1956) 1811.
- [31] H.D. Hansen, Phys. Rev. D **69** (2004) 032001.
- [32] S. Klein, Rev. Mod. Phys. **71** (1999) 1501.
- [33] T. Yuda, Nucl. Instrum. Methods **73** (1969) 301.
- [34] U. Amaldi, Phys. Scr. **23** (1981) 409.
- [35] G. Grindhammer and S. Peters, Proc. Int. Conf. on Monte Carlo Simulation in High Energy and Nuclear Physics (1993) (e-Print Archive: hep-ex/0001020).
- [36] C.W. Fabjan and F. Gianotti, Rev. Mod. Phys. **75** (2003) 1243.
- [37] C. Grupen, *Particle detectors*, Cambridge University Press (1996).
- [38] F. Schmidt, *CORSIKA Shower Images*, University of Leeds, UK. Available online: <http://www.ast.leeds.ac.uk/~fs/showerimages.html>.
- [39] A. Abashian et al., Nucl. Instrum. Methods Phys. Res. A **479** (2002) 117.
- [40] Babar collaboration, *The First Year of the BABAR Experiment at PEP-II*, SLAC-PUB-8539.
- [41] G. Kanbach et al., Space Sci. Rev. **49** (1988) 69.
- [42] W.N. Johnson et al., IEEE Trans. Nucl. Sci. **48** (2001) 1182.

- [43] W.B. Atwood, Nucl. Instrum. Methods Phys. Res. A **446** (2000) 444.
- [44] D. Bédérède et al., Nucl. Instrum. Methods Phys. Res. A **518** (2004) 15.
- [45] P. Carlson et al., Nucl. Instrum. Methods Phys. Res. A **376** (1996) 271.
- [46] B. Lott et al., In press, Nucl. Instrum. Methods Phys. Res. A.
- [47] W. Crookes, Chemical News **87** (1903) 241.
- [48] H. Geiger and E. Marsden, Proc. R. Soc. **82** (1909) 495.
- [49] E. Rutherford, Philos. Mag. **21** (1911) 669.
- [50] J.B. Birks, *The Theory and Practice of Scintillation Counting*, Pergamon Press (1964).
- [51] G.F. Knoll, *Radiation Detection and Measurement*, 3rd ed., John Wiley & Sons Inc. (2000) 231.
- [52] P.A. Rodnyi, *Physical Processes in Inorganic Scintillators*, CRC Press LLC (1997).
- [53] M. Moszyński et al., IEEE Trans. Nucl. Sci. **44** (1997) 1052.
- [54] C.W.E. van Eijk, Nucl. Instrum. Methods Phys. Res. A **460** (2001) 1.
- [55] S. Kubota, S. Sakuragi, S. Hashimoto and J.Z. Ruan, Nucl. Instrum. Methods Phys. Res. A **268** (1988) 275.
- [56] Hamamatsu Catalog No. KOTH0002E05, *Si Photodiodes and Charge Sensitive Amplifiers for Scintillation Counting and High Energy Physics*, June 1997.
- [57] A.J. Tylka, IEEE Trans. Nucl. Sci. **44** (1997) 2150.
- [58] J. Alcaraz et al., Phys. Lett. B **472** (2000) 215.
- [59] J. Barwick et al., Astrophys. Journal **498** (1998) 779.
- [60] NASA proposal, *GLAST Flight Investigation*, 1999.
- [61] H.F.-W. Sadrozinski, Nucl. Instrum. Methods Phys. Res. A **476** (2002) 722.
- [62] http://heasarc.gsfc.nasa.gov/docs/rosat/gallery/misc_saad.html
- [63] M. Kobayashi and M. Ishii, Nucl. Instrum. Methods B **61** (1991) 491.
- [64] M. Ishii and M. Kobayashi, Prog. Cryst. Growth Charact. Mater. **23** (1991) 245.
- [65] C.L. Woody, J.A. Kierstead, P.W. Levy, S. Stoll, IEEE Trans. Nucl. Sci. **39** (1992) 524.

- [66] R.Y. Zhu, Nucl. Instrum. Methods Phys. Res. A **413** (1998) 297.
- [67] M.A.H. Chowdhury et al., Nucl. Instrum. Methods Phys. Res. A **432** (1999) 147.
- [68] B.G. Zaslavsky, J. Cryst. Growth **200** (1999) 476.
- [69] G. Johansson, PhD thesis, Kalmar University (to appear).
- [70] F.H. Attix, *Introduction to Radiological Physics and Radiation Dosimetry*, Wiley-Interscience Publication, John Wiley & Sons Inc., New York (1986).
- [71] J.H. Hubbell and S.M. Seltzer, *Tables of X-Ray Mass Attenuation Coefficients and Mass Energy-Absorption Coefficients*, NISTIR 5632. Available online: <http://physics.nist.gov/PhysRefData/XrayMassCoef/cover.html>.
- [72] C.M. Lederer and V.S. Shirley, *Table of Isotopes*, 7th ed., John Wiley & Sons Inc. (1978)
- [73] S. Agostinelli et al., Nucl. Instrum. Methods Phys. Res. A **506** (2003) 250.
- [74] H.J. Bhabha and W. Heitler, Proc. R. Soc. London A **159** (1937) 432.
- [75] W.H. Furry, Phys. Rev. **52** (1937) 569.
- [76] A.N. Mitra, Nucl. Phys. **3** (1957) 262.
- [77] N. Arley, *On the theory of stochastic processes and their application to the theory of cosmic radiation*, Thesis, The Institute of Theoretical Physics, Copenhagen University (1943).
- [78] J.R. Prescott, Nucl. Instrum. Methods **39** (1966) 173.
- [79] A. Giovannini et al., Nuovo Cimento Soc. Ital. Fis. A **24** (1974) 421.
- [80] G.J. Alner et al., Phys. Lett. B **160** (1985) 193.
- [81] A.T. Bharucha-Reid, *Elements of the Theory of Markov Processes and Their Applications*, McGraw-Hill, New York (1960).
- [82] H. Messel and R.B. Potts, Phys. Rev. **87** (1952) 759.
- [83] T. Gaisser, *Cosmic Rays and Particle Physics*, Cambridge univ. press (1990).
- [84] V. de Souza, G. Medina-Tanco, J. A. Ortiz, astro-ph/0511677 (2005).
- [85] S. Ajimura et al., Nucl. Instrum. Methods Phys. Res. A **552** (2005) 263.
- [86] K. Amako et al., Nucl. Sci., IEEE Trans. Nucl. Sci. **52** (2005) 910.
- [87] R. Wigmans and M.T. Zeyrek, Nucl. Instrum. Methods Phys. Res. A **485** (2002) 385.

- [88] C. Walck, *Hand-book on Statistical Distributions for Experimentalists*, Internal report SUF-PFY/96-01, Stockholm University (1996).
- [89] E. do Couto e Silva et al., Nucl. Instrum. Methods in Phys. Res. **A474** (2001) 19
- [90] Bruel, *Energy reconstruction at high energy with the LAT*, Internal Report (2005). Available online: <http://polywww.in2p3.fr/~bruel/CalFullProfile.pdf>
- [91] G. Cowan, *Statistical Data Analysis*, Oxford University Press Inc., New York (1998)
- [92] P. d'Avezac, *A Maximum-Likelihood Energy Reconstruction Method*, Internal Report (2006). Available online: <http://polywww.in2p3.fr/glast/CalLikelihood.pdf>